Geochemistry of fluid-rock processes

Hector M. Lamadrid

Dissertation submitted to the faculty of the Virginia Polytechnic Institute and State University in partial fulfillment of the requirements for the degree of

Doctor of Philosophy
In
Geosciences

Robert J. Bodnar
James Beard
Mark Caddick
Frieder Klein
Robert Lowell
Robert Tracy

April 29, 2016
Blacksburg, VA

Keywords: Fluid inclusions, Raman spectroscopy, granulite rock metamorphism, serpentinization, synthetic fluid inclusions, rates of reaction.

Geochemistry of fluid-rock processes

Hector M. Lamadrid

ABSTRACT

When these fluids interact with the surrounding rocks, small aliquots of these fluids are trapped as imperfections in the crystal lattice and fractures of minerals. These microscopic features are called fluid and melt inclusions, and are one of the best tools available to probe, measure and determine the chemical and physical properties of crustal fluids. In the present study we examine new developments into our understanding of fluid-rock interactions using fluid and melt inclusion as tools to provide insights into the evolution of the Earth's crust from the deep continental crust to the surface. Chapter II "Raman spectroscopic characterization of H_2O in CO_2-rich fluid inclusions in granulite facies metamorphic rocks", is a brief review of the current understanding of granulite rocks and their formation, and a new development into our ability to characterize the composition of the fluids trapped as fluid inclusions in minerals in granulite facies rocks. Chapter III "Reassessment of the Raman CO_2 densimeter" details new developments in the use of the Raman spectroscopy to characterize the density of CO_2. In this chapter we describe briefly the Raman effect of CO_2 and the density dependence of the Fermi diad using different Raman instruments, laser sources and gratings to understand the differences in the published data. Chapter IV "Serpentinization reaction rates measured in olivine micro-batch reactors" describes new insights into the serpentinization process by using olivine micro-reactors. The micro-reactor technique is a new experimental

development that allows researchers to monitor the fluid chemistry as well as the mineral composition changes inside the synthetic fluid inclusions.

Table of contents

List of Tables

Chapter 3. Reassessment Of The Raman CO_2 Densimeter

Chapter 4. Serpentinization reaction rates measured in olivine micro-batch reactors

List of Figures

Chapter 2. Raman spectroscopic characterization of H2O in CO2-rich fluid inclusions in granulite facies metamorphic rocks

Chapter 3. Reassessment Of The Raman CO_2 Densimeter

Chapter 4. Serpentinization reaction rates measured in olivine micro-batch reactors

Attributions

The following chapters include collaborations with researchers, professors and students inside and outside of the Department of Geoscience of Virginia Tech.

In Chapter II called "Raman spectroscopic characterization of H_2O in CO_2-rich fluid inclusions in granulite facies metamorphic rocks", I collaborated with William Lamb from the Department of Geology and Geophysics from Texas A&M University, M. Santosh from the School of Earth Sciences and Resources of the China University of Geosciences and the Faculty of Science in Kochi University Japan, and my advisor Robert J. Bodnar from the Department of Geosciences at Virginia Tech.

In Chapter III "Reassessment of the Raman CO_2 densimeter", I collaborated with Daniel Moncada from the Departamento de Geologia of the Universidad de Chile, Robert C. Burruss from the U.S. Geological Survey National Center in Reston Virginia and with Lowell Moore, Donald Rimstidt and my advisor Robert J. Bodnar from the Department of Geosciences at Virginia Tech.

Chapter IV "Serpentinization reaction rates measured in olivine micro-batch reactors" is an ongoing collaboration with Esther Schwarzenbach from the Institute of Geological Sciences, Freie Universität Berlin, Frieder Klein from the Woods Hole Oceanographic Institute, Andrei Dolocan from the Texas Materials Institute, University of Texas at Austin, Donald Rimstidt and Robert J. Bodnar from the Geoscience Department at Virginia Tech.

Chapter I

Introduction

Water (H_2O) and other volatiles like CO_2, CH_4, N_2, NH_4, SO_2, H_2S etc., are the major components of fluids on Earth's crust and in the upper mantle and they play an important role in the biological, geochemical, and physical evolution of the Earth and other bodies in the solar system. Fluids are essential in the formation of hydrothermal mineral deposits, they affect the dynamics and explosivity of volcanic systems, and significantly affect the way in which rocks deform and fracture. Furthermore, these volatiles species among other dissolved elements in a fluid phase (including melts) are responsible for the formation of the hydrothermal and magmatic systems that enable mass transfer between the mantle and the crust. When these fluids interact with the surrounding rocks, small aliquots of these fluids are trapped as imperfections in the crystal lattice and fractures of minerals. These microscopic features are called fluid and melt inclusions, and are one of the best tools available to probe, measure and determine the chemical and physical properties of crustal fluids.

For several decades the Virginia Tech Fluids Research group have focused in studying the physical and chemical properties of fluids, and the fundaments of fluid-rock interactions and their implications into the evolution of the Earth and other planetary bodies. One of developing experimental, analytical and modeling techniques to study fluid and melt inclusions, have provided the theoretical and empirical framework necessary for the interpretation and characterization of fluid and melt inclusions.

In the following chapters of this dissertation the reader will be presented with some recent advances in the understanding of fluid-rock interactions in different geological environments.

Chapter II "Raman spectroscopic characterization of H_2O in CO_2-rich fluid inclusions in granulite facies metamorphic rocks", is a brief review of the current understanding of granulite rocks and their formation, and a new development into our ability to characterize the composition of the fluids trapped as fluid inclusions in minerals in granulite facies rocks.

Chapter III "Reassessment of the Raman CO_2 densimeter" details new developments in the use of the Raman spectroscopy to characterize the density of CO_2. In this chapter it is described briefly the Raman effect of CO_2 and the density dependence of the Fermi diad using different Raman instruments, laser sources and gratings to understand the differences in the published data.

Chapter IV "Serpentinization reaction rates measured in olivine micro-batch reactors" describes new insights into the serpentinization process by using olivine micro-reactors. The micro-reactor technique is a new experimental development that allows researchers to monitor the fluid chemistry as well as the mineral composition changes inside synthetic fluid inclusion.

Chapter II

Raman spectroscopic characterization of H_2O in CO_2-rich fluid inclusions in granulite facies metamorphic rocks

H. M. Lamadrid, W. Lamb, M. Santosh and R. J. Bodnar

Abstract

Water (H_2O) has been identified during Raman analyses at ~150-200°C of fluid inclusions from granulites that were previously thought to contain pure CO_2. At room temperature, H_2O in a CO_2- rich fluid inclusion forms an optically unresolvable liquid wetting the inclusion walls. During heating the H_2O phase evaporates into the CO_2 phase to produce a homogeneous H_2O-CO_2 fluid throughout the inclusion volume, and the H_2O Raman peak at ~3661 cm^{-1} is clearly resolvable at elevated temperatures. To test and confirm the method, synthetic H_2O-CO_2 FI of known composition (87.5 mol% and 95 mol% CO_2) were also analyzed.

Previously studied natural samples of granulites from the Adirondack Mountains, USA, and from the Kerala Kondalite Belt, Sittampundi Complex and Sevitturangampatti, India were tested for the presence of H_2O in CO_2-rich fluid inclusions. Traces of H_2O were found in CO_2-rich fluid inclusions in quartz crystals from the Adirondacks and from the Kerala Kondalite Belt. H_2O was not detected in CO_2-rich secondary fluid inclusions in garnet from the Sittampundi Complex and from Sevitturangampatti. Rather, hydrogarnet was detected along the walls of inclusions in garnet, as evidenced by a peak

at ~3661 cm^{-1}. The hydrogarnet is interpreted to be a "step-daughter" phase that formed by reaction of the H_2O in the fluid inclusion with the garnet host during retrogression. These observations confirm the presence of an H_2O-bearing fluid at some time during granulite petrogenesis.

1. Introduction to granulite petrogenesis

Granulite facies metamorphism occurs at high temperatures and high pressures, with the boundary between the amphibolite and granulite facies defined by the first appearance of metamorphic orthopyroxene in mafic rocks (Spear, 1993). Granulites form large domains in the cores of Precambrian shields as well as in more recent mobile belts, and also are commonly found as xenoliths in recent volcanic products (Kelsey, 2008). Granulites represent a major component of the lower crust and are thus thought to be critical for understanding the evolution of the continents (Newton, 1986).

Mineral equilibria indicate equilibration temperatures and pressures ranging from 650 to 1200˚C and from 5 to >30 kbar for the peak of granulite facies metamorphism (Harley, 1989; Bohlen, 1991; Brown, 2007; Kelsey, 2008) (Fig. 1). Pyroxenes represent a major phase in granulites, whereas the hydrous minerals mica, amphibole and epidote are more typical of amphibolite and other lower grade metamorphic rocks (Touret, 1985). Granulite facies metamorphism is thus characterized by the presence of relatively anhydrous mineral assemblages, including pyroxene-rich mafic rocks, sillimanite-K-feldspar assemblages in metapelitic rocks, and metamorphic orthopyroxene in quartzofeldspathic rocks. These anhydrous phases often co-exist with hydrous phases, such as amphibole and biotite, over a range of temperatures. However, the ratio of

anhydrous to hydrous phases changes with increasing temperature, and at the highest grades, hydrous phases may be totally absent.

The genesis of granulite facies metamorphic rocks and the role of fluids in granulite formation have been of special interest and have fueled an ongoing debate within the scientific community (Clemens, 1992, 1993, 1995; Clemens et al., 1997; Clemens and Droop, 1998; Clemens and Watkins, 2001; Fyfe, 1973; Lamb and Valley, 1988; Newton et al., 1980; Newton, 1986; Newton et al., 1998; Newton and Manning, 2002, 2010; Santosh et al., 1993; Stevens and Clemens, 1993; Stevens et al., 1997; Touret, 1985, 2009; Huizenga and Touret, 2012; Touret and Huizenga, 2012a; Valley, 1985; Valley et al., 1990). Because granulite facies metamorphism typically occurs at temperatures higher than the H_2O-saturated melting curve for intermediate composition rocks, it has generally been assumed that any fluids involved in granulite formation must have low H_2O concentrations (or activities) to prevent large-scale melting (Fig. 2). One observation that is commonly offered as evidence for H_2O-poor fluids associated with granulite facies metamorphism is the ubiquitous occurrence of presumably pure CO_2 fluid inclusions in granulites. Here, we describe analyses of presumably pure CO_2 fluid inclusions from granulites, using a methodology described by Dubessy et al. (1992) which has recently been modified and applied to identify small amounts of H_2O in gas-rich inclusions in mantle xenoliths (Berkesi et al., 2009). The analyses confirm the ubiquitous occurrence of small amounts of H_2O in CO_2-rich inclusions from granulite facies rocks. While there is debate as to whether these inclusions represent the peak metamorphic fluid or if they represent inclusions that were trapped or which reequilibrated during retrogression,

results presented here are relevant to future studies related to the petrogenesis and evolution of granulite facies rocks.

The ongoing debate concerning the formation of granulites is centered around two main issues, (1) whether or not large amounts of externally buffered, chemically active fluids infiltrated during the peak of metamorphism (Newton et al., 1980; Valley and Essene, 1980; Valley and O'Neil, 1984; Lamb and Valley, 1985; Valley, 1985; Vry et al., 1988; Moecher and Essene, 1990, 1991; Cartwright and Valley, 1991; Santosh, 1992; Clemens, 1993; Santosh and Omori, 2008) and, (2) the composition of any fluids that might have been present (Newton et al., 1998; Newton and Manning, 2010; Touret and Huizenga, 2012a). Granulite facies mineral assemblages typically record H_2O activities that are less than ~0.5 and often in the range 0.1 to 0.4 (Philips, 1980; Valley et al, 1984; Powers and Bohlen, 1985; Bhattacharya and Sen, 1986; Lamb and Valley, 1988; Valley et al., 1990; Ouzegane et al., 2001; Bendaoud et al., 2004). These a_{H_2O} values are, in general, low relative to those estimated for lower grade (e.g., amphibolite facies) rocks, and various processes have been proposed to generate the low a_{H_2O} fluids required for granulites facies metamorphism.

One possible mechanism to generate a low a_{H_2O} fluid environment is partial melting in the deep crust (anatexis) (Thompson, 1983; Clemens and Vielzeuf, 1987; Clemens, 1990; Patiño-Douce and Johnston, 1991; Skjerlie et al., 1993), followed by extraction of a melt phase that migrates to shallower depths in the crust (Fyfe, 1973). Any H_2O present would be partitioned preferentially into the melt, and the refractory residuum would crystallize anhydrous mineral phases that are typical of granulite facies rocks. This mechanism is supported by experiments in which partial melting is achieved in normal upper crustal

lithologies by the progressive break down of hydrous minerals to generate water that lowers the melting point of the rock to produce a granitic melt (Clemens and Vielzeuf, 1987; Clemens, 1990; Patiño Douce and Johnston, 1991; Skjerlie et al., 1993). According to this model, the lower crust is depleted in H_2O and other incompatible elements, such as U, Th and Rb, that would be partitioned into the melt phase along with H_2O, leaving behind a refractory residuum that is largely anhydrous (Thompson, 1983).

Some authors invoke field evidence, including the occurrence of orthopyroxene in migmatites from granulite terranes, to preclude the partial melting mechanism described above (Percival, 1991; Newton et al., 1998; Harlov et al., 2006; Rajesh et al., 2013). These workers argue that the dehydration melting process should be reversed upon freezing of the melts higher in the system. H_2O that is exsolved from the melt should rehydrate the rocks to produce biotite from orthopyroxene, unless the a_{H_2O} of the fluid exsolved from the melt remains low (Percival, 1991) or if the melt does not become saturated in H_2O. However, others have argued that orthopyroxenes might have been armored by quartz, feldspar or hornblende as the activity of H_2O increased during cooling and crystallization, thus preventing alteration of the orthopyroxene, or that H_2O released during crystallization migrated along discrete channels and did not infiltrate the bulk rock (Waters, 1988). It should also be noted that some workers have suggested that melting in the mid- to lower-crust may occur under fluid-absent conditions (Stevens and Clemens, 1993), such that the melt contains an insufficient amount of H_2O to become saturated during crystallization.

A second mechanism that has been proposed to stabilize granulite facies mineral assemblages is the infiltration of low a_{H_2O} fluids. This process is referred to in the

literature as a "fluid assisted" process (Touret, 2009), "fluid-induced" process, or simply metasomatism (Newton et al., 1998; Harlov et al., 2006; Safonov et al., 2012; Rajesh and Santosh, 2012, Rajesh et al., 2013). Accordingly, it has been suggested that influx of large amounts of CO_2 (referred to as CO_2-flushing, CO_2-streaming, or CO_2-infiltration in the literature) or other low a_{H_2O} fluid (such as high salinity brines) into the mid- to lower-crust is responsible for driving reactions (metasomatism) that produce granulite facies minerals (Touret, 1971; Newton et al., 1980, Santosh et al., 1993; Harlov et al., 2006; Santosh and Omori, 2008; Safonov et al., 2012; Rajesh and Santosh, 2012, Rajesh et al., 2013). Studies of granulite facies rocks from Halmstad, SW Sweden (Harlov et al., 2006) and the Limpopo Complex, South Africa (Rajesh et al., 2013) report textural and fluid inclusion evidence of low a_{H_2O} saline fluids (CO_2-H_2O-K, NaCl fluid) that exsolved from a cooling leucosome, driving dehydration reactions at granulite facies conditions. Experimental studies based on lithologies in the Limpopo Complex (Safonov et al., 2012) suggest that textural relations observed could have been triggered by the interaction of H_2O-CO_2-salt fluids with the Sand River gneiss.

A third mechanism that has been proposed to explain the absence of fluids (H_2O) associated with granulite petrogenesis is metamorphism of already "dry" metamorphic or igneous rocks. For example, if an orthopyroxene-bearing igneous rock were metamorphosed under granulite facies P-T conditions, the effects of metamorphism might obliterate any igneous textures, yet the orthopyroxene-bearing mineral assemblage, stable at low a_{H_2O}, could persist throughout the metamorphic event (Lamb and Valley, 1988; Valley et al., 1990). In this case the low a_{H_2O} was inherited from its protolith (Lamb and Valley, 1988).

The ubiquitous occurrence of fluid inclusions in granulites from different locations, ages and tectonic settings has been offered as evidence to challenge the model of an anhydrous lower crust generated by "fluid-absent" processes (Touret, 1971). Most of the fluid inclusions in granulites contain mainly CO_2, with variable densities that occasionally coincide with the peak of metamorphism (Ohyama et al., 2008; Santosh et al., 2010) or are consistent with post-metamorphic entrapment and/or reequilibration during retrogression (Lamb et al., 1987; Morrison and Valley, 1988, Ohyama et al., 2008). Tsunogae et al. (2008) report that CO_2 is the dominant species at peak metamorphic conditions in UHT granulites from southern India, based on Raman analysis of fluid inclusions. However, other minor species such as N_2 (5.0 mol%), H_2O (0.5 mol%) and CH_4 (0.47 mol%) were trapped in fluid inclusions during retrogression. Although less common, highly saline aqueous inclusions (brines) are reported, and the composition and density of these inclusions in some cases approaches that of molten salt (Touret, 2009). These inclusions are not entirely unlike the carbonate-salt melt "fluid inclusions" that have recently been reported in diamonds (Izraeli et al., 2001; Klein-BenDavid et al., 2007).

CO_2-rich fluids in granulites can be explained either by CO_2-infiltration (Newton et al., 1980), or by removal of water and other components from an original H_2O-CO_2±"salt" fluid. Thus, the H_2O component of an H_2O-CO_2 fluid would partition into a silicate melt, leaving behind a CO_2-rich fluid (Clemens, 1992, 1993, 1995; Stevens and Clemens, 1993; Clemens et al., 1997; Stevens et al., 1997; Clemens and Droop, 1998; Clemens and Watkins, 2001). Two of the mechanisms that have been proposed to stabilize granulite facies mineral assemblages are consistent with the presence of a CO_2-

rich peak metamorphic fluid. However, the low solubility of most ionic species and silicate minerals in a CO_2-rich fluid have been cited as evidence that CO_2 alone cannot be responsible for some features observed in granulite facies metamorphism, including alkali-exchanged feldspars (Na^+ with K^+) in charnockites, garnet corrosion textures, synmetamorphic quartz veins, the apparent mobility of Ca, Fe, Mg, and REE, and depletion of Rb and Th (Newton et al., 1998). Moreover, the relatively low fO_2 predicted from mineral equilibria in some granulite terranes is inconsistent with the presence of CO_2-rich fluids (Lamb and Valley, 1984; Lamb and Valley, 1985). Furthermore, thermodynamic calculations indicate that some granulites were not metamorphosed in the presence of a C-O-H fluid and suggest that a free fluid phase was not present during the peak of granulite facies metamorphism (Lamb and Valley, 1984; Lamb and Valley, 1985). Thus, while some workers emphasize the role of CO_2 to explain the occurrence of low a_{H_2O} fluids in granulite petrogenesis (Santosh and Omori, 2008), other workers have suggested that high-salinity H_2O-bearing fluids represent the low a_{H_2O} fluid that drives granulite facies metamorphism (Crawford and Hollister 1986; Smit and Van Reenen, 1997; Newton et al., 1998; Van den Berg and Huizenga, 2001; Yardley and Graham, 2002; Harlov et al., 2006; Touret, 2009; Newton and Manning, 2010; Touret and Huizenga, 2011, 2012a; Safonov et al., 2012; Rajesh et al., 2013) .

It should be emphasized here that much uncertainty exists concerning the timing of formation of fluid inclusions in granulite facies rocks relative to peak metamorphic conditions (c.f., Lamb et al., 1987, 1991; Lamb, 1990). Even if the fluid inclusions were trapped at peak metamorphic conditions, there is considerable evidence to suggest that the inclusions would likely re-equilibrate during retrogression, and could lose any H_2O in

the original fluid (Sterner and Bodnar, 1989; Hollister, 1990; Bakker and Jansen, 1991, 1994; Hall and Sterner, 1993; Barker, 1995; Vityk et al., 2000). Thus, interpretations of the fluid regime associated with peak metamorphic conditions in granulite facies rocks based on fluid inclusion data must consider the possibility that the fluids do not represent peak fluids, either because the inclusions were trapped at post-peak conditions and/or they have re-equilibrated following entrapment. However, granulite xenoliths sometimes show fluid inclusion textures and compositions similar to those found in granulites collected from surface outcrops. And, as it is generally assumed that fluid inclusions in xenoliths have experienced little or no re-equilibration during their rapid transport from the deep crust to the surface (Szabo and Bodnar, 1998), one might interpret the similarities between fluid inclusions in granulite xenoliths and those in granulites that have experienced slower metamorphic uplift and cooling to indicate that retrogression has not affected the composition of the fluid inclusions (Selverstone, 1982; Wass and Hollis, 1983; Ertan and Leeman, 1999, Sachs and Hansteen, 2000).

As noted above, petrographic, microthermometric and Raman analyses of fluid inclusions in granulites at ambient conditions have identified CO_2 as the dominant fluid species (Touret, 1985; Lamb, 1990; Tsunogae et al., 2008). Fluid inclusions in many granulite samples show small depression of the melting temperature at the CO_2 triple point (-56.6˚C) indicating that other species (e.g., N_2, H_2S, or CH_4) are present at low concentrations (e.g., the triple point of CO_2 is initially lowered by about 1°C by addition of 5 mol% of CH_4) (Newton, 1986; Hall and Bodnar, 1990). H_2O has a negligible effect on the melting temperature of CO_2, and, therefore, some H_2O may be present in CO_2-rich fluid inclusions from granulite facies rocks and it would not be detected during

microthermometry. It is important to note that even low concentrations of H_2O can result in fluids in which the a_{H2O} is relatively high, owing to the positive deviation from ideal mixing exhibited by the system H_2O-CO_2 at P-T conditions appropriate for granulite formation (Fig. 3).

At room temperature and pressures up to a few hundred bars, CO_2 and H_2O are largely immiscible, and any fluid inclusion that originally trapped an H_2O-CO_2 fluid at peak granulite facies conditions would contain two phases at room temperature – one that is nearly pure CO_2 and the other nearly pure H_2O. Owing to the different wetting behaviors of CO_2 and H_2O (Beere, 1975; Watson and Brenan, 1987), the liquid H_2O phase would occur as a thin film on the walls of the fluid inclusion. As a result, an inclusion could contain a significant amount of H_2O that would not be detectable during petrography, microthermometry and/or conventional Raman spot analysis at ambient temperature. For example, if a 10 μm diameter spherical fluid inclusion contains 90 mol% CO_2 with a density of 0.7 g/cm^3, and 10 mol% H_2O with a density of 1 g/cm^3, the H_2O phase will occur as a 0.05 μm (50 nanometer) film on the inclusion walls (Fig. 4). Thus, a significant amount of H_2O could be present in a fluid inclusion and yet it would be impossible to resolve optically, or by microthermometry, or Raman spot analysis. In this study, we have re-visited several well-characterized granulite environments, applying a recently described analytical technique that has been used successfully to identify H_2O in CO_2-rich inclusions in mantle xenoliths (Berkesi et al., 2009; see also Dubessy et al., 1992), to test for the presence of H_2O in the fluid inclusions.

2. Methods

The method used in this study is similar to that described by Dubessy et al. (1992) and further refined by Berkesi et al. (2009), and involves conducting Raman analyses at temperatures of ≈150-200°C. During heating, an optically unresolvable liquid H_2O phase occurring as a thin film on the inclusion walls (Fig. 4) will dissolve (evaporate) into the CO_2 liquid phase to produce a one-phase, homogeneous CO_2 liquid-rich fluid phase. In this case, the H_2O component will be uniformly distributed throughout the inclusion volume, and thus the precise location of the laser spot during analysis is not critical (as long as it is within the inclusion). This technique allows workers to recognize small amounts of H_2O that might otherwise be missed if the fluid inclusions are analyzed at room temperature.

Synthetic CO_2-rich, H_2O-CO_2 fluid inclusions of known composition, containing 87.5 mol% and 95 mol% CO_2, were used to test and confirm the method for analyzing CO_2-rich fluid inclusions containing small but known amounts of H_2O (Sterner and Bodnar, 1984; Sterner and Bodnar, 1991). During normal petrographic examination at room temperature, a distinct liquid H_2O phase could be recognized in about 1/3 to 1/2 of the larger (>10-15 μm) tubular or more irregularly-shaped synthetic fluid inclusions containing 87.5 mol% CO_2 (Fig. 5A). No evidence of a separate H_2O phase was observed in any fluid inclusions less than about 5 μm for this composition. In the 95 mol% CO_2 sample, a distinct liquid H_2O phase was never recognized during normal petrography (Fig. 5B). This suggests that a separate H_2O phase can be resolved optically in natural fluid inclusions that contain more than about 5-10 mol% H_2O and which are larger than about 10-15 μm. A separate H_2O liquid phase is less likely to be recognized in fluid inclusions containing <5 mol% H_2O, regardless of the inclusion size or shape.

All of the natural fluid inclusions analyzed in this study had been previously studied to estimate fluid compositions and P-T conditions of granulite facies metamorphism and retrogression (Lamb et al., 1987; Santosh et al., 1993, Santosh and Tsunogae, 2003; Ohyama et al., 2008; Santosh et al., 2010). In most cases, the same polished plates and fluid inclusions examined in these earlier studies were analyzed here. The analyses focused on CO_2-rich inclusions that contain no visible H_2O phase when examined petrographically at room temperature. After the inclusions were located, all inclusions were first analyzed by Raman spectroscopy at room temperature. The thickness of the fluid inclusion wafers (thick sections) used in this study is between 100 to 200 μm.

Raman analyses were performed using a JY Horiba LabRam HR (800 mm) spectrometer, with 600 grooves/mm gratings. The slit width was set to 150 μm, and the confocal aperture at 400 μm. Excitation was provided by a 514.53 nm (green) Laser Physics 100S-514 Ar^+ laser. The laser output was 50 mW at the source and <10 mW at the sample. The detector was an electronically cooled open electrode CCD.

The collection time varied according to the optical characteristics of the samples and fluid inclusions sizes. Most synthetic and natural fluid inclusions were analyzed with a 40x objective (N.A. = 0.55) with cover-glass correction to improve signal to noise (Adar et al., 2004). Data were collected over the spectral range 500 to 4000 cm^{-1} using 3 accumulations of 60 seconds. This range includes the Fermi diad for CO_2 at 1285 cm^{-1} and 1388 cm^{-1}, as well as the broad H_2O band that extends from about 3100 to 3700 cm^{-1}. For some smaller inclusions, an 80X objective was used. For each inclusion, the Fermi diad for carbon dioxide was collected by focusing the laser spot into the central part of the fluid inclusions to confirm the presence of CO_2. Then, several additional analyses

were conducted at ambient conditions, focusing the laser spot at various locations around the edges and in the middle of each inclusion, with the spectrometer positioned to monitor the broad H_2O band. It should be noted that only inclusions that did not show an optically resolvable H_2O phase at room temperature were selected for analysis.

After all inclusions were analyzed at room temperature, the fluid inclusions were heated to 150ºC and analyzed again. A Linkam THSG 600 heating/cooling stage was used to heat the samples and to maintain the fluid inclusions at constant temperature during Raman analysis. It is important to note that, in order to use the higher power (80x) objective to analyze some of the inclusions, the cover plate for the Linkam stage had to be removed. This results in a larger than normal thermal gradient within the sample chamber, and the exact temperature at the sample is estimated to be ~150 ±10ºC. This uncertainty in temperature is not considered to be significant, because the primary objective was to analyze the inclusions at a temperature sufficiently high such that some or all of the liquid H_2O film present on the inclusion walls at room temperature would evaporate into the CO_2-rich phase. The temperature of 150ºC for the Raman analyses was selected after monitoring the intensity of the H_2O peak in the synthetic fluid inclusions during heating from room temperature in 25ºC increments. The analyses revealed that the H_2O peak was clearly observable at 150°C, and this temperature was low enough to prevent decrepitation of the high density CO_2-rich fluid inclusions. The position of each measured Raman line and the peak areas were determined after baseline correction using Gaussian/Lorentzian peak fitting following the procedure outlined by Fall et al. (2011).

3. Results

3.1 Synthetic Fluid Inclusions

The compositions of the synthetic fluid inclusions used in this study were selected to be representative of the low H_2O concentrations expected in granulite facies metamorphism. The fluid inclusions analyzed ranged from about 5 to 20 μm. Fluid inclusions in the 87.5 mol% CO_2 sample tend to be larger, more equant (rounded) and more abundant, and some had a recognizable H_2O phase at room temperature (Fig. 6). Inclusions in the 95 mol% CO_2 sample are less abundant and more irregularly shaped (Fig. 5B) because the fractures in the host mineral (quartz) do not heal as quickly or completely at low H_2O concentrations as they do for more H_2O-rich compositions.

H_2O was detected during Raman spot analyses of some of the larger and more elongated 87.5 mol% CO_2 fluid inclusions at room temperature (Fig. 6). Raman mapping of a small (~5 μm) equant fluid inclusions containing 87.5 mol% CO_2 and with no visible H_2O revealed a thin film of H_2O wetting the walls (Fig. 4). The results confirmed that H_2O is indeed present, but the thin film of H_2O is typically not detected during Raman spot analysis at room temperature. H_2O was not detected in any of the 95 mol% CO_2 fluid inclusions at room temperature. After heating, all inclusions in both samples showed a weak H_2O peak at ~3640 cm^{-1} (Fig. 6).

3.2 Natural Inclusions

3.2.1 Adirondack Mountains, USA

Samples TP-5, LB-1, N-5, and IN-10 from the Adirondack metamorphic complex were previously studied by Lamb et al. (1987). These samples are magnetite and ilmenite-bearing Proterozoic granulites with quartz, K-feldspar, plagioclase, orthopyroxene, and minor garnet and biotite. In all samples, the fluid inclusions analyzed were CO_2-rich and hosted in quartz. Microthermometric measurements conducted by Lamb et al. (1987) found variable homogenization temperatures. Fluid inclusions in sample N-5 homogenize between 0º and 30ºC, while those in TP-5 homogenize between -10º and 20ºC. Fluid inclusions in LB-1 show a much smaller temperature range from -20 to -10ºC. Fluid inclusions in sample IN-10 show a wide range of homogenization temperatures, from -20º to +30ºC. The densities of the fluid inclusions estimated from homogenization temperatures range from ~0.5 to 1.14 g/cm^3.

In this study we analyzed CO_2-rich fluid inclusions in quartz from samples N-5, TP-5, LB-1 and IN-10 of Lamb et al. (1987). Raman spectroscopic spot analysis of the inclusions at room temperature failed to identify H_2O (Fig. 7A). However, when the same fluid inclusions were heated to 150°C a small H_2O peak at ~3640 cm^{-1} was present in all fluid inclusions (Fig. 7B), confirming the presence of small (but unknown) amounts of H_2O in the fluid inclusions.

Lamb et al. (1987) noted that mineral equilibria constrain the fugacity of CO_2 (quartz-calcite-wollastonite), or the oxygen fugacity (hercynite- or magnetite + ilmenite-bearing rocks), which can be used to place limits on the maximum amount of CO_2 in the peak metamorphic fluid. These results indicate that for 13 of 21 samples they studied (including sample LB-1) peak metamorphic mineral equilibria require low activity of CO_2 such that, if a fluid phase were present during the peak of metamorphism, it could

not be CO_2-rich. Thus, these workers interpreted the CO_2-rich fluid inclusions in these samples to reflect post peak metamorphic conditions.

3.2.2 Kerala Kondalite Belt, India

Sample NLK1/2, from Kerala, South India, was first described by Santosh et al. (1993). The sample is a late Neoproterozoic-Cambrian cordierite-bearing charnockite from the Achankovil Suture Zone. The focus of the work by Santosh et al. (1993) was to understand the significance of CO_2-rich fluid inclusions and channel-trapped volatiles in cordierite. The mineralogy consists of cordierite, orthopyroxene, alkali feldspar, plagioclase and quartz, which coexist with partly consumed biotite and garnet. Microthermometric measurements performed on CO_2-rich fluid inclusions (Fig. 5C) in cordierite, quartz and garnet showed melting temperatures (T_m) close to the triple point for pure CO_2 (-56.6°C), and the fluid inclusions usually showed high densities between 0.80 and 0.95 g/cm^3, based on homogenization behavior. The higher CO_2 densities were observed in fluid inclusions in quartz and garnet, and these fluid inclusions were interpreted to have been trapped at peak metamorphic conditions by Santosh et al. (1993). Santosh et al. (1993) further suggested that CO_2 was trapped in cordierite channels and in fluid inclusions during mineral growth, and experienced little reequilibration during subsequent events. Santosh et al. (1993) did not report H_2O in the fluid inclusions.

In the present study, CO_2-rich fluid inclusions in sample NLK1/2 were analyzed by Raman spectroscopy. At room temperature the fluid inclusions showed no evidence of H_2O (Fig. 8A), whereas at 150°C a clearly-resolvable peak for H_2O was observed at ~3640 cm^{-1} (Fig. 8B).

3.2.3 Sittampundi Complex, India

The Sittampundi Complex in the Palghat-Cauvery Suture Zone of southern India is a late Archean, high-pressure and ultra-high temperature (UHT) mafic granulite retrograded to eclogite (Santosh et al., 2010). Sample STM03-1 from this complex is composed mostly of garnet porphyroblasts, plagioclase, clinopyroxene, with retrograde calcic amphibole surrounding the peak metamorphic minerals.

Santosh et al. (2010) conducted microthermometry and Raman spectroscopic analysis of fluid inclusions in sample STM03-1. The fluid inclusions are texturally primary and pseudosecondary, occurring in plagioclase, staurolite and kyanite, with secondary fluid inclusions in garnet. Fluid inclusion size ranges from 2 to 10 μm. Primary fluid inclusions are scarce, occur only in the cores of garnets, and have a negative crystal-shape. Secondary trails (Fig. 5B) in garnet are abundant and are interpreted to have been trapped prior to the formation of plagioclase. These inclusions contain dolomite and calcite as solid phases. Homogenization temperatures range from -18.9 to 24.5ºC, with melting temperatures from -56.7 to -57.4ºC. The fluid inclusions were described as high-density CO_2 (0.968-1.154 g/cm^3), containing traces of CH_4 and N_2. Santosh et al. (2010) found no evidence of H_2O during Raman analysis. These workers suggested that the CO_2 was derived from sub-lithospheric sources, possibly a carbonated sub-cratonic continental keel (tectosphere) invaded by hot asthenosphere, or underplated mafic magmas.

Fluid inclusion petrography was conducted to locate the same inclusions that were studied previously by Santosh et al. (2010). No evidence of H_2O was found in any of the fluid inclusions described as being primary by Santosh et al. (2010) when analyzed in this

study by Raman at room temperature or at 150ºC. However, during analysis of the secondary fluid inclusions in garnet at room temperature, a peak was observed at ~3671 cm^{-1} (Fig. 9). This peak disappeared when the laser spot was positioned outside of the inclusion, indicating that it was not from the garnet host. This peak is shifted to higher frequency (by about 30 cm^{-1}) compared to the position of the peak for H_2O vapor at ~3640 cm^{-1}. This peak is interpreted to represent the hydrated form of garnet, referred to as hydrogarnet (Arredondo and Rossman, 2002; Kolesov and Geiger, 2005), that formed as a thin rim on the walls of the fluid inclusion cavity. Some secondary fluid inclusions in garnet contain numerous solid phases (Fig. 5 E, F) that have been identified as Fe- Mg-, Zn- and Cu-rich carbonates, hydrogarnet, pyrophyllite, micas and probable sulfide phases based on Raman analysis.

3.2.4 Sevitturangampatti, India

Sample MD16-1G is an UHT granulite from the Palghat-Cauvery Shear Zone in Sevitturangampatti, South India. This sample was previously studied by Ohyama et al. (2008) and was interpreted to have formed at high pressure (P >12 kbar) and ultra-high temperature (T~990°C) during the collisional assembly of the Gondwana Supercontinent in the Neoproterozoic. The rock is a quartz-free Mg-Al granulite composed mainly of garnet, cordierite, gedrite, corundum, sillimanite and staurolite. Ohyama et al. (2008) described the fluid inclusions as primary CO_2-rich inclusions in plagioclase, with sizes ranging from 3 to 10 μm. Pseudosecondary and secondary CO_2 fluid inclusions ranging from 5 to 30 μm were observed in staurolite and garnet (Fig. 5D). Homogenization temperatures ranged from -25.8 to +30ºC with densities of 0.67-1.06 g/cm^3, and melting

temperatures ranged from -57.3 to -56.6ºC. The secondary inclusions showed higher homogenization temperatures, ranging from +12.9 to 30ºC, indicating a lower density of 0.59-0.83 g/cm^3. The CO_2 fluid inclusion isochores for the high-density primary inclusions intersect the peak metamorphic conditions inferred from mineralogical evidence. The CO_2 fluid inclusions trapped during formation of the plagioclase are interpreted to represent samples of the syn-metamorphic fluid that was trapped at the peak of UHT metamorphism. The secondary inclusions along trails were trapped during retrogression.

In the present study, H_2O was not detected in fluid inclusions in sample MD16-1G when analyzed at room temperature or at 150°C. However, similar to sample STM03-1A described earlier, hydrogarnet was observed in the fluid inclusions in garnet, as evidenced by a peak at ~3665 cm^{-1}. The fluid inclusions that contain the hydrogarnet are secondary, CO_2-rich, range from 5 to 40 μm, and some contain several solid phases (Fig. 5E). Some of the inclusions are irregularly shaped and others occur as randomly oriented thin tubes that appear to be recrystallized melts and show evidence of necking down. The solid phases in the fluid inclusions (obtained by Raman spectroscopy) are mainly Mg-rich carbonates, scapolite (?) and paragonite.

4. Discussion

Our data confirm that H_2O is a minor but common component in fluid inclusions that had previously been considered to contain "pure" CO_2 (or CO_2 – rich fluid) (Santosh et al., 1993; Ohyama et al., 2008; Santosh et al., 2010). The amount of H_2O in the fluid inclusions was not be quantified because we could not be certain that the inclusions had

been heated to the homogenization temperature. However, when compared to synthetic fluid inclusions with known H_2O contents, the room temperature phase ratios suggest ~5 mol% H_2O. Phase equilibria for granulites frequently indicate a_{H2O} = 0.1 to 0.4 (Bohlen et al. 1980; Philips, 1980; Valley et al, 1984; Powers and Bohlen, 1985; Bhattacharya and Sen, 1986) at the peak of metamorphism. At these P-T conditions, experimental data for the system H_2O - CO_2 reported by Newton (1986) suggest that the a_{H2O} predicted for these granulites (0.1 to 0.4) is consistent with X_{H2O} ranging from ~ 0.05 to 0.13 (5 to 13 mol % H_2O; Fig. 3), which is consistent with our observations.

The density (i.e., the molar volume) of the fluid inclusions determined from the CO_2 homogenization temperature is often used to estimate isochores and infer P-T conditions of inclusion formation. If H_2O is present in CO_2- rich fluid inclusions then, at any given temperature, pressures based on the density of pure CO_2 are lower than the actual pressures of trapping (Lamb et al. 1987). For example, Lamb et al. (1987) determined that a hypothetical mixed H_2O + CO_2 fluid inclusion containing 20 vol.% H_2O (equivalent to 36 mol % H2O) at room temperature and with a CO_2 density of 1.1 g/cm3 (see also Brown and Lamb, 1986). At 750˚C the density of this fluid would require a trapping pressure of approximately 9.5 kbars, whereas pure CO_2 with a density 1.1 gm/cm3 indicates a pressure of approximately 7.8 kbars (Brown and Lamb, 1986). In many studies, therefore, the pressures likely have been underestimated because the presence of H_2O was ignored. Clearly, accurate isochore location in P-T space requires complete characterization of the CO_2-rich inclusions in rocks from granulite terranes.

Despite the fact that H_2O fluid was not found in some of the fluid inclusions analyzed here (sample STM03-1 and MD16-1G), H_2O is present as hydrogarnet in secondary fluid

inclusions in garnet. Hydrogarnet is a hydrothermal mineral, in which the hydroxide (OH) partially replaces silica (SiO_4), the Si^{4+} missing from the tetrahedral site is replaced by bonding of a H^+ to each of the four oxygen atoms surrounding the vacant site with a reaction [$(O_4H_4)^{4-} \Leftrightarrow (SiO_4)^{4-}$] (Arredondo and Rossman, 2002; Kolesov and Geiger, 2005). This observation suggests that the original fluid contained some unknown amount of H_2O that reacted with the host to form hydrogarnet after entrapment, and explains the failure to identify fluid water in the fluid inclusions during microthermometry and/or Raman analysis at room temperature.

Some workers have suggested that the low a_{H_2O} fluids required during granulite petrogenesis are represented by high-salinity brines (Touret, 1971; Newton et al., 1980, Santosh et al., 1993; Harlov et al., 2006; Santosh and Omori, 2008; Safonov et al., 2012; Rajesh and Santosh, 2012, Rajesh et al., 2013). And, while high-salinity fluid inclusions have been reported in granulites, they are much less abundant than CO_2-rich inclusions. Watson and Brenan (1987) documented experimentally that pure CO_2 at elevated P-T conditions exhibits high dihedral angles (>60°) in quartz aggregates and hence has low infiltration ability and greater tendency to be captured during fracture healing. H_2O, in contrast, generally forms lower dihedral angles, and concentrated brines thus have enhanced wetting ability. Brines would therefore have a low tendency to be captured as fluid inclusions in the high-grade metamorphic regime. This property could account for their rarity relative to CO_2-rich inclusions. This interpretation agrees with petrographic and chemical evidence of metasomatic alteration in charnockites in the Limpopo Complex in South Africa (Touret and Huizenga, 2011; Safonov et al., 2012; Rajesh et la., 2013), where myrmekites (quartz-plagioclase intergrowths) occur along the borders of K-

feldspar and K-feldspar veins at intergrain boundaries. Touret and Huizenga (2011, 2012b) interpreted this to reflect the action of a metasomatic fluid that facilitated the exchange of K^+ for Na^+ in plagioclase, while the other major components remain unchanged. These workers also reported that amphiboles, biotite and fluorapatite are enriched in Cl, consistent with the presence of a saline brine.

Hydrogarnet in the secondary fluid inclusions in samples STM03-1A and MD16-1G represents a step- daughter mineral that formed after fluid entrapment as the fluid interacted with the host phase (Roedder, 1972; Anthony et al., 1984; Shepherd et al., 1985; Rankin et al., 1994; Van den Kerkhof and Hein, 2001). Other solids occurring in these same inclusions may also represent step- daughter minerals (rather than true daughter minerals that simply reflect saturation of the trapped fluid during cooling), and include Fe- Mg-, Zn- and Cu-rich carbonates, pyrophyllite, (scapolite?), paragonite and sulfide phases. Solid phases have been reported elsewhere in secondary trails of high-salinity fluid inclusions from high-grade metamorphic rocks, including halite, calcite and silicate minerals (pyroxene, garnet and zircon) in rocks from Bamble, Norway (Touret, 1985); halite, sylvite and nahcolite from the Front Range migmaties in Colorado, U.S.A. (Olsen, 1987); scapolite from the Proterozoic Mozambique Belt in East Africa (Pinna, 1995); scapolite, sulfates and carbonates from the Furua Complex, Tanzania (Coolen, 1980); $CaCl_2$ (DeJong and Williams, 1995) and magnetite (Williams, 1994) from Cloncurry, Queensland, Australia. The secondary fluid inclusions in samples STM03-1A and MD16-1G might be evidence for the presence of H_2O during retrogression, and might give hints about the complexity of these fluids (Newton et al., 1998). The reported mineral assemblage in many of these fluid inclusions suggests a composition not unlike

that reported for diamonds and diamond- grade metamorphic rocks (Izraeli et al., 2001; Klein-BenDavid et al., 2007; Korsakov et al., 2011).

5. Conclusions

The results presented here document that the ubiquitous CO_2- rich fluid inclusions observed in quartz in granulite facies metamorphic rocks often contain small amounts of fluid H_2O that is undetectable during routine petrography, microthermometry or Raman analysis at room temperature. When these same fluids are trapped in garnet, the H_2O component in the fluid reacts with the garnet host during retrogression to form hydrogarnet – thus the remaining fluid is essentially pure CO_2. In many studies, the pressures inferred from the densities of CO_2 in fluid inclusions have been underestimated because the presence of H_2O was not recognized.

Some secondary fluid inclusions contain abundant solid phases, suggesting that these fluid inclusions trapped saline brines at peak or near peak metamorphic conditions. As suggested by Newton et al. (1998), high-salinity brines may be responsible for the metasomatism observed in some granulites that cannot be explained either by "fluid absent" melting (Thompson, 1983) or by flushing of CO_2 from the mantle (Santosh and Omori, 2008).

Although the data reported in this study confirm previous observations that CO_2 is the dominant fluid phase preserved in granulite facies rocks, we cannot confirm that these fluids represent peak metamorphic fluids or that the fluid inclusions have not re-equilibrated following trapping. Our results are consistent with the interpretation that one process cannot explain the formation of all granulites, but that several different processes

contribute to dehydrate the lower crust, leaving behind the anhydrous mineral assemblages found in granulite facies metamorphic rocks.

Acknowledgements

The authors thank Charles Farley for assistance with the Raman analyses, and Jesse Sigman for collecting some of the Raman spectra as part of an undergraduate research project. HML and RJB thank Bob Tracy, Esteban Gazel and Mark Caddick for insights concerning the world of metamorphism. Reviews of an earlier version of this paper by T. Tsunogae and an anonymous reviewer significantly improved the presentation and interpretation. HML and RJB acknowledge support from the National Science Foundation under grant EAR-1019770. Consejo Nacional de Ciencia y Tecnología (CONACyT) and the Virginia Tech Graduate School provided partial funding to HML during this study.

References

Adar, F., Naudin,C., Whitley, A., Bodnar, R. J. (2004) Use of a microscope objective corrected for a cover glass to improve confocal spatial resolution inside a sample with finite index of refraction. *Applied Spectroscopy,* ***58***, 1136–1137.

Anthony, E.Y., Reynolds, T.J., Beane, R.E. (1984) Identification of daughter minerals in fluid inclusions using scanning electron microscopy and energy dispersive analysis. *American Mineralogist,* ***69***, 1053-1057.

Aranovich, L.Y., Newton, R.C. (1997) H_2O activity in concentrated KCI and KCI-NaC1 solutions at high temperatures and pressures measured by the brucite-periclase equilibrium. *Contributions to Mineralogy and Petrology,* ***127***, 261-271.

Arredondo, E.H., Rossman, G.R. (2002) Feasibility of determining the quantitative OH content of garnets with Raman Spectroscopy. *American Mineralogist,* ***87***, 307-311.

Bakker, R.J., Jansen, J.B.H. (1991) Experimental post-entrapment water loss from synthetic CO_2-H_2O inclusions in natural quartz. *Geochimica et Cosmochimica Acta,* ***55***, 8, 2215-2230.

Bakker, R.J., Jansen, J.B.H. (1994) A mechanism for preferential H_2O leakage from fluid inclusions in quartz, based on TEM observations, *Contributions to Mineralogy and Petrology,* ***116***, 7-20.

Barker, A.J. (1995) Post-entrapment modification of fluid inclusions due to overpressure: evidence from natural samples. *Journal of Metamorphic Geology* ***13***, 737–750.

Beere, W., (1975) A unifying theory of the stability of penetrating liquid phases and sintering pores. *Acta Metallurgica **23***, 131-138.

Bendaoud, A., Derridj, A., Ouzegane, K., Kienast, J.R. (2004) Granulitic metamorphism in the Laouni terrane (Central Hoggar, Tuareg Shield, Algeria). *Journal of African Earth Sciences, **3***, 187-192.

Berkesi, M., Szabo, C.S., Bodnar R.J., Fedele, L. (2007) CO_2- bearing fluid inclusions in upper mantle xenoliths from Tihany (western Hungary): Minimum trapping pressures and trace element compositions. *Geochimica et Cosmochimica Acta, **71***, 83.

Berkesi, M., Hidas, K., Guzmics, T., Dubessy, J., Bodnar, R. J., Szabo, C.S., Vajna, B., Tsunogae, T. (2009) Detection of small amounts of H_2O in CO_2-rich fluid inclusions using Raman spectroscopy. *Journal of Raman Spectroscopy **40***, 1461–1463.

Bhattacharya, A., Sen, S.K. (1986) Granulite metamorphism, fluid buffering, and dehydration melting in the Madras charnockites and metapelites. *Journal of Petrology **27***, 1119-1141.

Bohlen, S.R. (1991) On the formation of granulites. *Journal of Metamorphic Geology, **9**,* 223-229.

Brown, P.E., Lamb, W.M. (1986) Mixing of H_2O - CO_2 in fluid inclusions; geobarometry and Archean gold deposits. *Geochimica et Cosmochimica Acta, **50***, 847-852

Brown, M. (2007) Metamorphic conditions in orogenic belts: A record of secular change. *International Geology Review, **49***, 193–234.

Cartwright, I., Valley, J.W. (1991) Steep oxygen-isotope gradients at marble metagranite contacts in the northwest Adirondack Mountains, New York, USA: Products of fluid-hosted diffusion. *Earth and Planetary Science Letters, **107***, 148-163.

Clemens, J.D., Vielzeuf, D. (1987) Constraints on melting and magma production in the crust. *Earth and Planetary Science Letters, **86***, 287-306.

Clemens, J.D. (1990) The granulite - granite connexion. In: Vielzeuf, D., Vidal, P.H. (Eds.) Granulites and crustal evolution. Kluwer, Netherlands, 25-36.

Clemens, J.D. (1992) Partial melting and granulite genesis: A partisan overview. *Precambrian Research, **55***, 297-301.

Clemens, J.D. (1993) Experimental evidence against CO_2- promoted deep crustal melting. *Nature, **363**,* 336-338.

Clemens, J.D. (1995) Phlogopite stability in the silica-saturated portion of the system $KAlO_2$-MgO-SiO_2-H_2O- new data and a reappraisal of phase-relations to 1.5 Gpa. *American Mineralogist, **80***, 982-997.

Clemens, J.D., Droop, G.T.R., Stevens, G. (1997) High-grade metamorphism, dehydrations and crustal melting: a reinvestigation based on new experiments in the silica-saturated portion of the system $KAlO_2$-MgO-SiO_2-H_2O-CO_2 at P <= 1.5GPa. *Contributions to Mineralogy and Petrology, **129***, 308-325.

Clemens, J.D., Droop, G.T.R. (1998) Fluids, P-T paths and the fates of anatectic melts in the Earth's crust. *Lithos, **44***, 21-36.

Clemens, J.D., Watkins, J.M. (2001) The fluid regime of high-temperature metamorphism during granitoid magma genesis. *Contributions to Mineralogy and Petrology, **140***, 600-606.

Coolen, J.J.M.M.M. (1980) Chemical petrology of the Furua Granulite Complex, southern Tanzania. *Free University of Amsterdam Papers of Geology*, *Series* ***1***, 13, Amsterdam, 1-258.

Crawford, M.L., Hollister, L.S. (1986) Metamorphic fluids: The evidence from fluid inclusions. In: Walther J.V., Wood B.J. (Eds.), *Fluid-Rock Interactions During Metamorphism.* Springer-Verlag, New York, 1-35.

DeJong, G., Williams, P.J. (1995) Giant metasomatic system formed during exhumation of mid-crustal Proterozoic rocks in the vicinity of the Cloncurry Fault, northern Queensland. *Australian Journal of Earth Sciences,* ***42***, 281-290.

Dubessy, J., Boiron, M.C., Moissette, A., Monnin, C., Sretenskaya, N. (1992) Determinations of water, hydrates and pH in fluid inclusions by micro-Raman spectrometry. *European Journal of Mineralogy,* ***4***, 885-894.

Ertan, E.I., Leeman, W.P. (1999) Fluid Inclusions in mantle and lower crustal xenoliths from the Simcoe volcanic Field, Washington. *Chemical Geology,* ***154***, 83-95.

Fall, A., Tattitch, B., Bodnar, R.J. (2011) Combined microthermometric and Raman spectroscopic technique to determine the salinity of H_2O-CO_2 - NaCl fluid inclusions based on clathrate melting. *Geochimica et Cosmochimica Acta,* ***75***, 951-964.

Fyfe, W.S. (1973) Granulite facies partial melting and Archaean crust. Philosophical Transactions of the Royal Society of London. Series A, *Mathematical Physical and Engineering Sciences,* ***273,*** 457-461.

Harley, S.L. (1989) The origins of granulites: A metamorphic perspective. *Geological Magazine,* ***126***, 215-247.

Harlov, D.E. (2012) The potential role of fluids during regional granulite-facies dehydration in the lower crust. *Geoscience Frontiers,* ***3***, 813-827.

Hall, D.L., Bodnar, R.J. (1990) Methane in fluid inclusions from granulites: A product of hydrogen diffusion? *Geochimica et Cosmochimica Acta,* ***54***, 641-651.

Hall, D.L., Sterner, S.M., (1993) Preferential water loss from synthetic fluid inclusions, *Contributions to Mineralogy and Petrology,* ***114***, 489-500.

Hollister, L.S. (1990) Enrichment of CO_2 in fluid inclusions in quartz by removal of H2O during crystal-plastic deformation. *Journal of Structural Geology,* ***12***, 895–901.

Huizenga, J.M., Touret, J.L.R. (2012) Granulites, CO_2 and graphite. *Gondwana Research,* ***22***, 799-809.

Izraeli, E.S., Harris, J.W., Navon,O. (2001) Brine inclusions in diamonds: a new upper mantle fluid. *Earth and Planetary Science Letters,* ***187***, 323-332.

Kelsey, D.E. (2008) On ultrahigh-temperature crustal metamorphism. *Gondwana Research,* ***13***, 1-29.

Klein-DenDavid, O., Izraeli,E.S., Hauri, E., Navon, O. (2007) Fluid inclusions in diamonds from the Diavik mine, Canada and the evolution of diamond-forming fluids. *Geochimica et Cosmochimica Acta,* ***71***, 723-744.

Kolesov, B.A., Geiger, C.A. (2005) The vibrational spectrum of synthetic hydrogrossular (katoite) $Ca_3Al_2(O_4H_4)_3$: A low-temperature IR and Raman spectroscopic study. *American Mineralogist,* ***90***, 1335-1341.

Korsakov, A.V., Dieing, T., Golovin, A.V., Toporski, J. (2011) Raman imaging of fluid inclusions in garnet from UHPM rocks (Kokchetav massif, Northern Kazakhstan). *Spectrochimica Acta Part A,* ***80***, 88-95

Lamb, W., Valley, J.W. (1984) Metamorphism of reduced granulites in low-CO_2 vapor-free environment. *Nature,* ***312***, 56-58.

Lamb, W.M., Valley, J.W. (1985) C-O-H fluid calculations and granulite genesis. In: Tobi, A.C., Touret, J.L.R. (Eds.), *The Deep Proterozoic Crust in the North Atlantic Provinces*. Reidel, Dordrecht, 119-131.

Lamb, W.M., Valley, J.W., Brown, P.E. (1987) Post-metamorphic CO_2-rich fluid inclusions in granulites. *Contributions to Mineralogy and Petrology,* ***96***, 485-495.

Lamb, W.M., Valley, J.W. (1988) Granulite facies amphibole and biotite equilibria, and calculated peak-metamorphic water activities. *Contributions to Mineralogy and Petrology,* ***100***, 349-360.

Lamb, W.M. (1990) Fluid inclusions in granulites: Peak vs. retrograde formation. In Vielzeuf, D., Vidal, P., (Eds.) *Granulites and Crustal Evolution,* ***311***, 419-433.

Lamb, W.M., Brown, P.E., Valley, J.W. (1991) Fluid inclusions in Adirondack granulites: Implications for the retrograde P-T path. *Contributions to Mineralogy and Petrology,* ***107***, 472-483.

Moecher, D.P., Essene, E.J. (1990) Scapolite phase-equilibria: Additional constraints on the role of CO_2 in granulite genesis. *Granulites and Crustal Evolution,* ***311***, 385-396.

Moecher, D.P., Essene, E.J. (1991) Calculation of CO_2 activities using scapolite equilibria: Constraints on the presence and composition of a fluid phase during high- grade metamorphism. *Contributions to Mineralogy and Petrology,* ***108***, 219-240.

Morrison, J., Valley, J.W. (1988) Post-granulite facies fluid infiltration in the Adirondack Mountains. *Geology,* ***16***, 513-516.

Newton, R.C., Smith, J.V., Windley, B.F. (1980) Carbonic metamorphism, granulites and crustal growth. *Nature,* ***288***, 45-50.

Newton, R.C. (1986) Fluids of granulite facies metamorphism. In: Walther, J.V., Wood, B.J., (Eds.), *Fluid-Rock Interactions During Metamorphism*, Springer-Verlag, New York, 36-59.

Newton, R.C., Aranovich, L.Y., Hansen, E.C., Vandenheuvel, B.A. (1998) Hypersaline fluids in Precambrian deep-crustal metamorphism. *Precambrian Research,* ***91***, 41-63.

Newton, R.C., Manning, C.E. (2002) Experimental determination of calcite solubility in $NaCl–H_2O$ solutions at deep crust/upper mantle pressures and temperatures: implications for metasomatic processes in shear zones. *American Mineralogist,* ***87,*** 1401–1409.

Newton, R.C., Manning, C.E. (2010) Role of saline fluids in deep-crustal and upper mantle metasomatism: insights from experimental studies. *Geofluids,* ***10***, 58–72.

O'brien, P.J., Rotzler, J. (2003) High-pressure granulites: Formation, recovery of peak conditions and implications for tectonics. *Journal of Metamorphic Geology,* ***21***, 3-20.

Ohyama, H., Tsunogae, T., Santosh, M. (2008) CO_2-rich fluid inclusions in stauraolite and associated minerals in a high/pressure ultrahigh/temperature granulite from the Gondwana suture in southern India. *Lithos,* ***101***, 177-190.

Olsen, S.N. (1987) The composition and role of the fluid in migmatites, a fluid inclusion study of the Front Range rocks. *Contributions to Mineralogy and Petrology,* ***96***, 104-120.

Ouzegane, K., Bendaoud, A., Kienast, J.R., Touret, J.L.R. (2001) Pressure-temperature fluid evolution in Eburnean metabasites and metapelites from Tamanrasset (Hoggar, Algeria). *Journal of Geology,* ***109,*** 247-263.

Patiño-Douce, A.E., Johnston A.D. (1991) Phase equilibria and melt productivity in the pelitic system: Implications for the origin of peraluminous granitoids and aluminous granulites. *Contributions to Mineralogy Petrology,* ***107***, 202-218.

Percival, J.A. (1991) Granulite-facies metamorphism and crustal magmatism in the Ashuanipi complex, Quebec-Labrador, Canada. *Journal of Petrology,* ***32***, 1261-1297.

Phillips, G.N. (1980) Water activity changes across an amphibolite-granulite facies transition, Broken-Hill, Australia. *Contributions to Mineralogy and Petrology,* ***75***, 377-386.

Pinna, P. (1995) On the dual nature of the Mozambique Belt, Mozambique to Kenya. *African Journal of Earth Sciences,* ***21***, 477-480.

Powers, R.E., Bohlen, S.R. (1985) The role of synmetamorphic igneous rocks in the metamorphism and partial melting of metasediments, Northwest Adirondacks. *Contributions to Mineralogy Petrology,* ***90,*** 401-409.

Rajesh, H.M., Santosh, M. (2012) Charnockites and charnockites. *Geoscience Frontiers* ***3***, 737-744.

Rankin, A.H., Ramsey, M.H., Coles, B., Van Langevelde, F., Thomas, C.R., (1994) The composition of hypersaline, iron-rich granitic fluids based on laser-ICP and Synchrotron-XRF microprobe analysis of individual fluid inclusions in topaz, Mole granite, eastern Australia. *Geochimica et Cosmochimica Acta,* ***56***, 67-79.

Roedder, E., (1972) The composition of fluid inclusions. *USGS Professional Paper,* ***440***, Chapter JJ, 12 plates, 164 pp.

Sachs, P.M., Hansteen T.H., (2000) Pleistocene underplating and metasomatism of the lower continental crust: A xenolith study. *Journal of Petrology,* ***41***, 331-356

Santosh, M., (1992) The Adirondack Mountains: A critical look at a classic granulite fracies terrane. *Journal Geological Society of India,* ***40***, 298-298.

Santosh, M., Jackson, D.H., Harris, N.B.W., (1993) The significance of channel and fluid inclusion CO_2 in Cordierite: Evidence from carbon isotops. *Journal of Petrology,* ***34***, 2, 233-258.

Santosh, M., Tsunogae, T. (2003) Extremely high density pure CO_2 fluid inclusions in a garnet granulite from southern india. *The Journal of Geology,* ***111***, 1-16.

Santosh, M., Omori, S., (2008) CO_2 flushing: A plate tectonic perspective. *Gondwana Research,* ***13***, 86-102.

Santosh, M., Tsunogae, T., Shimizu, H., Dubessy, J. (2010) Fluid characteristics of retrogressed eclogites and mafic granulites from the Cambrian Gondwana suture zone in southern India. *Contributions to Mineralogy and Petrology,* ***159***, 349-369.

Selverstone, J. (1982) Fluid Inclusions as petrogenetic indicator in granulite xenoliths, Pali-Aike Volcanic Field, Chile. *Contributions to Mineralogy and Petrology,* ***79***, 28-36.

Shepherd, T.J, Rankin, A.H, Alderton, D.H.M. (1985) A practical guide for fluid inclusion studies. Blackie (Glasgow and New York), 239 p.
Skjerlie K.P., Patiño-Douce, A.E., Johnston A.D. (1993) Fluid absent melting of a layered crustal protolith: Implications for the generation of anatectic granites. *Contributions to Mineralogy and Petrology,* ***114***, 365-378.
Smit, C.A., Van Reenen, D.D. (1997) Deep crustal shear zones, high-grade tectonites, and associated metasomatic alteration in the Limpopo Belt, *South African Journal of Geology,* ***105***, 37-58.
Spear, F.S. (1993) Metamorphic phase equilibria and pressure-temperature-time paths. *Mineralogical Society of America*, Washington, D. C., 799 p.
Sterner S.M., Bodnar R.J. (1984) Synthetic fluid inclusions in natural quartz I. Compositional types synthesized and applications to experimental geochemistry. *Geochimica et Cosmochimica Acta,* ***48***, 2659–2668.
Sterner S.M., Bodnar R.J. (1989) Synthetic fluid inclusions. VII. Reequilibration of fluid inclusions in quartz during laboratory-simulated metamorphic uplift. *Journal of Metamorphic Geology,* ***7***, 243-260.
Sterner S.M., Bodnar R.J. (1991) Synthetic fluid inclusions in natural quartz. X. Experimental determination of P–V–T–X properties in the CO_2–H_2O system to 6 kb and 700°C. *American Journal of Science,* ***262,*** 1055–1074.
Stevens, G., Clemens, J.D. (1993) Fluid-absent melting and the roles of fluids in the lithosphere - a slanted summary. *Chemical Geology,* ***108***, 1-17.
Stevens, G., Clemens, J.D., Droop, G.T.R. (1997) Melt production during granulite-facies anatexis: Experimental data from "primitive" metasedimentary protoliths. *Contributions to Mineralogy and Petrology,* ***128***, 352-370.
Szabo, C.S., Bodnar, R.J. (1998) Fluid inclusion evidence for an upper mantle origin for green clinopyroxenes in late Cenozoic basanites from the Nógrád-Gömör Volcanic Field, North Hungary/South Slovakia. *International Geology Review,* ***40***, 9, 765-773.
Thompson, A.B. (1983) Fluid-absent metamorphism. *Journal of the Geological Society of London,* ***140***, 533–547.
Touret, J.L.R., (1971) Le faciès granulite en Norvège Méridionale. II: Les inclusions fluides, *Lithos,* ***4***, 423–436.
Touret, J.L.R., (1985) Fluid regime in southern Norway: The record of fluid incluions. In: Tobi, A.C., Touret, J.L.R. (Eds.), *The Deep Proterozoic Crust in the North Atlantic Provinces.* Reidel, Dordrecht, 517-549.
Touret, J.L.R. (2009) Mantle to lower-crust fluid/melt transfer through granulite metamorphism, *Russian Geology and Geophysiscs,* ***50***, 1052-1062.
Touret, J.L.R., Huizenga, J.M. (2011) Fluids in granulites. In: Van Reenen, D.D., Kramers, J.D., McCourt, S., Perchuk, L.L. (Eds.), Origin and Evolution of Precambrian High-grade Gneiss Terranes, with Special Emphasis on the Limpopo Complex of Southern Africa: *Geological Society of America Memoir* ***207***, 25–37.
Touret, J.L.R., Huizenga J.M. (2012a) Fluid-assisted granulite metamorphism: A continental journey. *Gondwana Research,* ***21***, 224-235.
Touret, J.L.R., Huizenga J.M. (2012b) Charnockite microstructures: From magmatic to metamorphic. *Goescience Frontiers****,*** ***3***, 745-753

Tsunogae, T., Santosh, M., Dubessy, J. (2008) Fluid characteristiscs of high to ultrahigh-temperature metamorphism in southern India: A quantitative Raman spepectroscopic study. *Precambrian Research, **168***, 198-211.

Van den Berg R., Huizenga J.M. (2001) Fluids in granulites of the Southern Marginal Zone of the Limpopo Belt, South Africa. *Contributions to Mineralogy and Petrology, **141***, 529-545.

Van den Kerkhof, A.M., Hein, U.F. (2001) Fluid inclusion petrography. *Lithos, **55**,* 27-47.

Valley, J.W., Essene, E.J. (1980) Akermanite in the cascade slide xenolith and its significance for regional metamorphism in the Adirondacks. *Contributions to Mineralogy and Petrology, **74**,* 143-152.

Valley, J.W., O'Neil, J.R. (1984) Fluid heterogeneity during granulite facies metamorphism in the Adirondacks: Stable isotope evidence. *Contributions to Mineralogy and Petrology, **85***, 158-173.

Valley, J.W. (1985) Polymetamorphism in the Adirondakcs: Wollastonite at contacts of shallowly intruded anorthosite. In: Tobi, A.C., Touret, J.L.R. (Eds.), *The Deep Proterozoic Crust in the North Atlantic Provinces.* Reidel, Dordrecht, 217-236.

Valley, J.W., Bohlen, S.R., Essene, E.J., Lamb, W. (1990) Metamorphism in the Adirondacks 2. The role of fluids. *Journal of Petrology, **31***, 555-596.

Valley, J.W. (1992) Granulite formation is driven by magmatic processes in the deep crust. *Earth Science Reviews, **32***, 145-146.

Vityk, M.O., Bodnar, R.J., Doukhan, J.C. (2000) Synthetic fluid inclusions: XV. TEM investigation of plastic flow associated with re-equilibration of synthetic fluid inclusions in natural quartz. *Contributions to Mineralogy and Petrology, **139***, 3, 285-297.

Vry, J., Brown, P.E., Valley, J.W., Morrison, J. (1988) Constraints on granulite genesis from carbon isotope compositions of cordierite and graphite. *Nature, **332***, 66-68.

Vry, J.K., Brown, P.E. (1991) Texturally-Early fluid inclusions in garnets: Evidence of the prograde metamorphic path. *Contributions to Mineralogy and Petrology, **108***, 271-282.

Wass, S.Y., Hollis, J.D. (1983) Crustal growth in south-eastern Australia: Evidence from lower crustal eclogitic and granulitic xenoliths. *Journal of Metamorphic Geology **1***, 25-45.

Waters, D.J. (1988) Partial melting and the formation of granulite facies assemblages in Namaqualand, South Africa. *Journal of Metamorphic Geology. **6***, 387-404.

Watson, E.B., Brenan, J.M. (1987) Fluids in the lithosphere 1. Experimentally determined wetting characteristics of CO_2-H_2O fluids and their implication for fluid transport, host-rock physical properties and fluid inclusion formation. *Earth and Planetary Science Letters, **85***, 497–515.

Williams, P.J. (1994) Iron mobility during synmetamorphic alteration in the Selwyn Range area, NW Queensland: implications for the origin of ironstone hosted Au Cu deposits. *Mineralium Deposita, **29***, 250-260.

Yardley, B.W.D., Graham, J.T. (2002) The origins of salinity in metamorphic fluids. *Geofluids, **2***, 249-256.

Figures

Figure 1

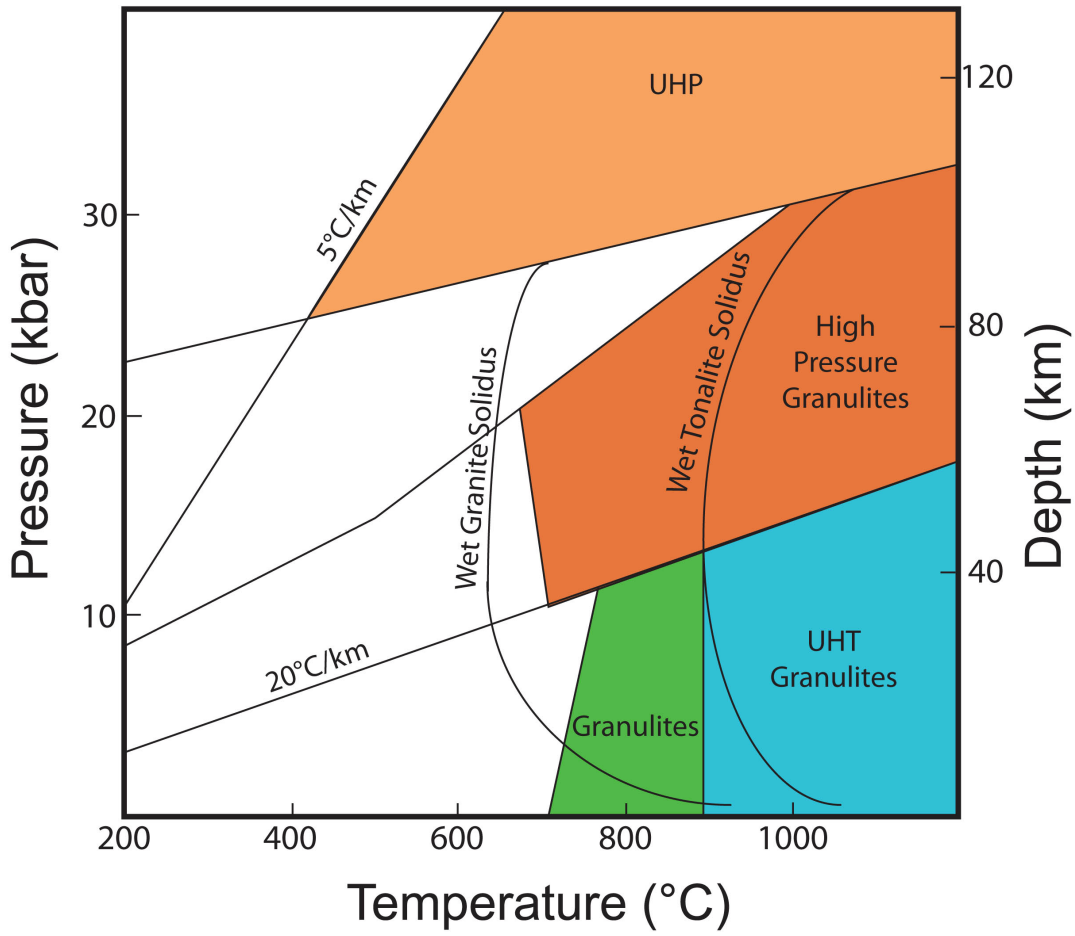

Figure 1. Classification of P-T conditions of granulite metamorphism. UHT = ultra-high temperature metamorphism; UHP = ultra-high pressure metamorphism (adapted from Brown, 2007 and Kelsey, 2008).

Figure 2

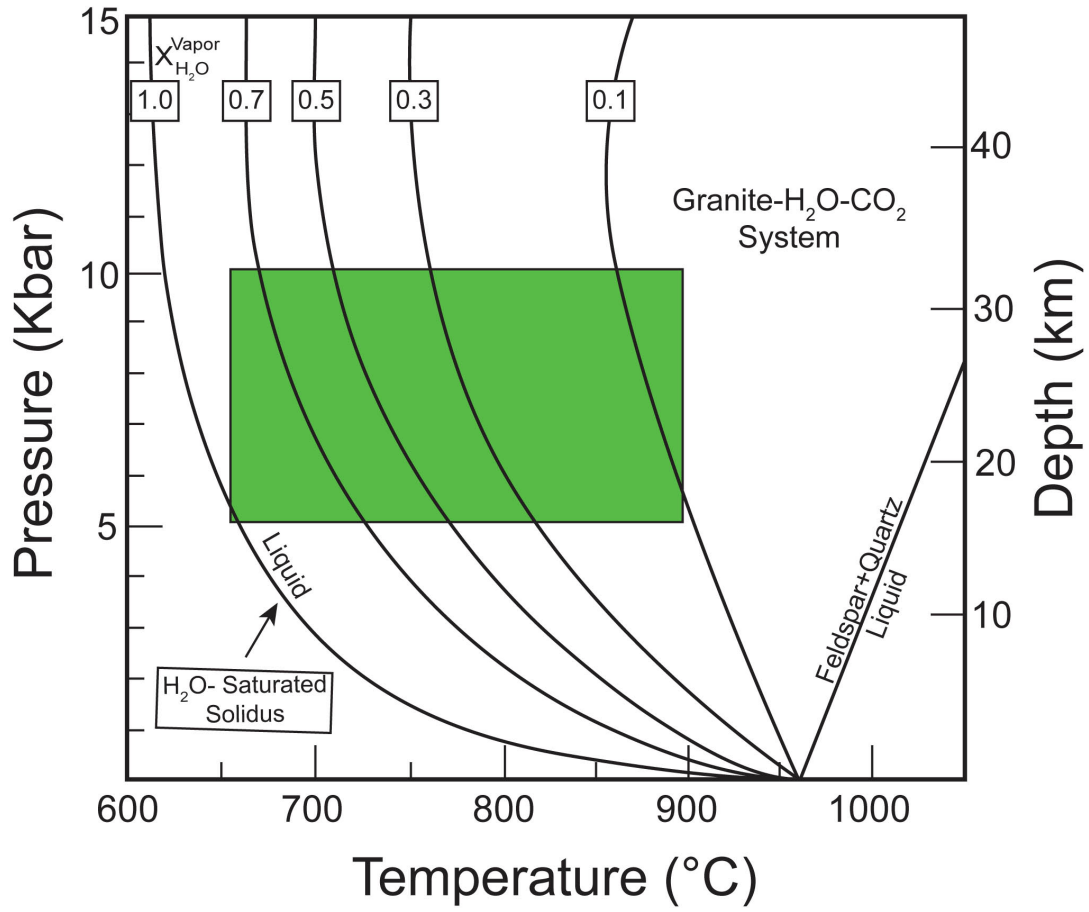

Figure 2. Solidus curves in the granite-H_2O-CO_2 system based on experimental data for the system $NaAlSi_3O_8$-H_2O-CO_2 with solidi for mole fractions of H_2O ranging from 0 to 1. The box shows the approximate P-T conditions for quartzofeldespathic granulites. Modified from Newton, 1986.

Figure 3

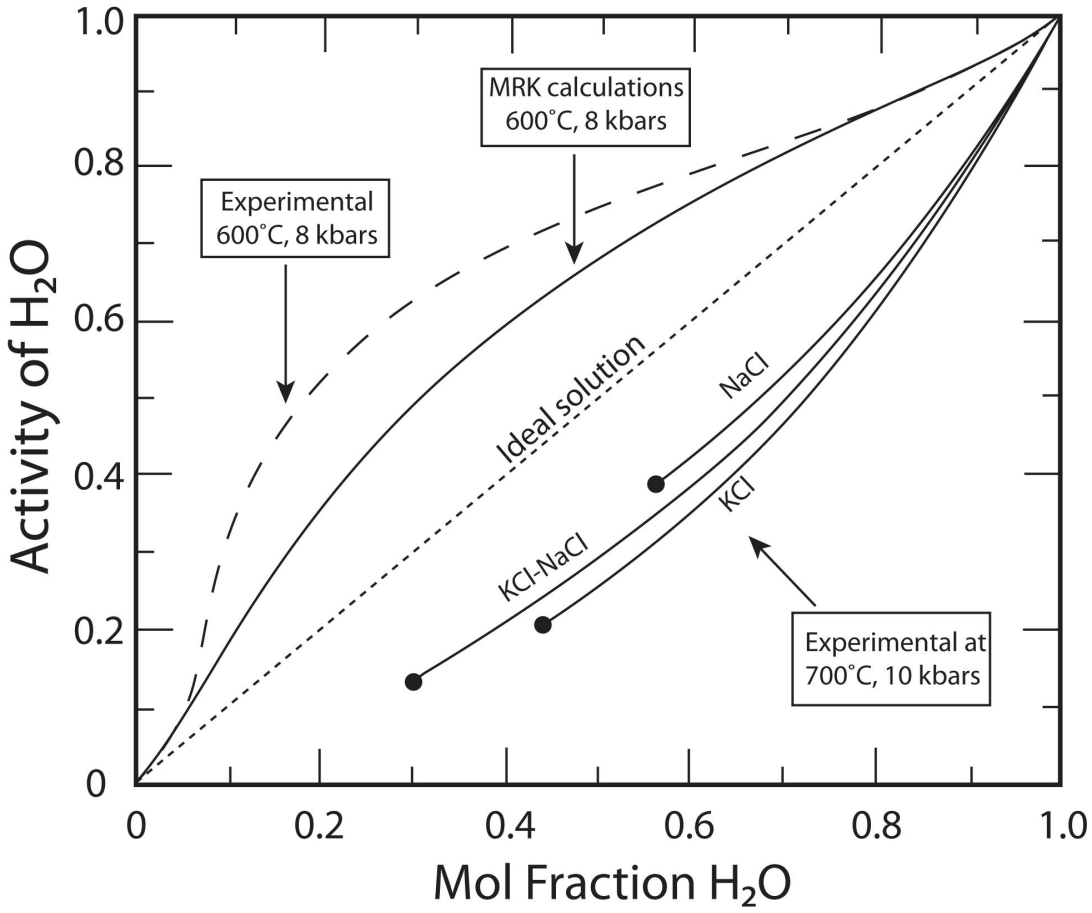

Figure 3. Activity-concentration diagram showing the relationship between the mole fraction of H_2O in the fluid and the activity of H_2O in H_2O-CO_2 fluids at 600°C and 8 kbar, estimated from experimental data and MRK calculations (Newton, 1986). The activity of H_2O is also plotted as a function of mole fraction of H_2O in NaCl-H_2O, KCl-H_2O and KCl-NaCl-H_2O fluids at 10 kbar and 700 °C (Aranovich and Newton, 1997). Both the H_2O-CO_2 and the H_2O-salt systems show a significant deviation from ideality and Aranovich and Newton (1997) proposed that the low water activity fluids associated with granulite-grade metamorphism were saline fluids rather than low-H_2O CO_2-rich fluids. The filled circles at the ends of the H_2O-salt lines represent conditions when the solutions become saturated.

Figure 4

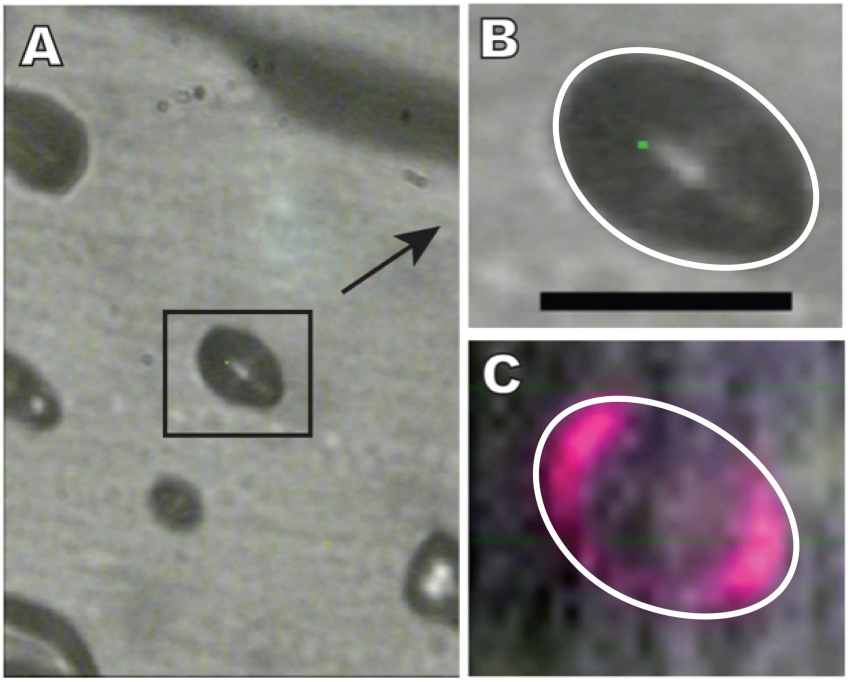

Figure 4. A) Photomicrograph of a synthetic H_2O-CO_2 fluid inclusion containing 87.5 mol% CO_2. B) Higher magnification view of the fluid inclusion showing that a separate liquid H_2O phase is not visible along the walls (scale bar =5 μm). C) Raman map of the same fluid inclusion shown in "B"; H_2O occurring as a thin film on the inclusion walls is represented by the magenta color.

Figure 5

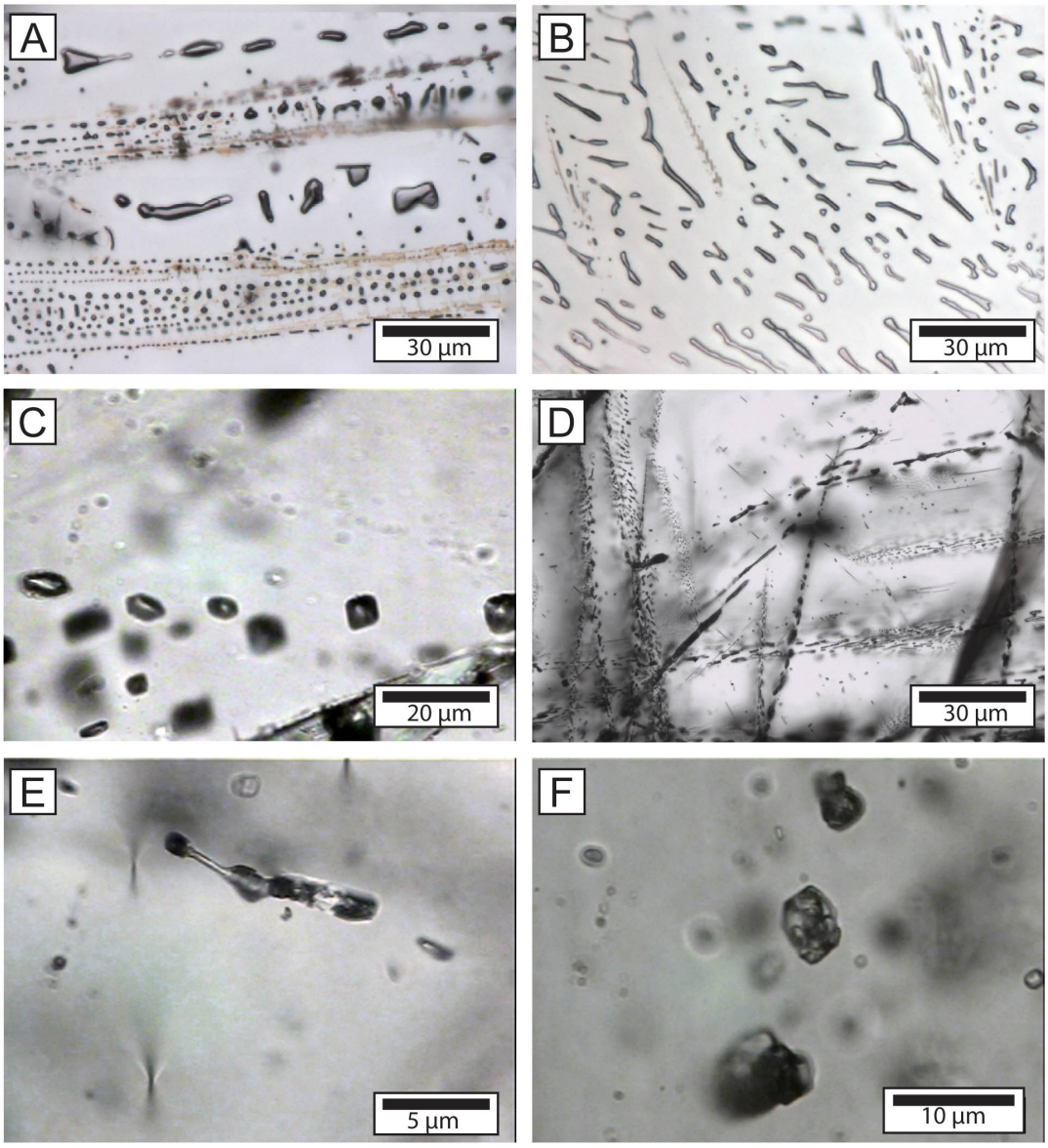

Figure 5. Photomicrographs of fluid inclusions. A) Synthetic H_2O-CO_2 fluid inclusions containing 87.5 mol% CO_2, with water recognizable only in some of the larger more elongated fluid inclusions. B) Synthetic H_2O-CO_2 fluid inclusions containing 95 mol% CO_2; none of the fluid inclusions show visible H_2O. C) Dark, single-phase fluid inclusions in sample NLK1/2. D) Secondary fluid inclusions trails in sample MD16-1G, E) Irregularly-shaped, secondary fluid inclusion with several solid phases in sample MD16-1G, F) Secondary fluid inclusions containing several mineral phases in sample STM03-1A. Hydrogarnet during Raman analysis of fluid inclusions shown in E and F.

Figure 6

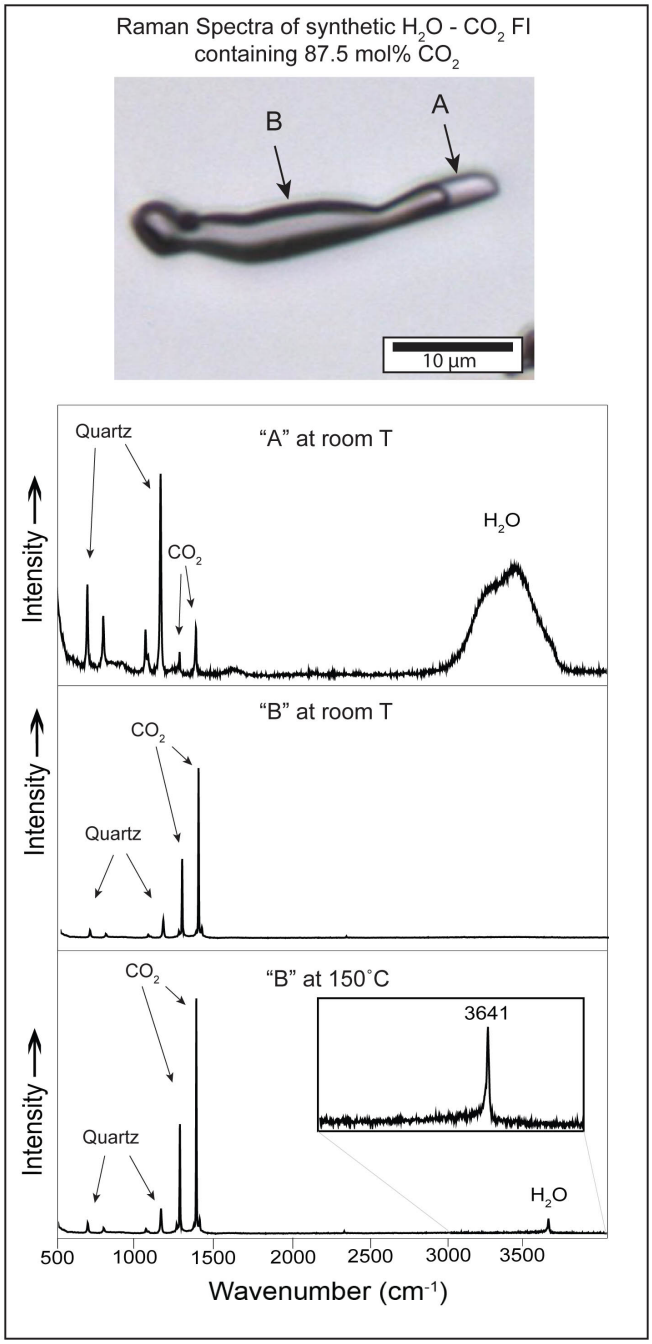

Figure 6. Raman spectra of a synthetic H_2O-CO_2 fluid inclusions containing 87.5 mol% CO_2. Raman analysis collected at room temperature at point A shows a peak for H_2O at ~ 3200 to 3500 cm^{-1}. At the same temperature, the Raman spectrum taken at point B shows the Fermi diad peaks of CO_2 at 1285 and 1388 cm^{-1}. After heating (150˚C), the Raman spectrum collected at point B shows a peak corresponding to H_2O vapor at 3641 cm^{-1}.

Figure 7

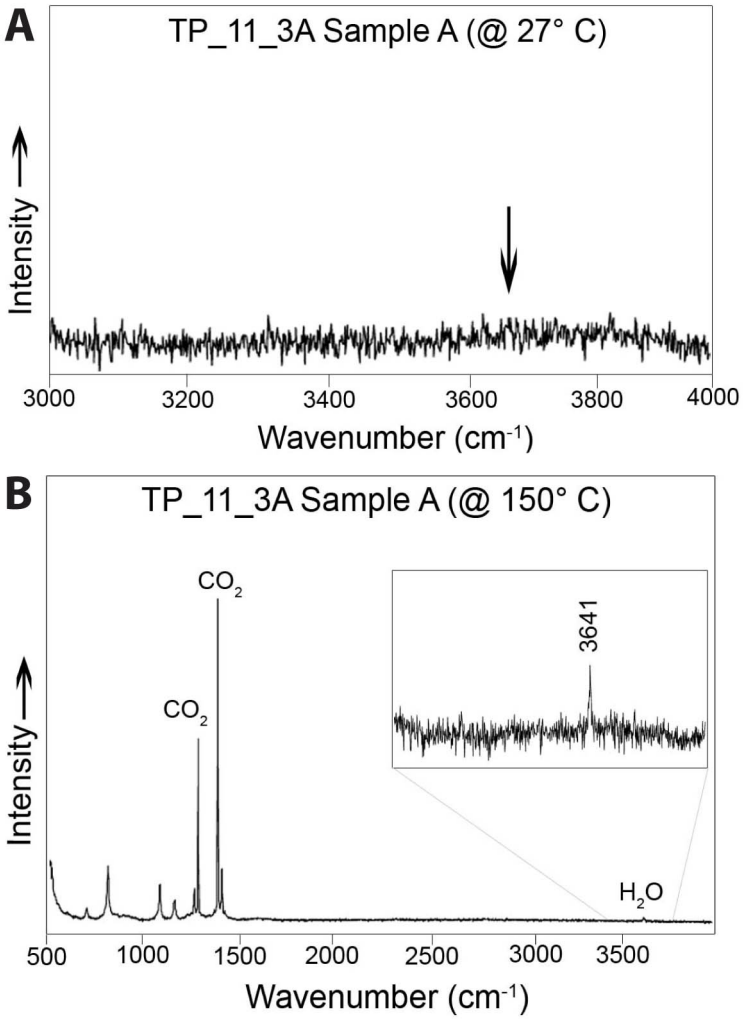

Figure 7. (A) Raman spectrum of fluid inclusions in sample TP-5 from the Adirondack Mountains collected at 27°C. The arrow shows the location for the H_2O peak, which is not observed in this inclusion when analyzed at room temperature. (B). Raman analysis of the same inclusion at 150°C. Note the small but discernible peak for H_2O at ~3641 cm^{-1}. The inset shows an enlargement of the H_2O region.

Figure 8

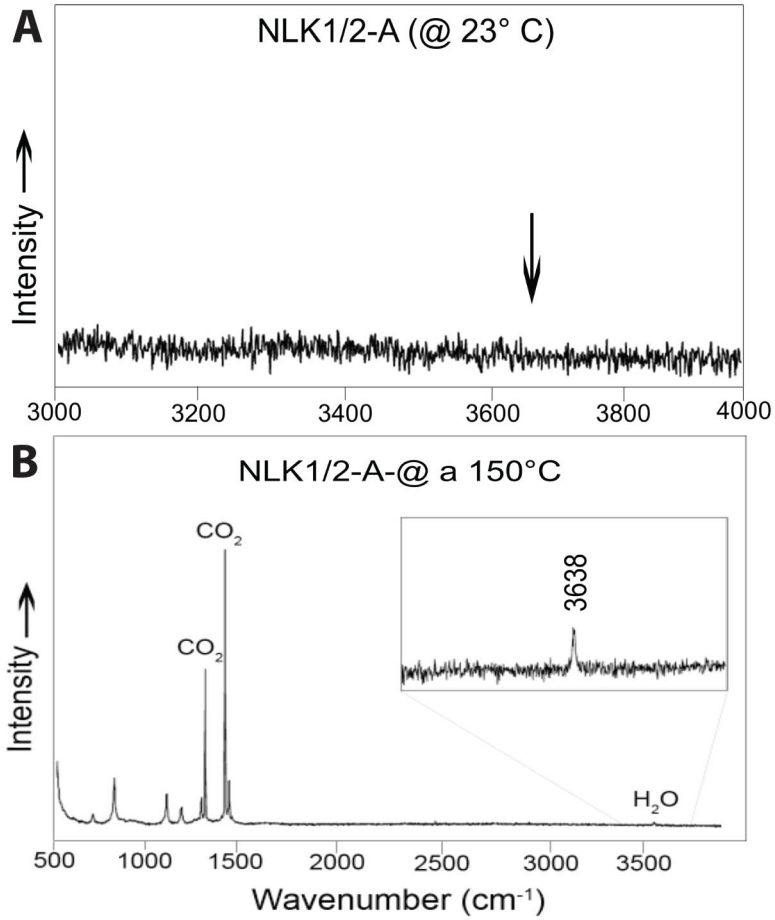

Figure 8. (A) Raman spectrum of fluid inclusions in sample NLK1/2 collected at 23°C. The arrow shows the location for the H_2O peak, which is not observed in this inclusion when analyzed at room temperature. (B). Raman analysis of the same inclusion at 150°C. Note the small but discernible peak for H_2O at ~3638 cm^{-1}. The inset shows an enlargement of the H_2O region.

Figure 9

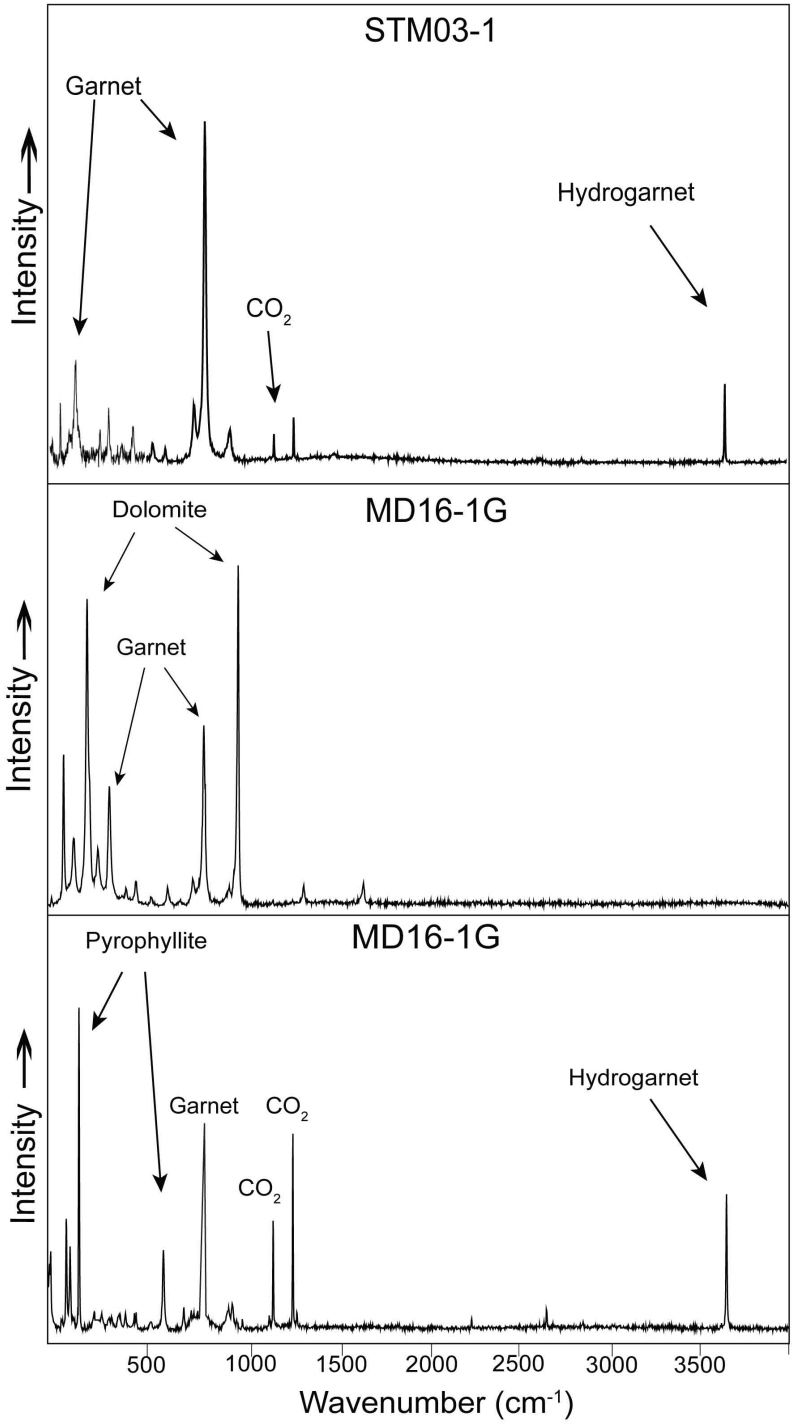

Figure 9. Raman spectra of secondary fluid inclusions in samples STM03-1A and MD16-1G. The spectra indicate the presence of several solid phases, including hydrogarnet, dolomite and pyrophyllite in the CO_2-rich fluid inclusions in garnet.

Chapter III

Reassessment of the Raman CO_2 densimeter

Lamadrid, H.M., Moore, L.R., Moncada, D., Rimstidt, J.D., Burruss, R.C., and Bodnar, R.J.

Abstract

Carbon dioxide-bearing fluids are common in many geological environments. Raman spectroscopy is sometimes used to confirm and determine concentrations of CO_2 in FI and MI, because the density of the CO_2 has an effect in the peak position of the two main peaks of CO_2 (Fermi diad). Several densimeters that use the density dependence of the Raman Fermi Diad splitting have been developed to determine the densities and concentrations of CO_2 in fluids trapped in different geological settings. It has been discussed in the literature that different densimeters will predict different densities for the same Fermi diad splitting. In this study we examine potential causes for variations in the various densimeters that have been reported in the literature by using various instrumental settings, collection parameter, different Raman instruments and analytical methods.

Twelve experiments were conducted to test the variability associated with instrumental and analytical conditions, as well as to understand the differences between the various densimeters, using three different Raman instruments, with different laser sources and gratings. All the experiments calibrated the relationship between the splitting

of the Fermi diad of CO_2 and CO_2 density at pressures from the liquid-vapor curve (6.0 MPa) to 0.06 MPa at ambient temperature (~22ºC). The results show a linear and parallel behavior where all Raman configurations have an small but constant effect in the splitting of the Fermi diad at experimental range of pressures examined here (~0.06 to 6.0 MPa). The slopes of the lines fit to our data, as well as low density (pressure) data from other densimeters (Kawakami et al., 2003; Yamamoto & Kagi, 2008; Song et al., 2009; Fall et al., 2011; Wang et al., 2011) are remarkably similar, with a variation of about ~10% and a standard deviation of 3%. The differences observed in all densimeters, including previously published densimeters and the 12 experiments from this study, are most likely a function of variations in instrumentation, laser excitation wavelength, gratings and analytical protocols used during the experimental calibration of the splitting of the Fermi diad.

1. Introduction

Carbon dioxide-bearing fluids are common in many geological environments (Roedder, 1984), including volcanic fumaroles and continental geothermal systems (Chiodini et al., 1998; Giggenbach, 1988, 1996), hydrothermal vents at mid ocean ridges (Charlou et al., 1998, 2002), in various ore-forming systems (Roedder, 1984; Bodnar, 1995; Bodnar et al., 2014; Hedenquist & Henley, 1985; Roedder & Bodnar, 1997), abbysal serpentinites (Kelley, 1996), low to high grade metamorphic rocks (Hollister and Burruss, 1976; Newton et al., 1981; Touret, 1971, 1981, 2001; Yardley, 1997), and mantle rocks sampled by upper mantle xenoliths (Roedder, 1965, 1984, 1994). Additionally, CO_2 is an important component in melt inclusions trapped during magmatic

and high-grade metamorphic processes (Wallace, 2005; Metrich & Wallace, 2008; Kent, 2008; Bartoli et al. 2013). Fluid and melt inclusions are the most reliable tools available to characterize the physical and chemical properties of paleo-crustal and mantle fluids, and much of our understanding of the pressure, density, temperature and composition of crustal (and upper mantle) fluids and melts comes from studies of fluid and melt inclusions (Roedder, 1984; Roedder & Bodnar, 1987; Frezzotti & Touret, 1994; Bodnar et al., 2014; Yardley & Bodnar, 2014; Frezzotti & Ferrando, 2015).

Numerous techniques are available to determine the presence and/or concentration of CO_2 in fluid and melt inclusions, and the choice of technique depends on several factors. Some fluid inclusions (FI) show three fluid phases when observed at room temperature (inclusions "A" and "B" in Fig. 1), consisting of liquid and vapor CO_2 and an aqueous (H_2O) phase that is saturated in CO_2. For such FI, petrographic observations confirm the presence of CO_2 and the relative amounts of CO_2 and H_2O can be determined either by analyzing the FI by Raman spectroscopy after heating it to the homogenization temperature and using the relationship between Raman peak areas and CO_2/H_2O ratio (Azbej et al., 2007) or from microthermometric data (Bakker and Diamond, 2000). Similarly, the CO_2 concentration can be estimated by measuring the homogenization temperature of the liquid and vapor CO_2 to determine the CO_2 density and then using the relative volume proportions of the CO_2 and H_2O phases to estimate the bulk composition using a mass balance approach (Bodnar, 1983). This technique works well if the FI are large enough to measure the CO_2 homogenization temperature precisely (such as FI "A" in Fig. 1). Unfortunately, for small FI (< 5 μm) and/or those in which the CO_2 liquid and vapor homogenize to the vapor phase, it is difficult to estimate the CO_2 concentration

with high precision (Rosso & Bodnar, 1995). If the CO_2 concentration and/or density in the FI are sufficiently low, the FI will not contain both liquid and vapor CO_2 at room temperature (such as FI "C" in Fig. 1). For these FI, the presence of CO_2 is sometimes indicated by the formation of a clathrate phase that melts at temperatures >0°C and/or by a "melting event" that is observed when the FI is cooled to low temperatures (<-100°C) and then heated through the CO_2 triple point temperature (-56.6°C). This same approach also applies to melt inclusions (MI), that contain low density CO_2 (Esposito et al., 2016; Moore et al., 2015; Fig. 1, inclusion "D"), such that liquid and vapor CO_2 would not be present or form during cooling of the MI.

Alternatively, Raman spectroscopy can be used to confirm the presence of CO_2, even when it is not obvious during petrographic and/or microthermometric analyses. Carbon dioxide has a characteristic Raman spectrum that contains several well-defined and relatively intense peaks, even at relatively low CO_2 densities (Fig. 1). As summarized in Rosso & Bodnar (1995), the linear CO_2 molecule has four modes of vibration: a symmetric stretching mode (v_1), an anti-symmetric stretching mode (v_3), and two bending modes (v_{2a} and v_{2b}) that have the same frequency and form a degenerate pair. According to Gordon & McCubbin (1966), the symmetric stretching mode occurs at 1332.87 cm^{-1} and this mode has nearly the same energy as the second excited state of an infrared active bending mode, v_2. Because they have nearly the same energy and the same symmetry species, they perturb each other in the excited state by a process known as Fermi resonance (Fermi, 1931). Fermi resonance causes the excited admixed states to split into two strong CO_2 lines referred to as the Fermi diad, with nominal frequencies of 1388.2 cm^{-1} (v^+; Fig. 1) and 1285.4 cm^{-1} (v^-; Fig. 1).

Some of the earliest Raman studies of the carbon dioxide molecule showed that the distance between the two peaks of the Fermi diad (peak splitting or Δ) (Fig. 1) is density (or pressure) dependent (Wright & Wang, 1973, 1975). Over the last 20-30 years several groups (Rosso & Bodnar, 1995; Kawakami et al., 2003; Yamamoto & Kagi, 2006, Song et al., 2009; Fall et al., 2011; Wang et al., 2011) have used this behavior to develop Raman densimeters that relate the splitting of the Raman Fermi diad to the density of CO_2, as summarized in Table 1 and Fig. 2A. The relationship between CO_2 density and the Fermi diad has been applied to estimate the density of carbon dioxide in FI and MI from a variety of different geological settings (Yamamoto et al., 2002; Yamamoto & Kagi, 2006, 2007; Esposito et al., 2011; Steele-MacInnis et al. 2011; Bartoli et al., 2013; Hartley et al., 2014; Moore et al., 2015). The densimeters are mathematical expressions that relate CO_2 density to the splitting of the Fermi diad (Δ , cm^{-1}). All of the densimeters show a similar trend of increasing splitting of the Fermi diad, Δ (cm^{-1}), with increasing CO_2 density. However, the CO_2 density predicted from a measured splitting of the Fermi diad shows significant variation, depending on which densimeter is used (Fig. 2A). Moreover, because all of the densimeters are described by empirical polynomial equations, none can be extrapolated with confidence beyond the density region used to develop the empirical relationships, as shown in Fig. 2B.

If the density of CO_2 in FI or MI is relatively high, such that both liquid and vapor CO_2 are present at room temperature or form during moderate cooling, the density of CO_2 phase can be estimated with reasonable confidence using a combination of petrography and microthermometry. However, if the density of CO_2 in the FI or MI is low (≤0.1-0.2 g/cm^3), such as for FI from epithermal precious metal deposits (Bodnar et al., 1985),

oceanic vents (Kelley et al., 1996) and most melt inclusions (Moore et al., 2015), these techniques cannot give a useful estimate of the CO_2 density. In addition, the inferred densities of CO_2 in FI and MI from these environments are lower than the lowest CO_2 densities used to develop most of the published densimeters. This requiring an extrapolation of the densimeters beyond the range in which they are calibrated. Finally, relatively large differences in CO_2 densities are predicted by the various densimeters at low densities (Fig. 2C). The relative difference in density between the densimeter that predicts the highest density for a given Fermi diad peak splitting (Kawakami et al., 2003) and that which predicts the lowest density for the same Fermi diad peak splitting (Wang et al., 2011) remains reasonably constant at ~0.1 g/cm^3 over the range ~0 to ~1 g/cm^3 (Fig. 2). An uncertainty of ±0.05 g/cm^3 represents a relatively small error if the density (pressure) is relatively high, and the relative error increases with decreasing density. For example, an uncertainty of ±0.05 g/cm^3 for a CO_2 density of 0.9 g/cm^3 represents a relative error of ~11% (Fig. 3A). However, the same uncertainty of ±0.05 g/cm^3 for a density of 0.1 g/cm^3 represents a relative error of ~101% (Fig. 3A). As will be discussed below, development of the CO_2 densimeter involves measuring the splitting of the Fermi diad at some known pressure. Thus, we can calculate the range (or uncertainty) in pressure required to produce a ±0.05 g/cm^3 range in density, and results of this calculation are shown on Figure 3B. Accordingly, the pressure uncertainty associated with an uncertainty in density of ±0.05 g/cm^3 for a nominal density of 1.0 g/cm^3 is ~29 MPa, and the pressure range associated with this same uncertainty in density for a nominal density of 0.1 g/cm^3 is ~4 MPa. As discussed below, a pressure error of 4 MPa is about 2 orders of magnitude greater than the error in pressure measurement during the

calibration experiments. Thus, the differences between the various densimeters are not likely associated with uncertainties in pressure determination during measurement of the Fermi diad.

It is clear from examination of the relationship between CO_2 density and the Fermi diad shown in Figure 2 that different laboratories report different relationships between these two parameters. Thus, a researcher will predict different CO_2 densities for the same measured Fermi diad splitting, depending on which densimeter is used. For example, the density of CO_2 bubble in a MI of which the splitting of the Fermi diad of 102.9 cm^{-1} will be 0.17 g/cm^3 using Kawakami et al. (2003), whereas the same splitting using Wang et al. (2011) will be 0.06 g/cm^3. The same MI would yield more than double the concentration of CO_2.

Some researchers have proposed techniques to correct for instrument dependent calibrations to obtain a universal equation that is applicable in all laboratories (Lu et al., 2007). In this study, we re-examine the relationship between splitting of the Fermi diad and CO_2 density at low CO_2 pressures (densities), extending from the CO_2 liquid vapor curve at ~6.0 MPa (density = 0.211 g/cm^3) down to 0.06 MPa (density = 0.001 g/cm^3) at room temperature (~22°C). This is the density (pressure) region in which it is difficult or impossible to determine the CO_2 density from petrographic or microthermometric analyses, and is also the region in which relative errors in density predicted by the various densimeters are largest. The results and fitted equations were compared to previously published experimental data (Kawakami et al., 2003; Yamamoto & Kagi, 2006; Song et al., 2009; Wang et al., 2011; Fall et al., 2011) to develop a densimeter for CO_2 that extends over the density range from 0.001 g/cm^3 to 0.205 g/cm^3. This density range

corresponds to a pressure range from ~9 to 860 psi (0.0621 to 5.93 MPa) at ambient temperature (~22°C).

A review of the literature indicates that the methodologies followed to develop the various CO_2 densimeters are sound, yet different densimeters predict different densities for the same Fermi diad splitting. Several previous studies of the pressure and temperature (density) dependence of Raman spectral features for volatile species (CO_2, CH_4) have acknowledged that their results follow near parallel trends to results of earlier studies (Song et al., 2009, Wang et al., 2001; Lu et al., 2007, Lin et al., 2007). These relationships have been considered to be mostly the result of: 1) variations associated with instrumentation (hardware) (Lu et al., 2007; Wang et al., 2011), 2) variations associated with data collection, calibration, and interpretation procedures (Song et al., 2009), 3) variations associated with the experimental method and EOS used to interpret the data (Song et al., 2009; Lu et al., 2007). These possibilities led us to examine potential causes for variations in the various densimeters that have been reported in the literature by using various instrumental settings and collection parameters to analyze CO_2, and to test our calibration results with those developed using other Raman instruments and analytical methods. As such, several hundred Raman analyses of CO_2 were collected at various pressures and using a variety of Raman instruments, excitation laser wavelengths and gratings.

2. Analytical Methods

The splitting of the Fermi diad in the Raman spectrum of CO_2 was calibrated as a function of pressure and temperature, using a high-pressure optical cell (HPOC) in the

Vibrational Spectroscopy Laboratory in the Department of Geosciences at Virginia Tech (Fig. 4). The experimental setup used for the measurements is similar to the one used in previous studies (Lin et al., 2007; Fall et al., 2011). Kawakami et al. (2003) and Yamamoto & Kagi (2006) describe a similar experimental technique using an HPOC to develop the calibration curve for splitting of the Fermi diad as a function of CO_2 density, which was then used to determine the densities of CO_2-rich fluid inclusions in mantle xenoliths. Song et al. (2009) determined the relationship between peak splitting and density for densities along the CO_2 liquid-vapor curve by analyzing CO_2 contained in fused silica capillary capsules (FSCC). Wang et al. (2011) used both an HPOC and FSCC to determine the relationship between peak splitting and density. The details of the experimental conditions used in these earlier studies are described in Table 2.

In this study, the optical cell (Fig. 4C, H) was connected to a manual screw press-type pressure generator (High-Pressure Equipment Model #50- 6-15; Fig. 4F). Pressure was monitored using two independent pressure transducers that were both connected to the HPOC and could be read simultaneously during the analyses. One was a Precise Instruments pressure transducer (Model 645) accurate to ±0.1% of the pressure output (pressure displayed in bars; Fig. 4B). The uncertainty in pressure for this transducer at the highest experimental pressure of 6.1 MPa (61 bars) was ±0.61 MPa (6.1 bars), and at the lowest experimental pressure of 0.1 MPa (1 bar) the uncertainty was ±0.01 MPa (0.1 bars). The second transducer that was connected to the HPOC was a Setra pressure transducer (Model 204C) accurate to ±0.25% of the pressure output (pressure displayed in psi) coupled with a Datum 2000 meter (Fig. 4D). The uncertainty for this transducer at

the highest pressure of 870 psi (6.0 MPa) was ±2.2 psi (0.01 MPa), and at the lowest pressure of 9 psi (0.06 MPa) the uncertainty was ±0.02 psi (0.0001 MPa).

Commercially supplied ultra-high purity CO_2 (99.999 % pure CO_2) (Fig. 4A) was used for the calibration experiments. The capillary system and HPOC were purged several times before each experiment to remove any other gases and/or water from the cell (Fig. 4C, H). The positions of the Fermi diad peaks were measured both along a decreasing pressure path from the CO_2 liquid-vapor curve (6.1 MPa at 22ºC) to 0.2 MPa in 0.2 MPa increments, and along an increasing pressure path from 0.1 to 6.1 MPa in 0.2 MPa increments. All spectra were collected at ambient temperature (~22°C), and the temperature of the pressure cell was recorded by an Omega type-E thermocouple, calibrated against the freezing point of H_2O at 0 °C, that was inserted into a small hole drilled into the top of the pressure cell, 10 mm deep and 5 mm laterally from the gas chamber. The accuracy of temperature measurements was estimated to be ±0.05 °C (Fall et al., 2011). Because the temperature in the cell sometimes changed by a few tenths of a degree Celsius owing to compression or expansion of the gas after the pressure was changed, the system was allowed to thermally equilibrate with ambient temperature (as shown by a constant readout from the temperature indicator) before the Raman spectrum was collected – this usually took ~10 minutes.

For the initial calibration experiments, Raman analyses were performed using a JY Horiba LabRam HR (800 mm) spectrometer (Fig. 4G), with 1800 grooves/mm gratings. The slit width was set to 150 µm, and the confocal aperture at 400 µm. Excitation was provided by a 514 nm (green) Laser Physics 100S-514 Ar+ laser. The laser output was 50 mW at the source and ~10 mW at the sample. The laser was focused through a 3.5 X

objective (N.A. = 0.10) with a working distance of ~12 mm for the pressure cell. The beam diameter for the 3.5 X objective is estimated to be on the order of 3–5 μm (Lin et al., 2007). The detector used is an electronically cooled open electrode 1024 pixel CCD. The mean value of three collections of 45 seconds each was taken to determine the Raman peak positions at each pressure. At pressures <1 MPa the collection times were increased by 30 s for every 0.2 MPa decrease in pressure to maintain good peak intensities (relative to background) to provide better fits during data analysis. The longest collection time was 300 seconds at 0.06 MPa.

In previous studies it was suggested that the absolute value of the difference in peak position (splitting) of the Fermi diad (Δ value) is sufficiently small to not be affected by the nonlinearity of the monochrometer (McCreery, 2000). Nonetheless, in order to eliminate or minimize any potential contributions to uncertainty related to Raman data reproducibility and the linearity, the following precautions were taken:

1) Small variations in the Fermi diad splitting, ranging from 0.03 to 0.06 cm^{-1}, were observed for analyses conducted at different times but at the same P-T conditions, and we tested whether this variation was associated to the non-linearity of the spectrometer. In the instrument and software used for the calibration (JY Horiba LabRam HR800 and Labspec 5), the linearity is defined by the zero position (laser line) and the *Koeff* value. Note that other Raman systems and software might have different approaches to set the linearity. The *Koeff* value is calculated using the position of some other well-known Raman line. The small variations in Fermi diad peak splitting described above were observed when the *Koeff* value or linearity was defined using the laser (Rayleigh) line (Zero value) and the position of the silicon peak (520.5 cm^{-1}, *Koeff* value). These

variations in peak splitting (0.03 to 0.06 cm^{-1}) correspond to uncertainties in density at our experimental conditions of ~0.03 g/cm^3. We note that when the positions of lines (such as the laser line and the silicon peak) are used to set the value of *Koeff* to define the linearity, the linearity is only defined in the spectral region between the two lines used to determine the linearity. As such, Lin et al. (2007) found that selecting a Raman line (band) closer to the spectral region of interest to set the *Koeff* value minimizes uncertainties generated by this random error. We, therefore, defined the linearity of the spectrometer (*Koeff* value) in the spectral region of interest using the laser (Rayleigh) line and the Ne line at 1458.58 cm^{-1}. Additionally, to better compensate for the nonlinearity of the monochrometer, two Ne emission lines (1031.42 cm^{-1} and 1458.58 cm^{-1}) were recorded *simultaneously* with the CO_2 bands using a Ne lamp that is permanently fixed into the optical path of the Raman system. It is important to note that the position of the Ne lines in our study is relative to the laser line at 514.5 nm. Anyone using a Raman spectrometer with a different laser wavelength will need to identify appropriate Ne (or other source) lines for calibration and for bracketing the Fermi diad. Using the measured splitting of the CO_2 Fermi diad (Δ) and the measured and real (known) distances between the Ne lines (427.16 cm^{-1}), the corrected splitting (real) of the CO_2 Fermi diad was determined according to the following expression:

$$\Delta_{CO_2}^{Corrected} = \left(\frac{\Delta_{Ne}^{Known}}{\Delta_{Ne}^{Measured}}\right) \Delta_{CO_2}^{Measured} \quad (1)$$

where $\Delta_{CO_2}^{Corrected}$ is the corrected splitting of the Fermi diad, Δ_{Ne}^{Known} and $\Delta_{Ne}^{Measured}$ are the known and measured distances between the 1458.58 cm^{-1} and 1031.42 cm^{-1} Ne emission lines, respectively, and $\Delta_{CO_2}^{Measured}$ is the measured splitting of the CO_2 Fermi

diad peaks (v_+ and v_-, cm^{-1}) in the Raman spectrum. The correction assumes that the separation between the known (1458.58 cm^{-1} and 1031.42 cm^{-1}) and measured positions for the Ne lines is proportional to the separation of the Fermi diad at ~1388.2 cm^{-1} and ~1285.4 cm^{-1} (Fig. 1).

2) Different Raman systems offer different methods of identifying the spectral region of interest and for collecting and compiling the spectral data. With the Raman system used in this study (JY Horiba LabRam HR), the region of interest over which the spectra are collected, *i.e.*, the spectral region that includes the Fermi diad and the Ne reference lines, can be defined using different methods. The spectral window that is sampled and recorded simultaneously by the detector varies as a function of the gratings used in the spectrometer (the system used in this study has the option of using 600, 1800 or 2400 grooves/mm gratings). Thus, in some cases it may not be possible to record spectra over the entire range of interest in one window (single window collection), and several collection windows or spectral ranges must be defined and collected and then stitched together to obtain the entire spectrum. In the JY system this method is referred to as an "extended range" collection (Labspec 5) or "multiwindow" collection (Labspec 6). The multi-window/extended window collection is an automatic function of Labspec Software that allows a spectrum to be acquired over an extended range by taking a number of individual windows and 'stitch' these together. In this study, differences in the measured Fermi diad peak splitting of 0.4 to 0.6 cm^{-1} were observed for a given P-T (density) condition when an extended window collection method was used rather than a single window collection. That is, the reproducibility was poorer if the different Raman lines were collected in different windows and at different times and the windows were then

stitched together to produce the entire spectrum, compared to collecting all lines in the spectrum simultaneously in a single window. These differences in splitting of the Fermi diad at the P-T conditions of the analyses represent uncertainties in the density of ~ 0.1 to 0.2 g/cm^3. To eliminate this contribution to uncertainty and to enhance the reproducibility in the measured Fermi diad splitting for a given pressure (density), single window collections were used after centering the spectrometer at a position (1250 cm^{-1}) such that the CO_2 Fermi diad and the two Ne bracketing lines could be collected simultaneously in the same spectral window.

In order to further test the reproducibility of the analytical method described above and to test for instrumental variations, data were collected using the HPOC on other Raman systems and on the same Raman instrument but with different laser excitation sources and/or gratings. In addition to the 514 nm laser described above, the JY Horiba LabRam HR (800 mm) Raman instrument at Virginia Tech is also equipped with a 632.9 nm He-Ne laser with a power of 20 mW at the source and ~2 mW at the sample, with 600, 1800 and 2400 grooves/mm gratings that can be used with both lasers. At the U. S. Geological Survey in Reston, VA the Fermi diad was measured at different pressures using a JY Horiba LabRam HR (800 mm) Raman system equipped with a 532.06 nm (frequency doubled Nd: YAG laser, 532.06 nm, ~20 mW output), a 5x objective, and 600 and 1800 grooves/mm gratings, and the confocal aperture was set at 100 μm. During the analyses at the USGS, it was not possible to collect spectra for the Ne lines and the Fermi diad simultaneously. The instrument calibration at the USGS followed procedures similar to those of Wang et al. (2011), with zeroth correction using the laser (Rayleigh) line set at 0.0 nm and a *Koeff* correction using the silicon peak at 520.6 cm^{-1}. The relationship

between CO_2 density and splitting of the Fermi diad was also measured on a JY Horiba Standard XploRA PLUS, equipped with 532 nm and 785 nm lasers and 600, 1800, and 2400 grooves/mm gratings. The spectral resolution varied from ~8 and 1.4 cm^{-1}, depending on the analytical settings. The slit width was set to 150 μm, and the confocal aperture was set at 400 μm. This system has a 1024 x 256 pixel TE deep air-cooled (-60°C) CCD. The same 3.5X objective (N.A. = 0.10) used for analyses at Virginia Tech was used for these measurements. The XploRA instrument uses a NIST traceable and patented "autocalibration" for all laser and grating combinations, and a manual calibration such as described above for the LabRam instruments was not possible.

The positions of all Raman lines collected using the different instrumental and analytical combinations described above were determined after baseline correction and Gaussian peak fitting using Labspec 5 software. Previous studies (Izraeli et al., 1999; Fukura et al., 2006; Lin et al., 2007) demonstrated that least-squares fitting applied to Raman spectra improves the precision by ~30 times compared to that estimated based on the detector pixel resolution, and Lin et al. (2007) reported an uncertainty in peak position of ~0.02 cm^{-1} using the same LabRam HR800 instrument and analytical and calibration procedures as described here.

3. Results

A total of 183 Raman spectra were collected over the range from ~0.2 to 6.0 MPa at room temperature (~22ºC) to determine the relationship between CO_2 pressure (density) and the distance between the peaks of the Fermi diad of CO_2 (Electronic Appendix A). We note that although all published Raman CO_2 densimeters relate the splitting of the

Fermi diad to CO_2 density, all of the densimeters were obtained by measuring the splitting of the Fermi diad as a function of the CO_2 pressure and not density. The pressure was then converted into CO_2 density using an equation of state (EOS), as described further below. The pressure range in our experiments extends from the CO_2 liquid-vapor curve (~6.0 MPa at ~22ºC) to the lowest pressure (0.06 MPa) at which the CO_2 peaks could be resolved during three consecutive collections, each consisting of 3 cycles of 45 seconds each. The difference in peak splitting of the three measurements at each pressure was generally less than ±0.02 cm^{-1}, with a standard deviation of 0.006 cm^{-1}. The difference in the measured distance between the two Ne lines (1031.42 cm^{-1} and 1458.58 cm^{-1}) used in our calibration was on average ±0.02 cm^{-1}, with a standard deviation of 0.015 cm^{-1}. The corrected values of the Fermi diad splitting ($\Delta_{CO_2}^{Corrected}$) obtained from Eq. (1) for the three different collections vary by ±0.009 cm^{-1}, with a standard deviation of 0.005 cm^{-1}. The average of the three Fermi diad peak splitting collections, $\Delta_{CO_2}^{Corrected}$, as well as experimental pressures, temperatures, densities and errors are shown in Table 3. The pressure (psi) at which the Raman spectrum was collected was fitted as a function of the corrected splitting of the Raman Fermi diad (Δ_{Real}) (Fig. 5a) using a 2nd order polynomial according to:

$$P_{psi} = -176807.6(1220.9) + 1723.55(11.88)\,\Delta_{CO_2}^{Corrected} - 1722.777(65.55)(\Delta_{CO_2}^{Corrected} - 102.866)^2 \quad (2)$$

where $\Delta_{CO_2}^{Corrected}$ is the corrected splitting of the Fermi diad in cm^{-1} and P_{psi} is pressure in psi. The standard deviation from a residual plot was calculated and an error in P_{psi} of 7

psi, and this error in pressure correspond to an uncertainty of 0.008 cm^{-1} in the Fermi diad splitting, with a R^2 of 0.997426.

We note that the relationship between Fermi diad splitting and pressure described by equation (2) is based on measurements obtained at ambient temperature (~22±1°C). Thus, equation (2) should only be used when analyzing CO_2 at room temperature, and for pressures (and densities) in the CO_2 vapor field.

In the present study, the density corresponding to the temperature and pressure condition of every analysis was calculated using the Span & Wagner (1996) EOS as implemented in the NIST online calculator (http://webbook.nist.gov/chemistry/fluid/) for thermophysical properties of fluids. Thus, as noted above, because all studies that have developed the CO_2 densimeter measured the pressure and converted this value to a density using an EOS, some variation between densimeters might be related to the choice of EOS used to convert the pressure to density (see Table 2 for a listing of the EOS used in previous studies). We note, however, that over the P-T range of this study, differences in the volumetric (Pressure-Volume-Temperature, or PVT) properties for CO_2 predicted by the various EOS are negligible, and the NIST calculator was used due to its flexibility and ease of use. Thus, differences in various densimeters shown in Figure 2 are not the result of using different EOS to interpret the PVT data for CO_2. After converting the experimental pressures (and temperatures) to density using the Span and Wagner (1996) EOS, CO_2 density was fitted as a function of the corrected splitting of the Fermi diad ($\Delta_{CO_2}^{Corrected}$) according to (Fig. 5B):

$$\rho = -36.42(0.31) + 0.355(0.003)\,\Delta_{CO_2}^{Corrected} \quad (3)$$

where ρ is density in g/cm^3 and $\Delta_{CO_2}^{Corrected}$ is the Fermi diad splitting in cm^{-1}. The standard error in ρ is 0.0037 g/cm^3, corresponding to an error of ~0.01 cm^{-1} in the Fermi diad splitting, with a R^2 = 0.995891. The densities predicted by Eq. (3) were compared to other published Raman densimeters (Fig. 6). Our revised densimeter predicts CO_2 densities that are in general agreement with results from Fall et al. (2011), Song et al. (2009), Wang et al. (2011) and Rosso & Bodnar (1995). At a given pressure and temperature, densities predicted by the Kawakami et al. (2003) and Yamamoto & Kagi (2006) densimeters are significantly higher than those predicted by our model, although we note that we have extrapolated those densimeters (especially those of Yamamoto and Kagi, 2006) well beyond the density range over which they have been calibrated. While the various densimeters predict different densities for the same measured Fermi diad splitting, the trends for all densimeters are parallel to each other and to the trend predicted by Eq. (3) (this study).

3.1 Variability associated with instrumental configuration and analytical conditions

Raman spectra of CO_2 were collected over a range of pressures extending from the pressure on the CO_2 liquid-vapor curve at ambient temperature (~22°C) (~6.0 MPa or 838 psi) to the lowest pressure at which the CO_2 Fermi diad bands could be measured (~0.01 MPa or 9 psi), to determine the relationship between CO_2 density and the splitting of the Fermi diad for 12 different Raman analytical configurations. Six of the experiments were conducted at Virginia Tech using the 514 nm and 632 nm lasers with the 600, 1800 and 2400 grooves/mm gratings; two experiments were conducted at the USGS in Reston, VA

using a JY Horiba LabRam Raman system, a 532 nm laser and 600 and 1800 grooves/mm gratings, and three experiments were conducted using the JY Horiba Standard XploRA Plus Raman system equipped with a 532 nm laser and 1800 and 2400 grooves/mm gratings, and with a 785 nm laser with 1800 grooves/mm grating. For all analyses, the measured pressures were converted to density using the Span & Wagner (1996) EOS as previously described. All results are tabulated in Table 4 and Figure 7.

4. Discussion

4.1 Variations Associated with Instrumentation (Hardware)

The comparison tests using different Raman configurations identified relatively small but systematic variations in the relationship between Fermi diad splitting and density (Fig. 7A). While the density predicted for a given Fermi diad splitting for the different instrumental combinations varies, the trends in Fermi diad splitting versus density for the various combinations are essentially parallel to each other (Fig. 7A), and over the range of conditions examined, the relationship of Fermi diad splitting to density is linear (Fig. 7B). The calculated slopes (m) for the different calibration lines vary from 0.344 to 0.394, with a standard deviation of 3.9%. This parallel behavior is similar to the trend observed for the extrapolated densimeters (Fig. 2C and 6).

The most likely reason to explain the differences observed using different Raman configurations, as well as the differences observed in the published densimeters, is the manner in which light interacts with its environment as it travels between the laser source

and diffraction gratings. Diffraction gratings used in our Raman instruments consist of a hard, optically flat surface etched with a large number of parallel and closely spaced grooves. Each grating of the same type (number of grooves per mm) is slightly different from all other gratings of that type because each is etched separately. As a result each grating disperses light (the Raman signal) at slightly different angles.

Another factor that most of the times is ignored in Raman studies and could explain some of the differences observed in between published CO_2 density calibrations is related to the ambient temperature conditions in the laboratories and their effect in spectrometer performance (Gaufes et al., 1995; Mestari et al., 1997; Fukura et al., 2006). Fukura et al. (2006) monitored the changes in the fluorescence spectrum of ruby with time (the reader is referred to Fig. 5 in Furkura et al., 2006). Their results show that changes as little as 0.8ºC in the laboratory were responsible for variation in the peak position of ~0.1 cm^{-1}. Other workers had observed changes in the range of 0.1 to 0.3 cm^{-1} per every 1ºC of room temperature change (Gaufes et al., 1995; Mestari et al., 1997). This fluctuations suggest that the room temperature changes causes the thermal expansion or contraction of spectrometer (Fukura et al., 2006).

In the Virginia Tech lab we recorded daily fluctuations in temperature in that range ~1ºC from morning to evening (12 hours). The experiments were conducted in a time frame of 30 minutes to 1 hour, were the thermal fluctuations are <0.2ºC. For our experiments the thermal variations in a daily basis do not completely explain the differences recorded.

4.2 Variations Associated with Data Collection, Calibration, Interpretation Procedures and EOS.

According to our results, the choice of grating has a relatively significant effect on the Raman spectrum. When using the same laser excitation wavelength with different gratings, we observed a correlation between different instruments and laser wavelengths (514, 532 and 632 nm). At the same CO_2 density, data collected with the 600 grooves/mm grating shows a greater splitting of the Fermi diad compared to using the 1800 and 2400 groove/mm gratings (Fig. 8A-B-C). In addition, using different Raman instruments but with similar excitation wavelength (532 nm) and gratings (1800 grooves/mm) produces similar peak splitting versus density relationships (Fig. 8A).

The effectiveness of using known positions of Ne lines to correct peak positions was tested using four different Raman combinations, including the 514 and 632 nm lasers with the 600 and 1800 grove/mm gratings. Since the Raman shift depends on the laser wavelength, the Ne lines used with the 514 nm laser (1031.42 and 1458.58 cm^{-1}) were not at the same position as the lines for analyses with the 632nm laser (1371.28 and 1582.54 cm^{-1}). In all cases, using the Ne lines to correct the positions of the Fermi diad lines and, therefore, the splitting of the Fermi diad, shifts the data points closer to values predicted by Eq. (3) (Fig. 8D-E-F). The 600 gratings result in lower spectral resolution and larger errors associated with fitting the less intense peaks at low pressure (density).

The reproducibility and linearity inconsistencies observed using the single vs. extended or multiwindow methods described above were observed in all of the Raman instruments tested. The distance between the peaks of the Fermi diad at 600 psi and ambient temperature was measured using single window and extended/multiwindow in consecutive collections. For the USGS Raman system (532 nm laser and 1800 gratings)

the variation in the splitting of the Fermi diad for different collections was between 0.4 and 0.6 cm^{-1}, and with the XploRA system (532 nm laser and 1800 gratings) the variation in peak splitting was between 0.3 and 0.5 cm^{-1}, similar to what was observed using the Virginia Tech JY Horiba LabRam system.

Differences associated with the single window – multi-window collection protocol might explain reported differences in published the densimeters of Song et al. (2009) and Wang et al. (2011). Both studies used the same Raman instrument at the U.S. geological Survey, and with the same laser source and gratings, and both used FSCC to contain the sample to measure the CO_2 spectra. However, Song et al. (2009) acquired the Raman spectra over the range (1200 to 1500 cm^{-1}), whereas Wang et al. (2011) collected the spectra in a single window between 1175 and 1619 cm^{-1} (the size of a single window collection using a 532 nm laser with 1800 grating). Owing to the manner in which the software controls the collection parameters, when the beginning and ending wavenumber range are defined, as in Song et al. (2009), the system uses a multi-window collection protocol. The difference in the Song et al. (2009) and Wang et al. (2011) densimeters is greater than expected when data are collected using the same Raman instrument, laser wavelength and grating, and can be explained by the use of multiple/extended window versus single window collection protocols (compare Fig. 2C). The software automatically adjusts and overlaps to a certain degree the individual windows, a process that produces errors in the linearity of the spectra. This problem can be avoided by using the single window collection method, or by using two reference lines (such as the Ne lines) to set the linearity of the spectrometer as was done in this study.

As noted above, during calibration to develop the densimeters, the pressure corresponding to a given Fermi diad peak splitting is known, and this value is converted to density using an equation of state (EOS). Here, we consider whether the differences in densimeters could be the result of which EOS was used to interpret the PVT data. Kawakami et al. (2003) and Yamamoto & Kagi (2008) used the Pitzer & Sterner (1994) EOS to calculate the CO_2 density corresponding to the PT conditions at which the Raman spectrum was collected, while the rest of the studies used the Span & Wagner (1996) EOS. The differences in density calculated at the same temperature from 0.1 MPa to 200 MPa using Pitzer & Sterner (1994) and Span & Wagner (1996) EOS are less than 1%, with a standard deviation of 0.43%. The difference is negligible and cannot account for the differences observed between the Kawakami et al. (2003) and Yamamoto & Kagi (2008) data sets and data from other studies described above.

4.3 Temporal Variations

The calibration experiments used to develop the densimeter described by equation (3) were conducted in October 2014. In an effort to understand the long-term reproducibility of the densimeter calibrated at Virginia Tech, a second calibration experiment was conducted in September 2015 using the same Raman setup and collection protocols used to determine the densimeter described by Eq. (3). The September 2015 data show almost perfect correlation with the October 2014 data (Fig. 9A). The maximum deviation between the data sets was about 0.02 cm^{-1}, corresponding to a density variation of 0.003 g/cm^{-1}, with a standard deviation of ~0.004 cm^{-1} or 0.001 g/cm^{-1}. The difference in the slopes of the densimeters was 2.8%.

In addition to these two calibrations that were done over the complete range of pressures and densities in the CO_2 vapor field at ambient temperature, the Fermi diad was measured episodically at a fixed pressure, using the same instrumental settings (514 nm laser, and 1800 gratings) and collection protocols used to develop the densimeters. Figure 9B shows the variations found in the splitting of the Fermi diad at 500 psi (3.5 MPa) and ambient temperature over the course of one year. The average Fermi diad peak splitting for 12 different measurements was 102.93 cm^{-1}, with a maximum deviation of 0.02 cm^{-1} equivalent to error in density of 0.002 g/cm^3 with a standard deviation of 0.007 cm^{-1} equivalent to 0.001g/cm^3.

We further examined temporal variations in the relationship between Fermi diad peak splitting and density by comparing calibrations conducted on the same Raman instrument and with the same hardware combinations (gratings, laser, etc.), and using the same analytical protocols, but at different times. For example, the relationship between Fermi diad peak splitting and density was determined at Virginia Tech using the JY Horiba LabRam HR800 instrument with 514 nm laser with 1800 grating, and was also determined approximately 4 years earlier by Fall et al. (2011) using the same configuration and instrument (Fig. 9C). As shown, the results for the 2011 calibration (Fall et al., 2011) and those for the more recent calibration (labeled "VT 514 nm 1800g" in Figure 9C) are essentially identical. The same consistency for the relationship between Fermi diad peak splitting and density with time is observed between data collected in 2015 as part of this study (labeled "USGS 532 nm 1800g" in Figure 9C) using the USGS Raman JY Horiba LabRam HR800 system with 532 nm laser and 1800 gratings and the

previously published data from Wang et al. (2011) obtained using the same configuration and instrument (Fig. 9C).

4.4 Universal Calibration Method

The results of this study show that instrumental as well as calibration and data collection protocols produce measureable and consistent differences in relationships that express the CO2 density as a function of the Fermi diad peak. This suggest that each laboratory will need to construct a calibration curve that is specific to their instrument as has been done in this and others studies (Rosso & Bodnar, 1995; Kawakami et al., 2003; Yamamoto & Kagi, 2008; Song et al., 2009; Fall et al., 2011; Wang et al., 2011). Moreover, the calibration should be confirmed before each analytical session using an HPOC, FSCC or synthetic fluid inclusions of known CO_2 density. However, not all Raman laboratories have access to a HPOC, FSCC or a set of synthetic fluid inclusions. Therefore, we propose an alternative method to calibrate the Raman instrument to determine the density as a function of the splitting of the Fermi diad of CO_2 for densities $\leq$0.2 g/cm^3 that requires only a single sample with known CO_2 density. Errors in density obtained from this alternate method will be larger than those associated with a full calibration, but will be significantly smaller compared to using a randomly selected densimeter from the literature, and may be acceptable in some circumstances.

In this study, 12 calibrations were preformed using different Raman instruments and combinations of lasers and gratings, and we assume that the various combinations and configurations are generally representative of the various instrumental and configuration combinations available in most laboratories. The data from each of these various calibration experiments were fit to linear equations. In addition, the data from Kawakami

et al. (2003), Song et al. (2009), Fall et al. (2011) and Wang et al. (2011) that were in the density range ~0.0 to 0.2 g/cm^3 were also fit to straight line equations, resulting in 16 equations (Table 4) of the form:

$$\rho = m\ \Delta_{CO_2}^{measured} + b \quad (4)$$

where ρ is the density, m is the slope of the calibration line, $\Delta_{CO_2}^{Measured}$ is the measured splitting of the Fermi diad of CO_2 in wavenumbers (cm^{-1}) and *b* is the intercept. Then, the average slope of the densimeter, *m*, and the average intercept, *b*, were determined and these values were used to define a universal densimeter. The average (universal) slope and average (universal) intercept can then be used to determine the density according to:

$$\rho_U = (m_u\ \Delta_{CO_2}^{measured}) + b_u \quad (5)$$

where ρ_U is the density calculated from the universal densimeter in g/cm^3, m_u = 0.36628981 g/cm^3/cm^{-1} and b_u= -37.60344 g/cm^3 are the average slope and intercept, respectively, of all the densimeter equations listed Table 4, and $\Delta_{CO_2}^{measured}$ is the measured splitting of the Fermi diad.

Equation (5) above and the linear and parallel behavior observed for the various densimeters may be now used to define a densimeter that is applicable to a particular Raman instrument. To construct a calibration curve (densimeter) with the same form of Eq. (5), a single sample (natural fluid inclusion, synthetic fluid or melt inclusion, fused silica capillary capsule or similar sample) with a known CO_2 density (ρ_S) ≤0.2 g/cm^3 is required. (1) Determine the splitting of the Fermi diad ($\Delta_{CO_2}^{measured}$) following the procedures outlined in the analytical methods sections (single window, Ne lines or other

peak position calibration method that can bracket the Fermi diad, etc.). (2) Calculate the density corresponding to this measured peak splitting is calculated using the Universal Densimeter (Eq. 5). (3) Calculate the difference between the density predicted by the Universal Densimeter and the known density of the standard defines $\Delta\rho$ (g/cm^3) :

$$\Delta\rho = \rho_S - \rho_U \quad (6)$$

where $\Delta\rho$ is the density difference (g/cm^3) between the known CO_2 density and the one predicted by the Universal Densimeter.

As an example of the application of the methodology using a single standard, assume that a CO_2 sample with a known density ρ_S= 0.1 g/cm^3 shows a Fermi diad splitting of 102.95 cm^{-1} (Fig. 10A). The Universal Densimeter (Eq. 5) (red line in Fig. 10A-C) predicts a density ρ_U= 0.1061 g/cm^3 for the measured peak splitting. If one assumes that the slope of the Universal Densimeter and the slope of the line expressing the relationship between Fermi diad splitting and density measured on the Raman system of interest are identical (blue line in Fig. 10 A-C), the Universal Densimeter may be translated in Δ- ρ (peak splitting-density) space to provide a densimeter appropriate to the Raman instrument on which the standard was analyzed. Then, one need only measure the Fermi diad peak splitting of some unknown sample, calculate the CO_2 density using the Universal Densimeter (Eq. 5), and then correct this density using the measured difference between the standard and predicted density or, as in this example, $\Delta\rho$ = -0.061 g/cm^3 (Fig. 10A).

As noted above, while the slopes of the various densimeters from the literature and those from this study are approximately parallel to each other, the slopes do show some

small variation, as listed in Table 4 and shown in Figure 10A. Owing to the different slopes, the density of the unknown at the measured peak splitting will vary from the calculated density, and the magnitude of the difference will vary as a function of the difference between the measured peak splitting for the standard and that for the unknown ($\Delta\nu$). Because the absolute difference in density between the densimeter corresponding to the shallowest slope and that corresponding to the steepest slope increases with increasing $\Delta\nu$ (Fig. 10C):

$$\sigma\rho_{max} = \Delta\nu(m_{universal} + m_{max}) \quad (7)$$

$$\sigma\rho_{min} = \Delta\nu(m_{universal} + m_{min}) \quad (8)$$

where $\sigma\rho_{max}$ and $\sigma\rho_{min}$ are the uncertainties (in g/cm^3) corresponding to the maximum and minimum slopes from Table 4, $\Delta\nu$ is the difference in splitting of the Fermi diad measured for the standard and that measured for the unknown (Fig. 10C). Table 5 lists the density corrections corresponding to various values of $\Delta\nu$ ranging from 0 cm^{-1} (zero) to the largest expected difference (~0.7 cm^{-1}) over the density range ~0 to 0.21 g/cm^3.

To accommodate for the variation in slope, the calibration methodology requiring one standard is modified slightly, as follows. First, determine the density corresponding to the measured Fermi diad peak splitting using the Universal Densimeter – for example $\rho_{unknown}$ corresponding to a measured peak splitting of 102.7 cm^{-1} (Fig. 10B). A complete list of densities predicted by the Universal Densimeter for various measured Fermi diad splittings ranging from 102.65 cm^{-1} to 103.22 cm^{-1} are listed in Table 6. Depending on the actual slope of the densimeter on the Raman instrument being used, the actual density may be greater than, less than, or equal to the density predicted by the Universal Densimeter (Fig. 10B). Finally, it should be noted that the slope of the

Universal Densimeter does not lie equi-distant between the maximum and minimum slopes for the various densimeters, so the "positive" deviation and "negative" deviation from the Universal Densimeter are not equal (Fig. 10C). For example, if the standard shows a Fermi diad peak splitting of 102.95 cm^{-1}, and the measured peak splitting for the unknown was 102.7 cm^{-1}, the difference ($\Delta\nu$) is 0.25 cm^{-1}. Extrapolation of the maximum and minimum densimeter slopes according to Eq. 7 and 8 results in densities that differ from that predicted by the Universal Densimeter by +0.0055 and -0.0068 g/cm^3 (Fig. 10C). Thus, adding and subtracting these values from the density predicted by the Universal Densimeter (0.1061 g/cm3) gives a range in densities from 0.0993 to 0.1116 g/cm3. Finally, subtracting the difference in density predicted from the Universal Densimeter ($\rho_{universal}$) and that of the standard at the same measured Fermi diad splitting gives a final estimated density of the unknown ranging from 0.093 to 0.106 g/ cm^3.

5. Summary and Recommendations

We experimentally calibrated the relationship between the splitting of the Fermi diad of CO_2 and CO_2 density at pressures from the liquid-vapor curve (6.0 MPa) to 0.06 MPa at ambient temperature (~22ºC). Twelve experiments were conducted to test the variability associated with instrumental and analytical conditions, as well as to understand the differences between the various densimeters, using three different Raman instruments, with different laser sources and gratings.

All densimeters show a linear and parallel behavior throughout the experimental range of pressures examined here (~0.06 to 6.0 MPa). The slopes of the lines fit to our

data, as well as low density (pressure) data from other densimeters (Kawakami et al., 2003; Yamamoto & Kagi, 2008; Song et al., 2009; Fall et al., 2011; Wang et al., 2011) (Table 4) are remarkably similar, with a variation of about ~10% and a standard deviation of 3%. The differences observed in all densimeters, including previously published densimeters and the 12 experiments from this study, are most likely a function of variations in instrumentation, laser excitation wavelength, gratings and analytical protocols used during the experimental calibration of the splitting of the Fermi diad.

Based on the results of this examination of the various factors that affect the relationship between Fermi diad splitting and CO_2 pressure, the authors recommend the following protocol for developing a densimeter.

1) We advise against randomly selecting a densimeter from the literature to interpret the Raman data. The most reliable densimeters will be those that are developed on the Raman instrument that will be used to analyze unknowns, following the calibration procedures used in this study. This requires access to samples or equipment that allow the splitting of the Fermi diad to be measured over the complete range of PTX conditions over which the densimeter is to be applied.

2) The linearity of the Raman spectrometer should be determined using positions of known lines (peaks) that bracket or include the spectral region of interest.

3) The Raman spectrum should be obtained using single window and Ne lines (or some other well-known Raman lines) should be collected simultaneously with the Fermi diad spectrum. To develop the densimeter described here, we selected a spectral window such that the CO_2 Fermi diad and the bracketing Ne lines (1031.42 cm^{-1} and 1458.58 cm^{-1}) were within the same window. Following baseline correction, the peaks of the Fermi

diad and the Ne lines were fitted using a Gaussian fit to determine the Fermi diad splitting corrected for the non-linearity of the spectrometer in the spectral region of interest.

4) If an experimental calibration of the Raman instrument over the complete range of pressures of interest is not possible, we suggest using the method that requires availability of only a single sample of known density (natural fluid inclusion, synthetic fluid inclusion, or fused silica capillary capsule). Combining the data obtained from analysis of this single sample with the average slope of all densimeters described above, one can extrapolate to other values of Fermi diad splitting and density. The magnitude of the error associated with this approach increases as the difference in density (and measured Fermi diad splitting) of the single standard used for calibration and that of the unknown increases.

Acknowledgements

The authors thank Charles Farley for assistance with the Raman analyses, and Matt Steele-MacInnes for discussions about Raman spectroscopy and the CO_2 Fermi Diad. HML acknowledge support from the National Science Foundation under grant OCE-1459433. Consejo Nacional de Ciencia y Tecnología (CONACyT) and the Virginia Tech Geosciences Department and Virginia Tech Graduate School provided partial funding to HML during this study.

References

Azbej, T., Severs, MJ., Rusk, B.G. & Bodnar R.J. (2007) In situ quantitative analysis of individual H_2O-CO_2 fluid inclusions by laser Raman spectroscopy. *Chemical Geology*, ***237*** (3-4), 255-263

Bakker, R.J., & Diamond, L.W. (2000) Determination of the composition and molar volume of H_2O-CO_2 fluid inclusions by microthermometry. *Geochimica et*

Cosmochimica Acta, ***64*** (10), 1753-1764.

Bartoli, O., Cesare, B., Poli, S., Bodnar, R. J., Acosta-Vigil, A., Frezzotti, M. L., & Meli, S. (2013) Recovering the composition of melt and the fluid regime at the onset of crustal anatexis and S-type granite formation. *Geology*, ***41*** (2), 115-118.

Bodnar, R.J. (1983) A method of calculating fluid inclusion volumes based on vapor bubble diameters and P-V-T-X properties of inclusion fluids. *Economic Geology*, ***78*****,** 535-542.

Bodnar, R.J., Reynolds, T.J., & Kuehn, C.A. (1985) Fluid inclusion systematics in epithermal systems. in, Geology and Geochemistry of Epithermal Systems, B.R. Berger & P.M. Bethke, eds., Society of Economic Geologists, *Reviews in Economic Geology, **2***, 73-98.

Bodnar, R.J. (1995) Fluid inclusion evidence for a magmatic source for metals in porphyry copper deposits. In Magmas, Fluids and Ore Deposits (ed. J. F. H. Thompson). *Mineral Association of Canada Short Course*, ***23***, 139–152.

Bodnar, R. J., Lecumberi-Sanches, P., Moncada, D., & Steele-MacInnis, M. (2014) Fluid inclusions in hydrothermal ore deposits. *In Treatise on Geochemistry 2nd Edition* (pp. 119-142).

Charlou, J. L., Donval, J. P., Fouquet, Y., Jean-Baptiste, P., & Holm, N. (2002) Geochemistry of high H_2 and CH_4 vent fluids issuing from ultramafic rocks at the Rainbow hydrothermal field (36° 14′ N, MAR). *Chemical Geology*, ***191*** (4), 345-359.

Charlou, J. L., Fouquet, Y., Bougault, H., Donval, J. P., Etoubleau, J., Jean-Baptiste, P., & Rona, P. A. (1998) Intense CH_4 plumes generated by serpentinization of ultramafic rocks at the intersection of the 15° 20′ N fracture zone and the Mid-Atlantic Ridge. *Geochimica et Cosmochimica Acta*, ***62*** (13), 2323-2333.

Chiodini, G., Cioni, R., Guidi, M., Raco, B., & Marini, L. (1998) Soil CO_2 flux measurements in volcanic and geothermal areas. *Applied Geochemistry*, ***13*** (5), 543-552.

Chou, I. M., Pasteris, J. D., & Seitz, J. C. (1990) High-density volatiles in the system COHN for the calibration of a laser Raman microprobe. *Geochimica et Cosmochimica Acta*, ***54*** (3), 535-543.

Diamond, L.W. (2003) Introduction to gas-bearing, aqueous fluid inclusions. *Fluid Inclusions: Analysis and Interpretation (eds. I. Samson, A. Anderson and D. Marshall)*. *Mineralogy Association of Canada Short Course, **32***, 101–158.

Dixon, J. E., Stolper, E. M., & Holloway, J. R. (1995) An experimental study of water and carbon dioxide solubilities in mid-ocean ridge basaltic liquids. Part I: calibration and solubility models. *Journal of Petrology*, ***36*** (6), 1607-1631.

Dixon, J. E., & Stolper, E. M. (1995) An experimental study of water and carbon dioxide solubilities in mid-ocean ridge basaltic liquids. Part II: applications to degassing. *Journal of Petrology*, ***36*** (6), 1633-1646.

Esposito, R., Lamadrid, H.M., Danyushevsky, L.V., Redi D., Steele-MacInnis, M., Bodnar, R.J., Manning, C.E., De Vivo, B., Cannatelli, C., Lima, A.: Detection of liquid H2O in vapor bubbles in melt inclusions: implications for magmatic fluid composition and volatile budgets of magmas? Manuscript in press in American Mineralogist DOI:10.2138/am-2016-5689

Esposito, R., Bodnar, R.J., Danyushevsky, L.V., De Vivo, B., Fedele, L., Hunter, J. & Shimizu, N. (2011) Volatile evolution of magma associated with the Sochiaro eruption in the Phlegrean Volcanic District (Italy). *Journal of Petrology*, ***52***, 2431-2460

Fall, A., Tattitch, B., & Bodnar, R.J. (2011) Combined microthermometric and Raman spectroscopic technique to determine the salinity of H2O-CO2-NaCl fluid inclusions based on clathrate melting. *Geochimica et Cosmochimica Acta*, ***75***, 951-964.

Fermi, E. (1931) Über den Ramaneffekt des kolendioxyds. *Z. Phys.* 71, 250–259.

Frezzotti, M. L., & Ferrando, S. (2015) The chemical behavior of fluids released during deep subduction based on fluid inclusions. *American Mineralogist*, ***100*** (2-3), 352-377.

Frezzotti, M. L., Touret, J. L., Lustenhouwer, W. J., & Neumann, E. R. (1994) Melt and fluid inclusions in dunite xenoliths from La Gomera, Canary Islands: tracking the mantle metasomatic fluids. *European Journal of Mineralogy*, 805-818.

Fukura S., Mizukami T., Odake S. & Kagi H. (2006) Factors determining the stability, resolution, and precision of a conventional Raman spectrometer. *Applied Spectroscopy,* ***60***, 946–950.

Gaufrès, R., Huguet, P., & Arab, Y. (1995) Method for the determination of spectral shifts in Raman spectroscopy. *Journal of Raman Spectroscopy,* ***26*** (3), 243-253.

Giggenbach, W. F. (1988) Geothermal solute equilibria. derivation of Na-K-Mg-Ca geoindicators. *Geochimica et Cosmochimica Acta,* ***52*** (12), 2749-2765.

Giggenbach, W. F. (1996) Chemical composition of volcanic gases. In *Monitoring and mitigation of volcano hazards* (pp. 221-256). Springer Berlin Heidelberg.

Gordon, H.R. & McCubbin, T.K. (1966) The 2.8-micron bands of CO_2. *Journal of Molecular Spectroscocpy*. ***19***, 137–154.

Hartley, M.E., Maclennan, J., Edmonds, M., & Thordarson, T. (2014) Reconstructing the deep CO_2 degassing behavior of large basaltic fissure eruptions. *Earth and Planetary Science Letters*, ***393***, 120-121.

Hedenquist, J.W., & Henley, R.W. (1985) The importance of CO_2 on freezing point measurements of fluid inclusions; evidence from active geothermal systems and implications for epithermal ore deposition. *Economic geology*, **80** (5), 1379-1406.

Hollister, L.S. (1981) Information intrinsically available from fluid inclusions. Short Course in fluid inclusions: applications to petrology. Calgary, Mineralogical Association of Canada, 1-12.

Izraeli, E.S., Harris, J.W. & Navon, O. (1999) Raman barometry of diamond formation. *Earth and Planetary Science Lett*ers, ***173***, 351–360.

Kawakami Y., Yamamoto J. & Kagi H. (2003) Micro-Raman densimeter for the CO_2 inclusions in mantle-derived minerals. *Applied Spectroscopy,* ***57***, 1333–1339.

Kelley, D. S. (1996) Methane-rich fluids in the oceanic crust. *Journal of Geophysical Research: Solid Earth* (1978–2012), ***101*** (B2), 2943-2962.

Kent, A. J. (2008) Melt inclusions in basaltic and related volcanic rocks. *Reviews in Mineralogy and Geochemistry*, ***69*** (1), 273-331.

Lin, F., Bodnar, R.J. & Becker, S.P. (2007) Experimental determination of the Raman CH_4 symmetric stretching (v_1) band position from 1–650 bar and 0.3–22 ºC: Application to fluid inclusion studies. *Geochimica et Cosmochimica Acta,* ***71***,

3746– 3756.
Lu, W., Chou, I. M., Burruss, R. C., & Song, Y. (2007) A unified equation for calculating methane vapor pressures in the $CH_4 – H_2O$ system with measured Raman shifts. *Geochim. Cosmochim. Acta*, ***71*** (16), 3969-3978.
Mestari, A., Gaufrès, R., & Huguet, P. (1997) Behaviour of the calibration of a Raman spectrometer with temperature changes. *Journal of Raman spectroscopy*, ***28*** (10), 785-789.
Métrich, N., & Wallace, P. J. (2008) Volatile abundances in basaltic magmas and their degassing paths tracked by melt inclusions. *Reviews in Mineralogy and Geochemistry*, ***69*** (1), 363-402.
McCreery R. L. (2000) Raman Spectroscopy for Chemical Analysis, *John Wiley & Sons*. 448 pp.
Newman, S., & Lowenstern, J. B. (2002) VolatileCalc: a silicate melt–H_2O–CO_2 solution model written in Visual Basic for Excel. *Computers & Geosciences*, ***28*** (5), 597-604.
Newton, R.C., Smith, J.V., Windley, B.F. (1980) Carbonic metamorphism, granulites and crustal growth. *Nature,* ***288***, 45–50.
Roedder, E,. (1965) Liquid CO_2 inclusions in olivine-bearing nodules and phenocrysts from basalts. *American Mineralogist*, ***50***, 1746–1782.
Roedder, E. (1984) Fluid Inclusions, Mineralogy *Society of America Reviews on Mineralogy,* ***12***, 644 pp.
Roedder, E. (1994) Fluid inclusion evidence of mantle fluids. In B De Vivo, M.L Frezzotti (Eds.), *Fluid inclusions in Minerals: Methods and Applications,* Virginia Polytechnic Institute and State University, Blacksburg, pp. 283–296.
Roedder, E. & Bodnar, R.J. (1997) Fluid inclusion studies of hydrothermal ore deposits. In Geochemistry of Hydrothermal Ore Deposits (ed. H. L. Barnes), third ed. *Wiley & Sons Inc.*, New York, pp. 657–698.
Rosso K. M. & Bodnar R. J. (1995) Detection limits of CO_2 in fluid inclusions using microthermometry and laser Raman spectroscopy and the spectroscopic characterization of CO_2. *Geochimica et Cosmochimica Acta,* ***59***, 3961–3975.
Song, Y., Chou, I.M., Hu, W., Burruss, R. & Lu, W. (2009) CO_2 density-Raman shift relation derived from synthetic inclusions in fused capillaries and its application. *Acta Geolgica Sinica,* ***83***, 932–938.
Span, R. & Wagner, W. (1996) A new equation of state for carbon dioxide covering the fluid region from the triple point temperature to 1100 K at pressures up to 800 MPa. *Journal of Physical Chem*istry, ***25***, 1509–1596.
Steele-MacInnis, M., Esposito, R. & Bodnar, R.J. (2011) Thermodynamic model for the effect of post-entrapment crystallization on the H_2O-CO_2 systematics of vapor-saturated, silicate melt inclusions. *Journal of Petrology*, ***52***, 2461-2482.
Taylor, J. R. (1996) An Introduction To Error Analysis: The Study Of Uncertainties In Physical Measurements. University Science Books, pp. 327.
Touret, J. (1971) Le facies granulite en Norvege Meridionale: II. Les inclusions fluides. *Lithos*, ***4*** (4), 423-436.
Touret, J. (1981) Fluid inclusions in high-grade metamorphic rocks. In Fluid Inclusions: Applications to Petrology, (eds. L. S. Hollister & M. L. Crawford). *Mineralogy Association of Canada, Short Course*, ***6***. pp. 182–208.

Touret, J. (2001) Fluids in metamorphic rocks. *Lithos,* ***55***, 1–25.
Wallace, PJ (2005) Volatiles in subduction zone magmas: concentrations and fluxes based on melt inclusion and volcanic gas data. *Journal of Volcanology and Geothermal Research,* ***140***, 217–240
Wang, X., Chou, I. M., Hu, W., Burruss, R.C., Sun, Q., & Song, Y. (2011) Raman spectroscopic measurements of CO_2 density: Experimental calibration with high-pressure optical cell (HPOC) and fused silica capillary capsule (FSCC) with application to fluid inclusion observations. *Geochimica et Cosmochimica Acta*, ***75*** (14), 4080-4093.
Wright, R.B. & Wang, C.H. (1973) Density effect on the Fermi resonance in gaseous CO_2 Raman scattering. *Journal of Chemical Physics*. ***58***, 2893–2895.
Wright, R.B. & Wang, C.H. (1975) Effect of density on the Raman scattering of molecular fluids. II. Study of intermolecular interactions in CO_2. *Journal of Chemical Physics*. ***61***, 2707–2710.
Yamamoto, J., Kagi, H., Kaneoka, I., Lai, Y., Prikhod'ko, V.S., & Arai, S. (2002) Fossil pressures of fluid inclusions in mantle xenoliths exhibiting rheology of mantle minerals: implications for the geobarometry of mantle minerals using micro-Raman spectroscopy. *Earth and Planetary Science Letters*, ***198*** (3), 511-519.
Yamamoto, J. & Kagi, H. (2006) Extended micro-Raman densimeter for CO_2 applicable to mantle-originated fluid inclusions. *Chemistry Letters,* ***35***, 610–611.
Yamamoto, J., Kagi, H., Kawakami, Y., Hirano, N., & Nakamura, M. (2007) Paleo-Moho depth determined from the pressure of CO_2 fluid inclusions: Raman spectroscopic barometry of mantle-and crust-derived rocks. *Earth and Planetary Science Letters*, ***253*** (3), 369-377.
Yardley, B.W.D. (1997) The evolution of fluids through the metamorphic cycle. In *Fluid flow and transport in rocks. Jamtveit, B., & Yardley, B.W.D.* (Eds.), Springer, pp. 99-121.
Yardley, B. W., & Bodnar, R. J. (2014) Fluids in the continental crust. *Geochemical Perspectives*, ***3*** (1), 1-123.

Tables

Table 1. Equations used to describe the relationship between density, pressure, and splitting of the Fermi diad for CO_2

Source	Equation
Rosso & Bodnar (1995)	$\rho = 2.49\Delta+102.68$
Kawakami et al. (2003)	$\rho = 0.03238697\Delta^3 + 10.08428\Delta^2 -1046.189\Delta + 36163.67$
Yamamoto & Kagi (2006)	$\rho = - 0.01917(\Delta-100)^3 + 0.1984(\Delta-100)^2 - 0.241(\Delta-100) - 0.341$
	$\rho = - 0.00111808(\Delta-100)^8 + 0.04498451(\Delta-100)^7 - 0.7727143(\Delta-100)^6 + 7.4128146(\Delta-100)^5 - 43.468301(\Delta-100)^4 + 159.54433(\Delta-100)^3 - 357.7651(\Delta-100)^2 + 448.2404 (\Delta-100) -240.461$
Song et al. (2009)	$\rho = 0.74203 (-0.019\Delta^3 + 5.90332\Delta^2 - 610.79472\Delta + 21050.30165) - 3.54278$
Fall et al. (2011)	$\rho = - 0.030314551\Delta^3 + 9.432834797\Delta^2 - 977.9384933\Delta + 33780.38242$
Wang et al. (2011)	$\rho = 47513.64243 - 1374.824414\Delta + 13.25586152\Delta^2 - 0.04258891551\Delta^3$
Lamadrid et al. (this study)	$P_{psi} = - 176807.6 + (1723.5547\times \Delta) - 1722.7765 \times (\Delta - 102.866)^2$ $\rho = - 36.42055 + (0.354812 \times \Delta)$

ρ = density (g/cm^3) ; Δ = Fermi diad splitting (cm^{-1}; P_{psi} = Pressure (psi)

Table 2. Experimental conditions reported for the published densimeters.

Source	Experiment method	Pressure (MPa)	Density (g/cm^3)	T (ºC)	Reported error	Raman calibration method	Peak fitting function	EOS
Rosso & Bodnar (1995)	Gas cell SFI	0.5 - 50	0.1 - 1.21	RT	0.02 g/cm^3	Ne light	Gaussian/ Lorentz	Duschek et al. (1990) Bottinga & Richet (1981)
Kawakami et al. (2003)	HPOC	4 - 145	-	16.1 - 18.3 57.4 - 58.4 (SC)	0.1 cm^{-1}	naphtalene	Lorentz	Sterner & Pitzer (1994)
Yamamoto & Kagi (2006)	HPOC	-	0.91 - 1.24		0.03 cm^{-1}	naphtalene	Lorentz	Sterner & Pitzer (1994)
Song et al. (2009)	FSCC	-	0.06 - 1.05	22.1 - 23.5	0.1 cm^{-1}	diamond	Not specified	Span & Wagner (1996)
Fall et al. (2011)	HPOC	1 - 30	-	-10 to 22 35 (SC)	0.035 cm^{-1}	silicon	Gaussian/ Lorentz	Span & Wagner (1996)
Wang et al. (2011)	HPOC FSCC	2.2 - 35.7	0.04	RT 40 (SC)	0.054 cm^{-1}	benzonitrile diamond	Gaussian	Span & Wagner (1996)
Lamadrid et al. (2016)	HPOC	0.06 - 6.1	-	RT	0.0037 g/cm^3 0.01 cm^{-1}	Ne light	Gaussian	Span & Wagner (1996)

SFI: synthetic fluid inclusions, HPOC: high pressure optical cell, FSCC: fused silica capillary capsules, RT: room temperature, SC: supercritical temperatures.

Table 3. Analytical conditions and calculated Fermi diad peak splitting, density and uncertaint
peak splitting.

Pressure (psi)	Pressure (MPa)	Temperature (°C)	Δ_{Real}[1]	Density[2] (g/cm^3)	Error Δ_{Real} (cm^{-1})
9	0.06	23	102.64	0.001	0.007
19	0.13	23	102.65	0.002	0.002
29	0.2	23	102.65	0.004	0.007
39	0.27	22.9	102.65	0.005	0.01
49	0.34	23.1	102.65	0.006	0.014
69	0.48	22.8	102.67	0.009	0.012
79	0.54	23.1	102.67	0.010	0.007
99	0.68	23	102.68	0.013	0.017
109	0.75	23.1	102.67	0.014	0.007
129	0.89	23	102.68	0.017	0.007
144	0.99	23	102.69	0.019	0.005
159	1.1	22.9	102.69	0.021	0.007
174	1.2	23	102.70	0.023	0.003
189	1.3	22.8	102.70	0.025	0.005
204	1.41	23	102.73	0.027	0.017
224	1.54	22.8	102.73	0.030	0.012
239	1.65	23	102.74	0.032	0.005
259	1.79	22.6	102.76	0.035	0.005
269	1.85	23	102.76	0.037	0.02
284	1.96	22.6	102.77	0.039	0.005
299	2.06	23	102.77	0.042	0.002
314	2.16	22.6	102.78	0.044	0.017
329	2.27	23.1	102.80	0.046	0.01
344	2.37	22.6	102.80	0.049	0.007
359	2.48	23.2	102.81	0.051	0.015
374	2.58	22.5	102.81	0.054	0.017
389	2.68	23.2	102.82	0.057	0.007
404	2.79	22.4	102.82	0.059	0.012
409	2.82	23.1	102.83	0.060	0.012
434	2.99	22.4	102.83	0.065	0.017
444	3.06	23.1	102.85	0.067	0.0071
459	3.16	22.3	102.85	0.070	0.005
469	3.23	23.1	102.87	0.071	0.002
489	3.37	22.2	102.86	0.076	0.002
504	3.47	23.1	102.88	0.078	0.01
524	3.61	22.1	102.88	0.083	0.015
534	3.68	23.1	102.89	0.085	0.01

Pressure (psi)	Pressure (MPa)	Temperature (°C)	Δ_{Real}[1]	Density[2] (g/cm^3)	Error Δ_{Real} (cm^{-1})
554	3.82	22.6	102.90	0.090	0.015
564	3.89	23.1	102.91	0.091	0.002
579	3.99	22.5	102.91	0.095	0.012
589	4.06	23.1	102.93	0.087	0
604	4.16	22.5	102.93	0.101	0.014
619	4.27	23.2	102.95	0.104	0.008
634	4.37	22.4	102.95	0.109	0.008
654	4.51	23.1	102.97	0.113	0.007
664	4.58	22.4	102.97	0.117	0.002
684	4.72	23.1	102.99	0.122	0.012
694	4.78	22.3	103.00	0.126	0.005
709	4.89	22.3	103.00	0.129	0.015
729	5.01	22.2	103.03	0.137	0.01
734	5.06	23.3	103.04	0.137	0.017
757	5.22	22.3	103.05	0.147	0
764	5.27	23.3	103.06	0.148	0.005
784	5.41	22.2	103.09	0.158	0.01
794	5.47	23.3	103.10	0.160	0.01
812	5.6	22.3	103.12	0.171	0.007
829	5.72	23.3	103.14	0.176	0.01
842	5.81	22.2	103.17	0.188	0.022
854	5.89	23.3	103.18	0.190	0.012
868	5.98	22.3	103.21	0.206	0.02
879	6.06	23.3	103.23	0.207	0.014

[1]Fermi diad splitting obtained by using Eq. (1).
[2]Densities calculated using Span & Wagner (1996) EOS.

Table 4. Raman instruments and configurations, densimeters, slopes of fitted lines, and fitting statistics.

Experiment	Raman Instrument	Laser (nm)	Gratings	Fitted equation	Residual Error[a] (g/cm^3)	Slope ($g/cm^3/cm^{-1}$)	R^2
Eq. (3) Ne lines	JY Horiba Labram 800	514	1800	$\rho = - 36.42(0.305) + 0.355(0.003)\Delta$	0.002	0.355	0.996
VT 514nm 600g	JY Horiba Labram 800	514	600	$\rho = - 35.679(1.302) + 0.347(0.013)\Delta$	0.004	0.347	0.986
VT 514nm 1800g	JY Horiba Labram 800	514	1800	$\rho = - 36.635(0.293) + 0.357(0.003)\Delta$	0.004	0.357	0.999
VT 514nm 2400g	JY Horiba Labram 800	514	2400	$\rho = - 38.025(0.305) + 0.37(0.003)\Delta$	0.002	0.37	0.999
VT 632nm 600g	JY Horiba Labram 800	632	600	$\rho = - 37.8(2.404) + 0.368(0.023)\Delta$	.005	0.368	0.965
VT 632nm 1800g	JY Horiba Labram 800	632	1800	$\rho = - 35.424(0.86) + 0.345(0.008)\Delta$	0.003	0.345	0.992
VT 632nm 2400g	JY Horiba Labram 800	632	2400	$\rho = - 40.377(0.829) + 0.394(0.008)\Delta$	0.002	0.394	0.995
USGS 532nm 600g	JY Horiba Labram 800	532	600	$\rho = - 37.387(1.027) + 0.364(0.01)\Delta$	0.005	0.364	0.988
USGS532nm 1800g	JY Horiba Labram 800	532	1800	$\rho = - 37.37(0.224) + 0.364(0.002)\Delta$	0.001	0.364	0.999
XplorA 532nm 1800g	XploRA Plus	532.	1800	$\rho = - 38.891(0.874) + 0.379(0.008)\Delta$	0.002	0.379	0.994
XplorA 532nm 2400g	XploRA Plus	532	2400	$\rho = - 39.737(0.671) + 0.387(0.068)\Delta$	0.003	0.387	0.996
XplorA785nm 1800g	XploRA Plus	785	1800	$\rho = - 38.016(0.694) + 0.37(0.007)\Delta$	0.002	0.37	0.996
Kawakami et al. (2003)*	Chromex 250is	514	-	$\rho = -35.25(2.916) + 0.344(0.028)\Delta$	0.007	0.344	0.954
Song et al. (2009)	JY Horiba Labram 800	532	1800	$\rho = -39.548+ 0.385\Delta$	-	0.385	1[+]
Wang et al. (2011)*	JY Horiba Labram 800	532	1800	$\rho = -35.652(0.578) + 0.347(0.006)\Delta$	0.004	0.347	0.991
Fall et al. (2011)*	JY Horiba Labram 800	514	1800	$\rho = -39.441(0.164) + 0.384(0.002)\Delta$	0.001	0.384	0.999

nm = laser wavelength, σ = density, Δ = Fermi diad splitting (cm^{-1}) [a]Error = standard deviation of the residuals (difference from the predicted density equation to the real data),*only data lower than 0.2 g/cm^3, [+]only 2 data points

Table 5. Uncertainties in density (g/cm^3) as a function of difference in splitting of the Fermi diad for the standard and unknown ($\Delta\nu = \Delta_{Std} - \Delta_{Ukn}$).

Δν	σρmax	σρmin	Δν	σρmax	σρmin
-0.7	-0.0191	0.0155	-0.35	-0.0095	0.0077
-0.69	-0.0188	0.0153	-0.34	-0.0093	0.0075
-0.68	-0.0185	0.0150	-0.33	-0.0090	0.0073
-0.67	-0.0182	0.0148	-0.32	-0.0087	0.0071
-0.66	-0.0180	0.0146	-0.31	-0.0084	0.0069
-0.65	-0.0177	0.0144	-0.3	-0.0082	0.0066
-0.64	-0.0174	0.0142	-0.29	-0.0079	0.0064
-0.63	-0.0172	0.0139	-0.28	-0.0076	0.0062
-0.62	-0.0169	0.0137	-0.27	-0.0074	0.0060
-0.61	-0.0166	0.0135	-0.26	-0.0071	0.0058
-0.6	-0.0163	0.0133	-0.25	-0.0068	0.0055
-0.59	-0.0161	0.0131	-0.24	-0.0065	0.0053
-0.58	-0.0158	0.0128	-0.23	-0.0063	0.0051
-0.57	-0.0155	0.0126	-0.22	-0.0060	0.0049
-0.56	-0.0153	0.0124	-0.21	-0.0057	0.0046
-0.55	-0.0150	0.0122	-0.2	-0.0054	0.0044
-0.54	-0.0147	0.0119	-0.19	-0.0052	0.0042
-0.53	-0.0144	0.0117	-0.18	-0.0049	0.0040
-0.52	-0.0142	0.0115	-0.17	-0.0046	0.0038
-0.51	-0.0139	0.0113	-0.16	-0.0044	0.0035
-0.5	-0.0136	0.0111	-0.15	-0.0041	0.0033
-0.49	-0.0133	0.0108	-0.14	-0.0038	0.0031
-0.48	-0.0131	0.0106	-0.13	-0.0035	0.0029
-0.47	-0.0128	0.0104	-0.12	-0.0033	0.0027
-0.46	-0.0125	0.0102	-0.11	-0.0030	0.0024
-0.45	-0.0123	0.0100	-0.1	-0.0027	0.0022
-0.44	-0.0120	0.0097	-0.09	-0.0025	0.0020
-0.43	-0.0117	0.0095	-0.08	-0.0022	0.0018
-0.42	-0.0114	0.0093	-0.07	-0.0019	0.0015
-0.41	-0.0112	0.0091	-0.06	-0.0016	0.0013
-0.4	-0.0109	0.0089	-0.05	-0.0014	0.0011
-0.39	-0.0106	0.0086	-0.04	-0.0011	0.0009
-0.38	-0.0103	0.0084	-0.03	-0.0008	0.0007
-0.37	-0.0101	0.0082	-0.02	-0.0005	0.0004
-0.36	-0.0098	0.0080	-0.01	-0.0003	0.0002

Table 5. Continuation.

Δν	σρmax	σρmin	Δν	σρmax	σρmin
0	0.0000	0.0000	0.36	0.0098	-0.0080
0.01	0.0003	-0.0002	0.37	0.0101	-0.0082
0.02	0.0005	-0.0004	0.38	0.0103	-0.0084
0.03	0.0008	-0.0007	0.39	0.0106	-0.0086
0.04	0.0011	-0.0009	0.4	0.0109	-0.0089
0.05	0.0014	-0.0011	0.41	0.0112	-0.0091
0.06	0.0016	-0.0013	0.42	0.0114	-0.0093
0.07	0.0019	-0.0015	0.43	0.0117	-0.0095
0.08	0.0022	-0.0018	0.44	0.0120	-0.0097
0.09	0.0025	-0.0020	0.45	0.0123	-0.0100
0.1	0.0027	-0.0022	0.46	0.0125	-0.0102
0.11	0.0030	-0.0024	0.47	0.0128	-0.0104
0.12	0.0033	-0.0027	0.48	0.0131	-0.0106
0.13	0.0035	-0.0029	0.49	0.0133	-0.0108
0.14	0.0038	-0.0031	0.5	0.0136	-0.0111
0.15	0.0041	-0.0033	0.51	0.0139	-0.0113
0.16	0.0044	-0.0035	0.52	0.0142	-0.0115
0.17	0.0046	-0.0038	0.53	0.0144	-0.0117
0.18	0.0049	-0.0040	0.54	0.0147	-0.0119
0.19	0.0052	-0.0042	0.55	0.0150	-0.0122
0.2	0.0054	-0.0044	0.56	0.0153	-0.0124
0.21	0.0057	-0.0046	0.57	0.0155	-0.0126
0.22	0.0060	-0.0049	0.58	0.0158	-0.0128
0.23	0.0063	-0.0051	0.59	0.0161	-0.0131
0.24	0.0065	-0.0053	0.6	0.0163	-0.0133
0.25	0.0068	-0.0055	0.61	0.0166	-0.0135
0.26	0.0071	-0.0058	0.62	0.0169	-0.0137
0.27	0.0074	-0.0060	0.63	0.0172	-0.0139
0.28	0.0076	-0.0062	0.64	0.0174	-0.0142
0.29	0.0079	-0.0064	0.65	0.0177	-0.0144
0.3	0.0082	-0.0066	0.66	0.0180	-0.0146
0.31	0.0084	-0.0069	0.67	0.0182	-0.0148
0.32	0.0087	-0.0071	0.68	0.0185	-0.0150
0.33	0.0090	-0.0073	0.69	0.0188	-0.0153
0.34	0.0093	-0.0075	0.7	0.0191	-0.0155
0.35	0.0095	-0.0077			

Δν = difference between the observed splitting of the Fermi diad of the standard and that of the unknown, $\sigma\rho_{max}$ = density error corresponding to the maximum densimeter slope (m_{max}) at Δν, $\sigma\rho_{min}$ = density error corresponding to the minimum densimeter slope (m_{min}) at Δν.

Table 6. Density of carbon dioxide (g/cm^3) for various measured Fermi diad splittings (Δ) calculated using the Universal Densimeter at (22˚C).

	0.00	**0.01**	**0.02**	**0.03**	**0.04**	**0.05**	**0.06**	**0.07**	**0.08**	**0.09**
102.6x	–	–	–	–	–	0.0003	0.004	0.008	0.011	0.015
102.7x	0.019	0.022	0.026	0.030	0.033	0.037	0.041	0.044	0.048	0.052
102.8x	0.055	0.059	0.063	0.066	0.070	0.074	0.077	0.081	0.085	0.088
102.9x	0.092	0.096	0.099	0.103	0.107	0.110	0.114	0.118	0.121	0.125
103.0x	0.129	0.132	0.136	0.140	0.143	0.147	0.150	0.154	0.158	0.161
103.1x	0.165	0.169	0.172	0.176	0.180	0.183	0.187	0.191	0.194	0.198
103.2x	0.202	0.205	0.209	L + V	L + V	L + V	L + V	L + V	L + V	L + V

Figures

Figure 1

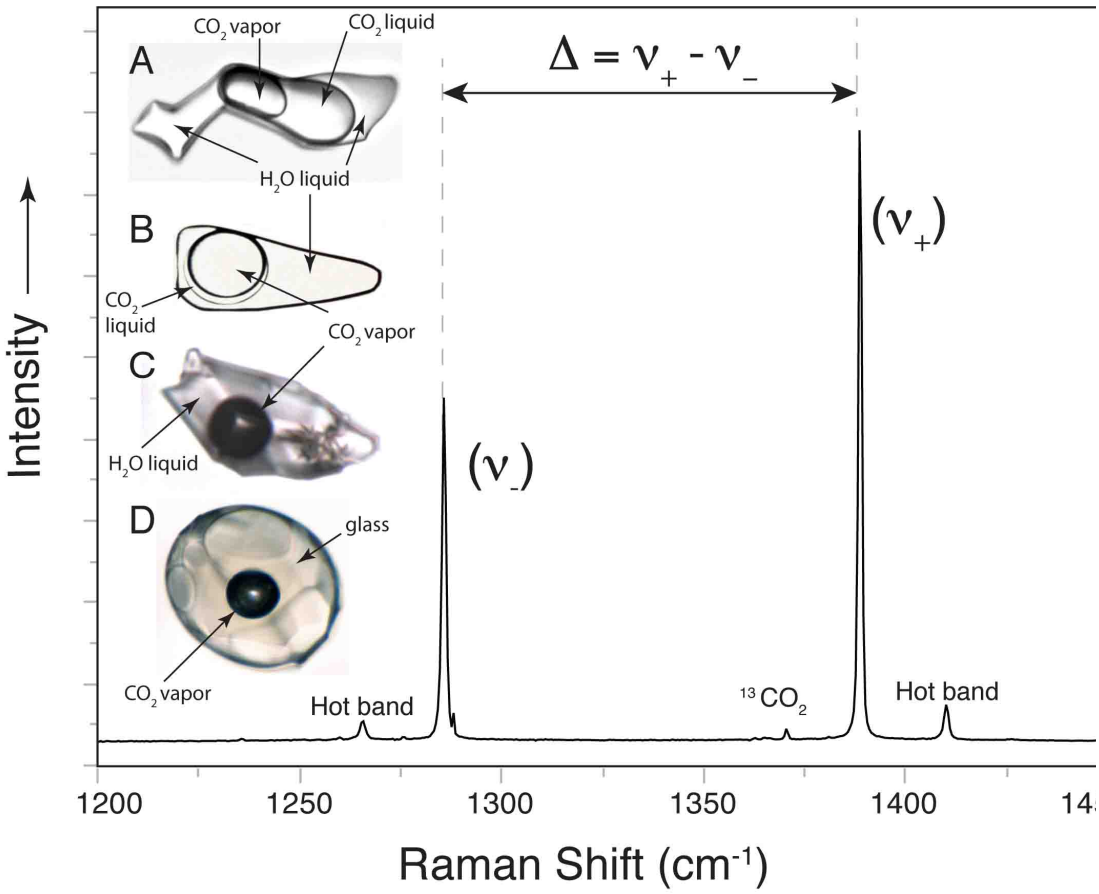

Figure 1. Raman spectrum of CO_2 showing the Fermi diad and representative CO_2-bearing fluid and melt inclusions. The distance between the positions of the υ_+ and the peaks of the Fermi diad is given by Δ (cm^{-1}) and is density (pressure) dependent. The lo intensity hot bands shown are due to the thermal energy of the vibrating molecules and are not used in this study. (A) Three phase fluid inclusion containing liquid H_2O, and liquid and vapor CO_2. (B) Three phase fluid inclusion containing liquid H_2O, CO_2 vapo and a thin rim of liquid CO_2 surrounding the vapor bubble. (C) Fluid inclusion containi liquid H_2O and CO_2 vapor. (D) Melt inclusion containing glass and a CO_2 vapor bubble All photos (A-D) taken at room temperature.

Figure 2

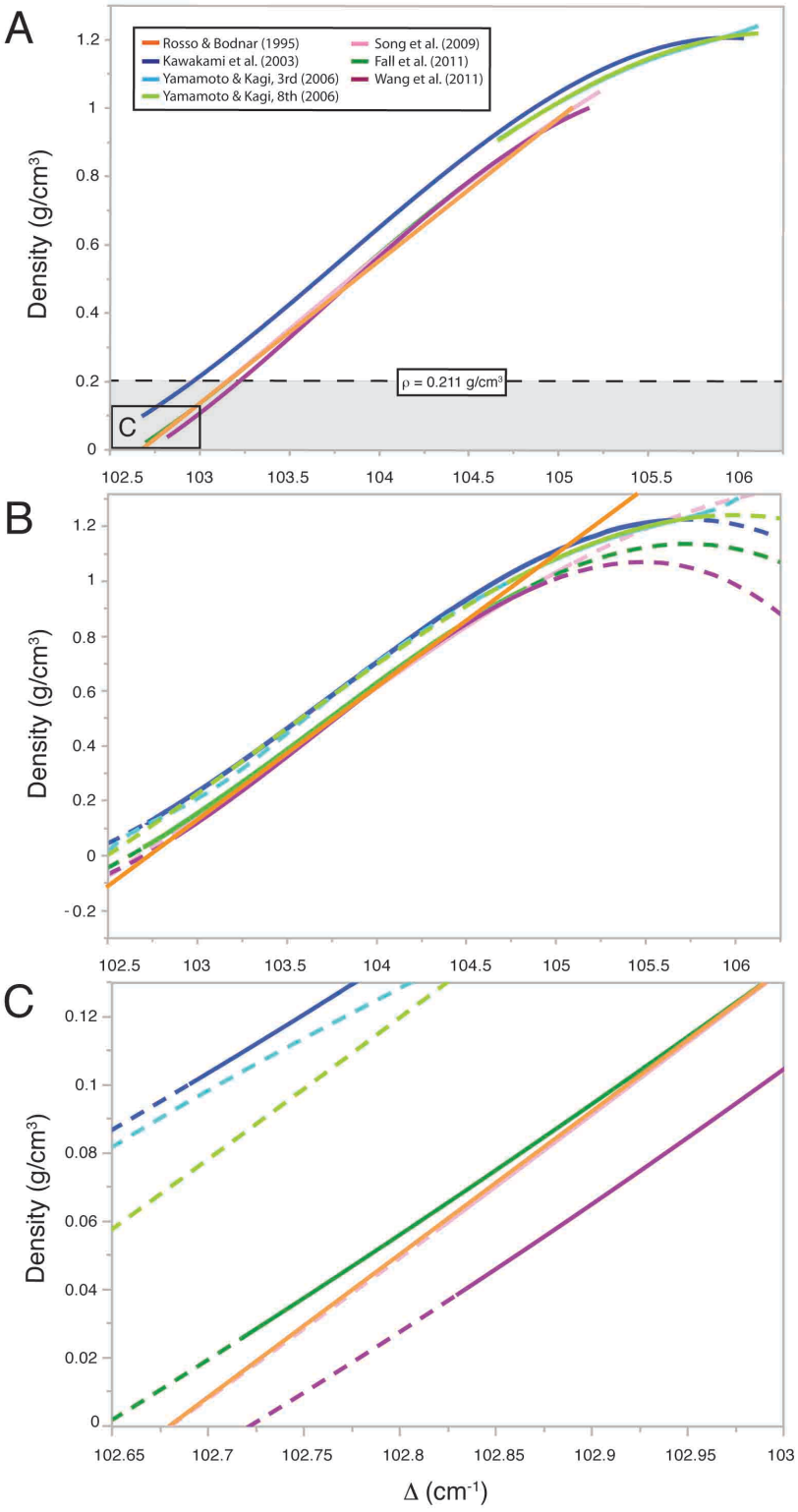
A
B
C
Rosso & Bodnar (1995)
Kawakami et al. (2003)
Yamamoto & Kagi, 3rd (2006)
Yamamoto & Kagi, 8th (2006)
Song et al. (2009)
Fall et al. (2011)
Wang et al. (2011)
ρ = 0.211 g/cm³
Density (g/cm³)
Δ (cm⁻¹)

Figure 2. Density of CO_2 as a function of the Fermi diad splitting predicted by various densimeters. (A) Density of CO_2 as a function of the Fermi diad splitting over the entire density range for which various densimeters have been calibrated. Densities less than 0.211 g/cm^3 correspond to CO_2 vapor at ambient conditions (~22°C) and are shown by the shaded region. (B) Densities predicted by the various published densimeters both within the density region in which calibration measurements were made (solid lines) and extrapolated to higher and/or lower densities using the published densimeter equations. (C) Enlargement of the low-density region shown in Figure 2A. Tables 1 and 2 list the equations and the experimental conditions of the published densimeters, respectively.

Figure 3

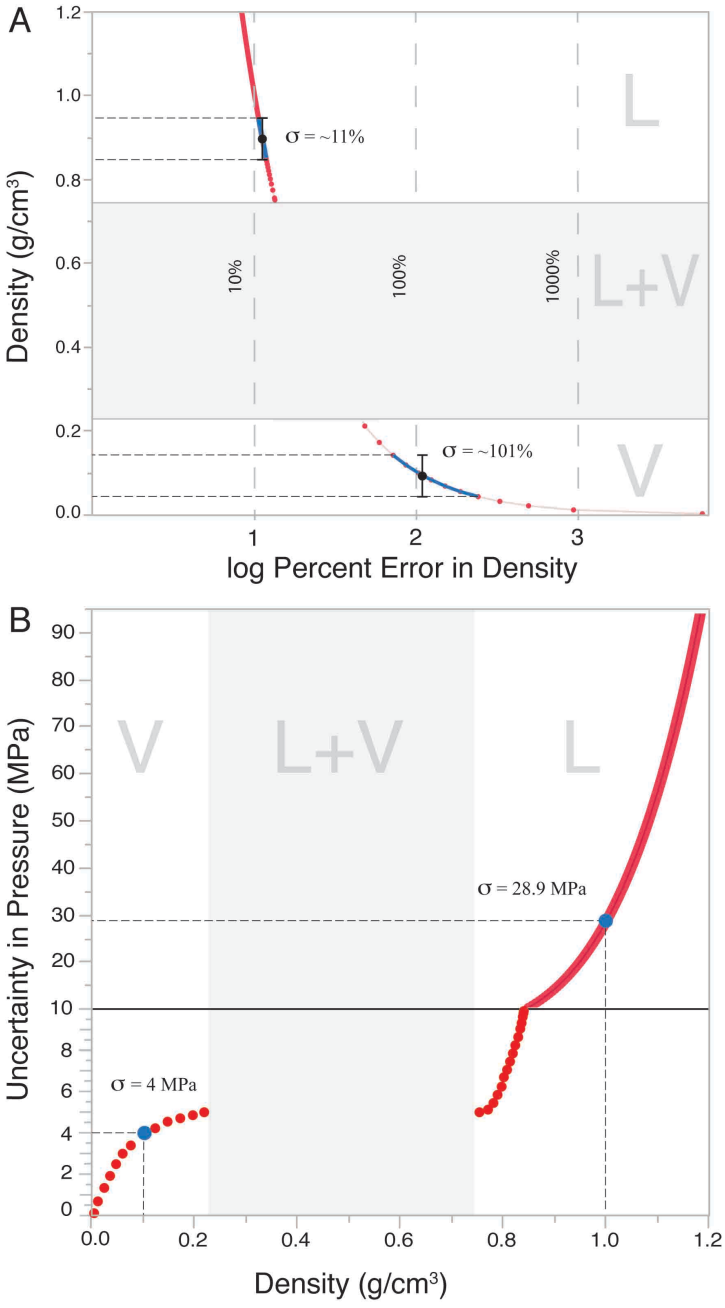
A
Density (g/cm³)
1.2
1.0
0.8
0.6
0.4
0.2
0.0
σ = ~11%
σ = ~101%
L
L+V
V
10%
100%
1000%
1
2
3
log Percent Error in Density
B
Uncertainty in Pressure (MPa)
90
80
70
60
50
40
30
20
10
8
6
4
2
0
V
L+V
L
σ = 28.9 MPa
σ = 4 MPa
0.0
0.2
0.4
0.6
0.8
1.0
1.2
Density (g/cm³)

Figure 3. Comparison of the relative error in density corresponding to an absolute uncertainty in density of ±0.05 g/cm^3, and the pressure uncertainty associated with a ±0.05 g/cm^3 variation in density. (A) The relative error is density, shown as the log of the percent error (x-axis) as a function of density. An uncertainty of ±0.05 g/cm^3 at a density of 0.9 g/cm^3 represents a relative error, σ, of ~11%. The same uncertainty of ±0.05g/cm^3 at a density of 0.1 g/cm^3 represents relative error of ~101%. The percent error increases logarithmically with decreasing density. (B) Uncertainty (or range) in pressure (MPa) required to produce an uncertainty of ±0.05 g/cm^3 in density. The pressure uncertaintyrequired to produce an uncertainty of ±0.05 g/cm^3 in density for a density of 1.0 g/cm^3 is 28.9 MPa, and for a density of 0.1 g/cm^3 the pressure uncertainty is 4 MPa bars. For comparison the uncertainty in pressure determination in this study is ~0.03 MPa (or ~4 psi).

Figure 4

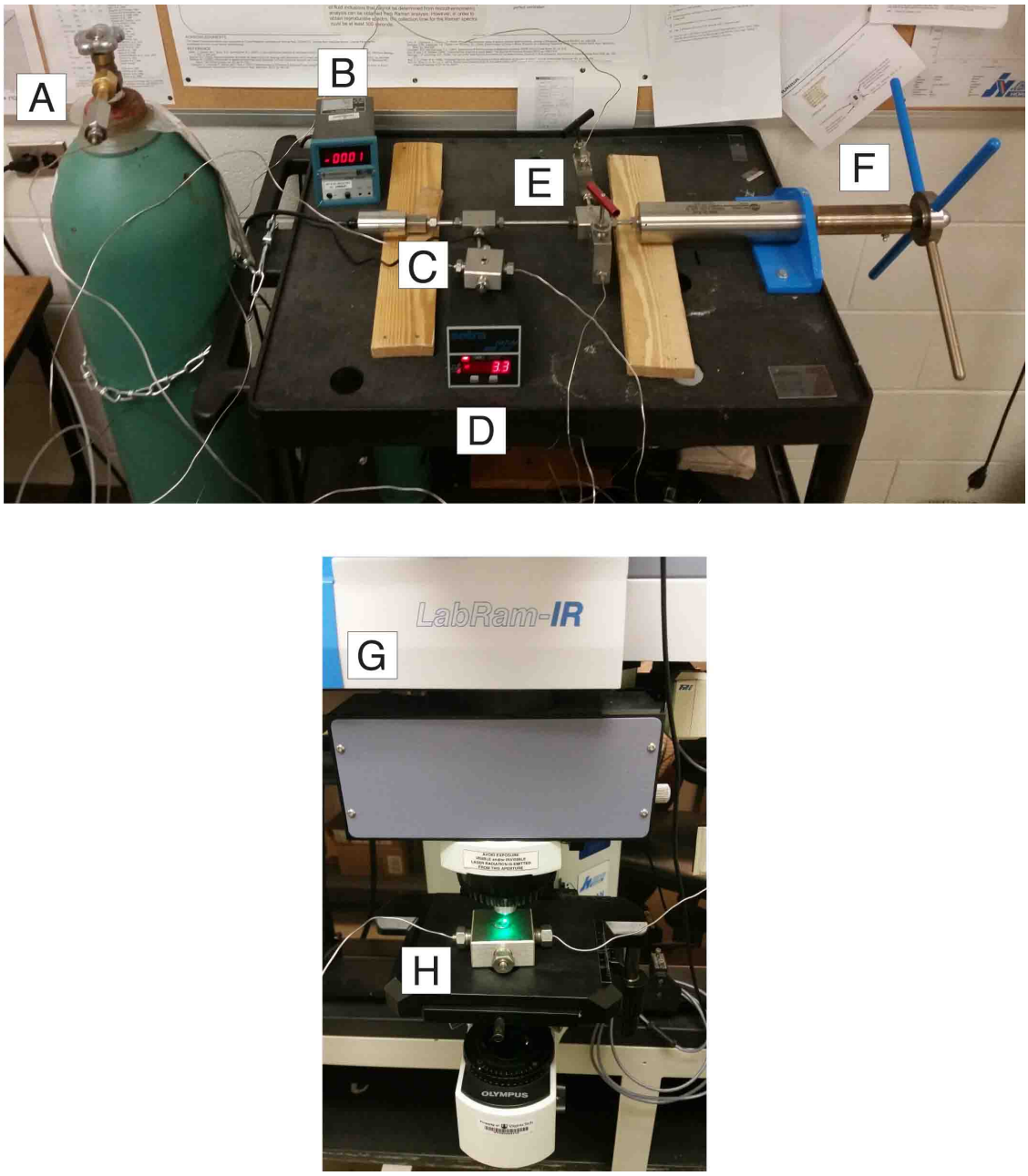

Figure 4. The high-pressure optical cell (HPOC) used to determine the position of the Raman Fermi diad as a function of temperature and pressure. (A) CO_2 tank (99.99% pure). (B) Pressure transducer with digital output in bars. (C) Optical pressure cell. (D) Pressure transducer with digital output in psi. (E) Input and output valves. (F) Manual screw press-type pressure generator. (G) Optical microscope of the JY Horiba LabRam HR spectrometer. (H) Optical pressure cell during Raman analysis. Readers are referred to Lin et al. (2007) and Fall et al. (2011) for a more detailed description of the experimental setup.

Figure 5

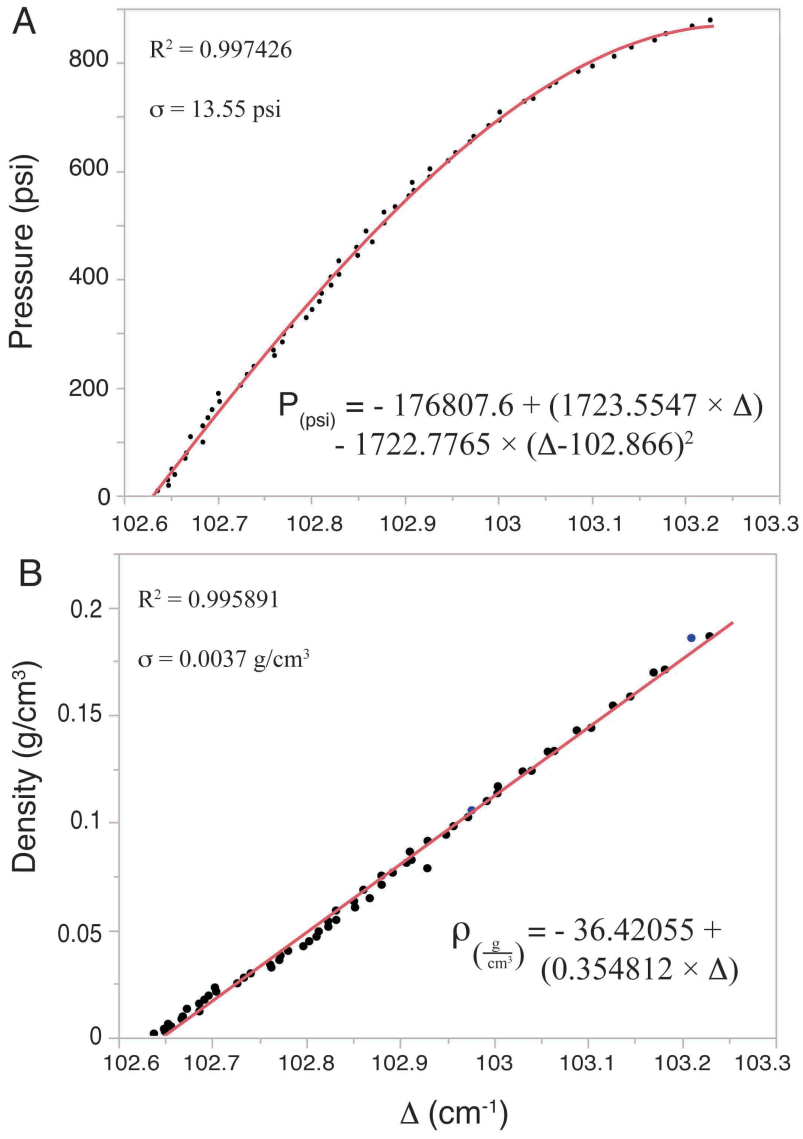

Figure 5. Pressure (A) and density (B) of CO_2 as a function of the splitting of the Fermi diad (distance between the υ_+ and the υ_- peaks of the Fermi diad) for CO_2 measured with the HPOC in this study. Data are listed as Electronic Appendix A.

Figure 6

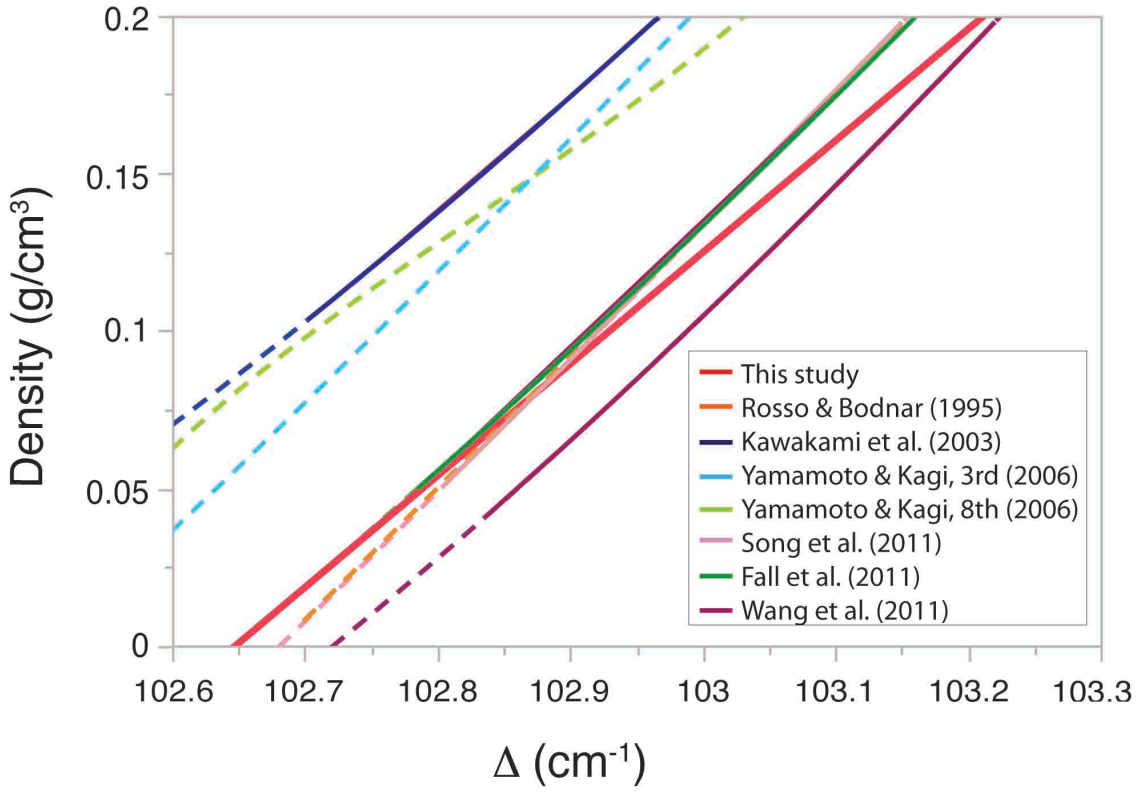

Figure 6. Comparison of published CO_2 densimeters with the densimeter developed in this study. Note that all of the densimeters have been extrapolated by various amounts beyond the range in which they were calibrated, as shown by the dashed lines. The densimeter developed in this study was calibrated over the density range from 0.001 g/cm^3 to 0.211 g/cm^3, corresponding to a pressure range from 0.06 to 6.0 MPa. Data are listed in Table 3.

Figure 7

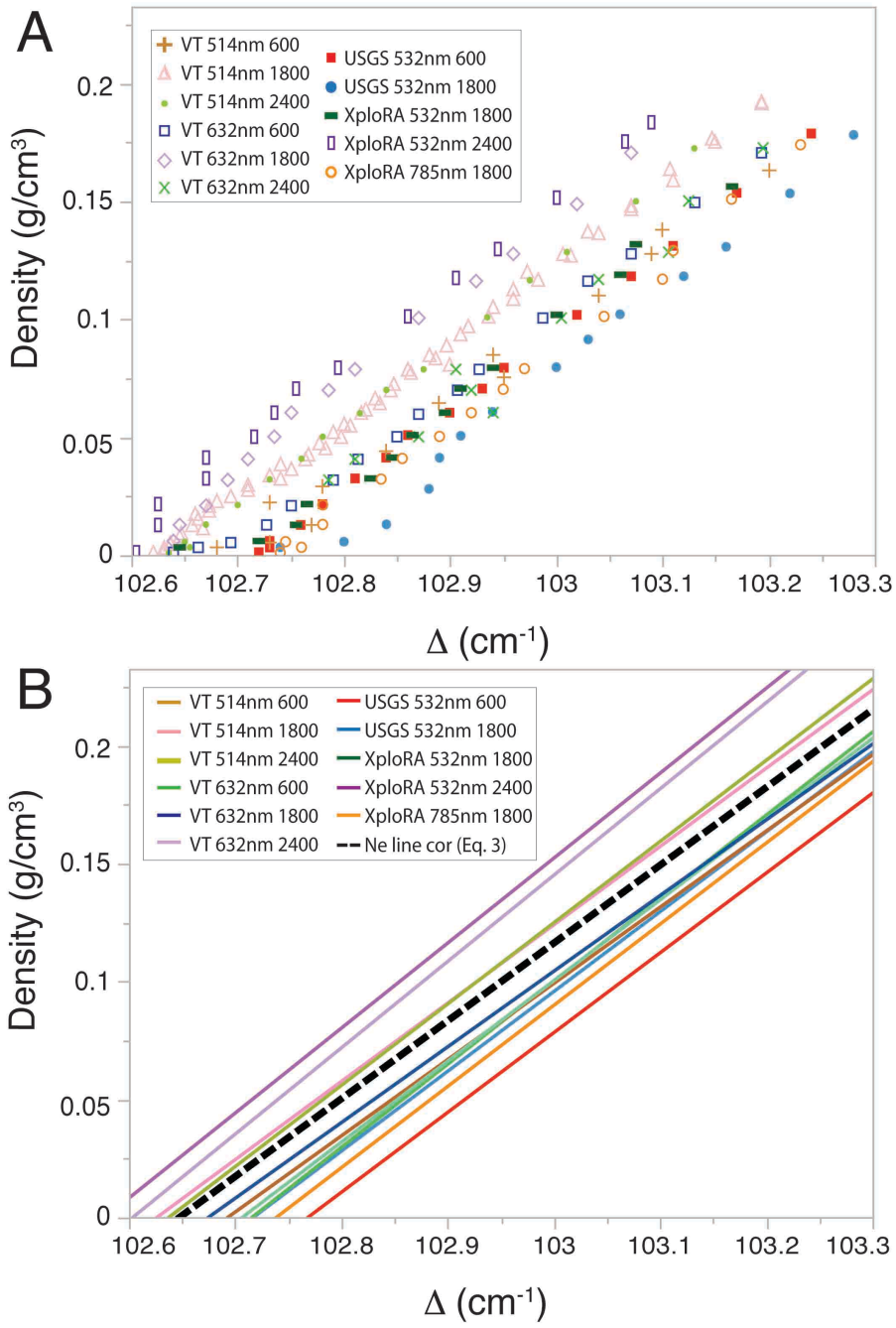

Figure 7. Comparison of the different CO_2 densimeters developed in this study. (A) Data for the splitting of the Fermi diad, Δ, as a function of density for the different Raman analytical configurations. VT refers to analyses conducted at Virginia Tech using the JY Horiba LabRam HR system; USGS refers to analyses conducted at the U. S. Geological Survey using a JY Horiba LabRam HR system; XploRA refers to analyses conducted at Virginia Tech using a JY Horiba XploRA Raman system; 514nm, 632nm, 532nm and

785nm refer to the laser excitation wavelength, and 600, 1800, and 2400 refer to the number of grooves/mm of the grating used. The data set labeled VT 514nm 1800 represents measurements without the Ne line correction. (B) Fitted lines corresponding to the different data sets shown in Figure 7A. The dashed line is the relationship between Fermi diad peak splitting and density predicted by Eq. (3), that was developed using the data in Figure 7A labeled "VT 514nm 1800" after correcting the peak positions using the positions of the bracketing Ne lines collected simultaneously with the CO_2 spectrum.

Figure 8

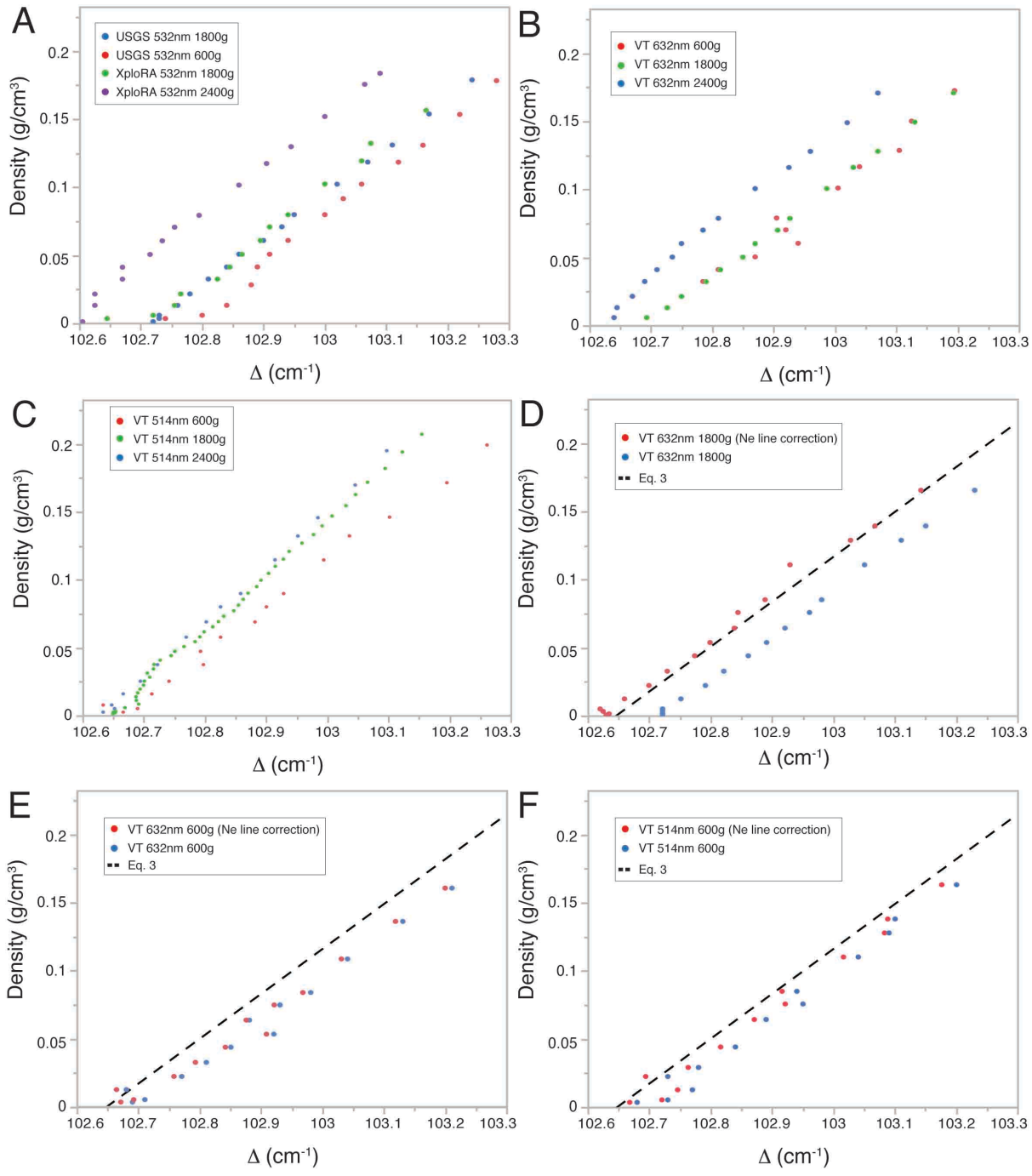

Figure 8. Density of CO_2 as a function of the Fermi diad splitting (Δ) for various instrumental configurations. (A) CO_2 density as a function of the Fermi diad splitting (Δ), all measured using the 532 nm laser but with different gratings. (B) CO_2 density as a function of the Fermi diad splitting (Δ), all measured using the 632 nm laser but different gratings. (C) CO_2 density as a function of the Fermi diad splitting (Δ), all measured using the 514 nm laser but different gratings. In all three cases, the splitting of the Fermi diad for a given density decreases as the resolution of the gratings (more grooves/mm)

increases. The data collected with the 600 grooves/mm gratings show greater dispersion due to the lower spectral resolution. (D-F) Fermi diad splitting as a function of density for different laser and gratings combinations, comparing the data before and after correction using the positions of the simultaneously collected Ne lines. Also shown is relationship between Fermi diad splitting and density predicted by Eq (3) (dashed line).

Figure 9

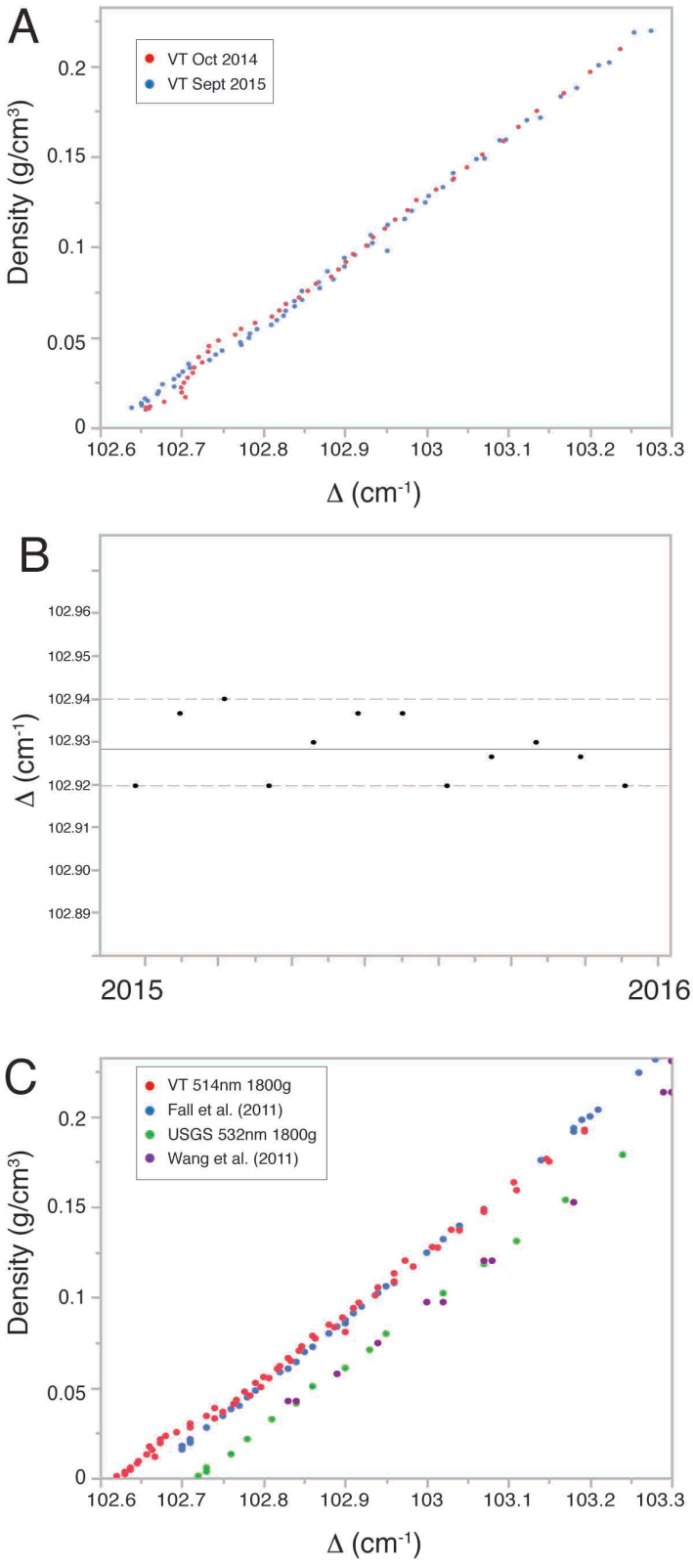
A
VT Oct 2014
VT Sept 2015
Density (g/cm³)
0.2
0.15
0.1
0.05
0
102.6
102.7
102.8
102.9
103
103.1
103.2
103.3
Δ (cm⁻¹)
B
Δ (cm⁻¹)
102.96
102.95
102.94
102.93
102.92
102.91
102.90
102.89
2015
2016
C
VT 514nm 1800g
Fall et al. (2011)
USGS 532nm 1800g
Wang et al. (2011)
Density (g/cm³)
0.2
0.15
0.1
0.05
0
102.6
102.7
102.8
102.9
103
103.1
103.2
103.3
Δ (cm⁻¹)

Figure 9. Comparison of the relationship between Fermi diad peak splitting and density determined at different times. (A) Relationship between Fermi diad splitting (Δ) and density determined in October 2014 and in September 2015 using the 514 nm laser and 1800 groove/mm gratings at Virginia Tech. (B) Measurement of the splitting of the Fermi diad of CO_2 in the HPOC at 500 psi and room temperature at various times over the course of ~ 1 year. (C) Comparison of the relationship between splitting of the Fermi diad and density obtained in this study (VT 514nm 1800g) and data collected at other times using the same Raman configuration, laser wavelength and grating resolution. The data collected in this study and data from Fall et al. (2011) collected approximately 4 years earlier in the same lab using the same Raman system are nearly identical. Similarly, data collected in the USGS lab in this study correlates well with data previously collected by Wang et al. (2011) using the same instrument.

Figure 10

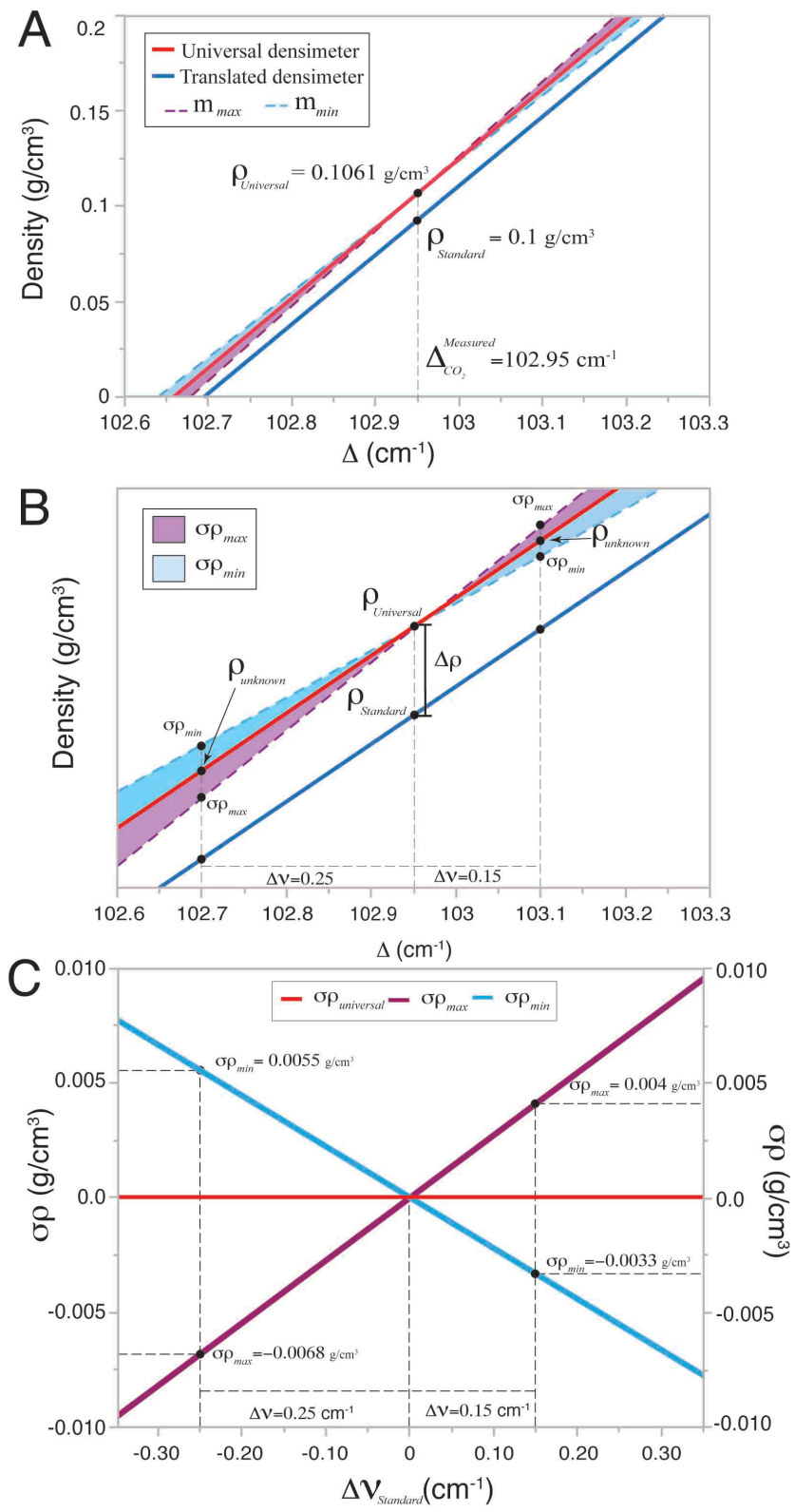
A
Universal densimeter
Translated densimeter
m max
m min
ρ Universal = 0.1061 g/cm³
ρ Standard = 0.1 g/cm³
Δ Measured CO2 =102.95 cm-1
Density (g/cm³)
Δ (cm-1)
B
σρ max
σρ min
ρ unknown
ρ Universal
ρ Standard
Δρ
Δν=0.25
Δν=0.15
Density (g/cm³)
Δ (cm-1)
C
σρ universal
σρ max
σρ min
σρ min= 0.0055 g/cm³
σρ max= 0.004 g/cm³
σρ min=−0.0033 g/cm³
σρ max=−0.0068 g/cm³
Δν=0.25 cm-1
Δν=0.15 cm-1
σρ (g/cm³)
Δν Standard(cm-1)

Figure 10. Methodology for calibration of a Raman densimeter using a single sample of known CO_2 density. See text for detailed explanation of application of the methodology. Table 5 has the data for which Figure 10C was constructed.

Chapter IV

Serpentinization reaction rates measured in olivine micro-batch reactors

Lamadrid H.M., Rimstidt J.D. and Bodnar. R.J.

Abstract

We used synthetic fluid inclusions as mini-reactors in olivine to monitor the serpentinization reactions with different initial fluids compositions (H_2O-NaCl, H2O-$MgCl_2$ and H_2O-NaCl-$MgCl_2$) and salinities (1, 3.5, 6 and 10 wt.%) at ~280ºC. Raman, SEM and TEM analyses confirmed that after a few days at ~280ºC brucite, serpentine and magnetite (only in the experiments that lasted longer than 120 days) formed inside the mini-reactors. Once the crystals started forming the salinity of the fluid inclusions increases constantly. Salinity changes were monitored by changes in the FPD and the amounts of H2O consumed by the serpentinization reaction were used to monitor reaction progress. The olivine micro-reactors experiments revealed that the serpentinization rates are strongly sensitive to the salinity and composition of the reacting fluid and decrease rapidly with increasing salinity. The calculated average rates for salinities of 1 wt.% and 3.5 wt.% are 6.73 x 10^{-9} (moles/m^2sec) and 2.91x 10^{-9} (moles/m^2sec), respectively, whereas for the 6 and 10 wt.% 8.39 x 10^{-10} (moles/m^2sec) and 7.12 x 10^{-11} (moles/m^2sec). In the experiments with high concentrations of Mg in the initial fluid, no reaction was observed in the first 120 days and only after 270 days a few inclusions started to form serpentine and brucite crystals with no salinity changes.

1. Introduction

Serpentinization encompasses a series of hydration reactions that occur when ultramafic rocks are exposed to aqueous fluids circulation. The fluid interacts with olivine and pyroxene to form serpentine phases (lizardite and/or chrysotile) ± brucite ± talc ± magnetite, among other minerals (e.g. Moody, 1976; Wicks & Whittacker, 1977; Wicks & O'Hanley, 1988; Cannat et al., 1992; Cannat, 1993; O'Hanley & Wicks, 1995; Kelley et al., 2001; Bach et al., 2004, 2006; Klein et al., 2009a). Olivine hydration is one of the most important of these reactions and proceeds according to the following simplified reaction:

$$2Mg_2SiO_4 + 3H_2O \Leftrightarrow Mg_3Si_2O_5(OH)_4 + Mg(OH)_2 \quad (1)$$

olivine + water ⇔ serpentine + brucite

The serpentinization process has been known since at least the 1800s (Merrill, 1899; Bowen & Tuttle, 1949; Whittaker & Zussman, 1956; Wenner & Taylor, 1971; Moody, 1976, Wicks & Whittaker, 1977; Wicks and O'Hanley, 1988; O'Hanley, 1992; O'Hanley and Wicks, 1995; O'Hanley, 1996). However, since the implementation of ocean dredging and drilling in slow-spreading Mid-Oceanic Ridge (MOR) environments (Cannat et al., 1992; Kelley et al., 2001; Bach et al., 2002; Dick et al., 2003) over four decades ago, the scientific community has recognized that serpentinization is a much more widespread process than previously thought. Recent estimates suggest that 10 to 25% of uplifted seafloor that formed along slow- or ultra-slow spreading MOR may be composed of serpentinized peridotites (e.g. Carlson, 2001; Cannat *et al.*, 2010; Alt *et al.*, 2013).

Serpentinization has important implications concerning the evolution of the oceanic lithosphere and affects many subduction related processes (Bach et al., 2002, 2004; Dick et al., 2003; Seyler et al., 2003; Boschi et al., 2013; Alt et al., 2013). The hydration reactions that occur in the oceanic lithosphere represent one of the major mass exchange mechanisms between the mantle and the Earths crust, occurring first at ridges (German et al., 2004; Wilcock et al., 2004) and then at subduction zones through recycling and dehydration processes (Deschamps et al, 2011; Li and Lee, 2006). Specifically, serpentinization results in a significant volume increase (up to 40%, O'Hanley, 1992; Evans et al., 2013), alters the rheological and seismic behavior of rocks (Hilairet et al., 2007; Chernak and Hirth, 2010), changes the magnetic properties of the oceanic lithosphere through the precipitation of magnetite (Toft et al., 1990), controls the geochemical cycling of H_2O, C, S and fluid-mobile elements in the solid Earth (Früh-Green et al., 2004; Boschi et al., 2008; Schwarzenbach et al., 2012, 2013a,b; Alt et al., 2013), is one of the major processes that transfer water from the exosphere to the geosphere (Bodnar et al., 2013), and generates a chemical environment similar to that in which life on Earth is thought to have originated (McCollom, 1999; Schulte et al., 2006; Martin & Russell, 2007; Martin et al., 2008; Russell et al., 2010).

Serpentinites occur throughout the geologic record and they outcrop on all continents within suture zones and accreted terrains (Deschamps et al., 2013). Modern-day serpentinization is occurring where upper mantle is exposed at slow to ultra slow spreading ridges (e.g. in oceanic core complexes, Kelley et al., 2001; Boschi et al., 2006; Blackman et al., 2009), in obducted ophiolites and mantle rocks exposed on the continents (Coleman, 1967; Barnes et al., 1967; Barnes & O'Neil, 1978; Kelemen &

Matter, 2008; Schwarzenbach, 2011), in subducting slabs (Deschamps et al., 2011; 2013), and in the mantle wedge where the fluids produced by dehydration of the slab percolate upwards (Hattori & Guilliot, 2003; Hyndman & Peacock, 2003) (Fig. 2).

The geochemical environment associated with serpentinization is one of the most reduced in the near-surface on Earth. The highly reducing conditions are generated as part of the overall serpentinization reaction when, for instance, the Fe- rich brucite reacts with silica in solution to form serpentine and magnetite and produce H_2 by the reaction:

$$Fe(OH)_2 + SiO_{2(aq)} \Leftrightarrow Fe_3Si_2(OH)_4 + Fe_3O_4 + H_2 \quad (2)$$

brucite + "fluid" $\Leftrightarrow$ serpentine + magnetite + hydrogen

Simultaneously, the presence of H_2 can promote the abiogenic reduction of CO_2 to form CH_4 and higher hydrocarbons (Charlou et al., 1998; Proskurowski et al., 2008; McCollom & Seewald, 2001). The presence of H_2 and CH_4 in fluids in modern peridotite-hosted sea-floor systems provides an ideal environment for modern chemosynthetic microorganisms to thrive (Sleep et al., 2004; Martin & Russell, 2007; Schulte et al., 2006; Russell et al., 2010). The microbial communities found in these submarine environments are thought to be analogous to those of the early Earth, while the abiotic production of hydrocarbon chains has been related to stabilization of amino acids that are the building blocks of life on Earth and, likely, other planetary bodies (Schulte et al., 2006; McCollom & Seawald, 2013).

The complex and dynamic serpentinization process involves rocks of different compositions (peridotites, dunites, gabbro, basalts, etc.) interacting with evolving hydrothermal fluid compositions over a range of temperatures (Kelley et al., 2001, 2005; Charlou et al., 2002; Fruh-Green et al., 2003; Allen & Seyfried et al., 2004b; Martin et

al., 2008; Lang et al., 2010, 2012). Despite much work on serpentinization in natural systems, certain aspects of serpentinization reactions, such as the order, timing, direction and products of the reactions, are still a matter of considerable debate (Martin & Fyfe, 1970; Wegner and Ernst, 1983; Moody, 1976; Frost & Beard, 2007; Evans, 2008; McCollom & Bach, 2006; Okamoto et al., 2011; Malvoisin et al., 2012; Ogasawara et al, 2013; Klein et al, 2013; Schwarzenbach et al., 2016; McCollom et al., 2016).

Most of the early experimental studies of serpentinization focused on mineral stability and reactions in the MgO-SiO-H_2O system (Bowen and Tutle, 1949; Kitahara & Kennedy, 1967; Johannes, 1968; Poty et al., 1972; Chernosky, 1973; Evans et al., 1976; Moody, 1976). With the rise in interest in seafloor hydrothermal processes, seafloor spreading and the formation of oceanic core complexes, experimental work using natural samples was conducted to determine reaction pathways, and the effects of temperature and host composition on the compositions of the reaction products and fluids (Martin & Fyfe, 1970, Seyfried & Dibble, 1980; Janecky & Seyfried, 1986; Allen & Seyfried et al., 2003; Seyfried et al., 2007; Godard et al., 2013, Klein et al., 2015; McCollom et al., 2016; Wegner & Ernst, 1983; Normand et al., 2002; Ogasawara et al., 2013; Okamoto et al., 2011; Marcaillou et al., 2011).

Most previous experimental studies of serpentinization were conducted using pure water (distilled and/or deionized) (Bowen and Tutle, 1949; Martin & Fyfe, 1970; Wegner & Ernst, 1983; Normand et al., 2002; Ogasawara et al., 2013; Okamoto et al., 2011; Malvoisin et al., 2012; Marcaillou et al., 2011; Farough et al., 2016), and in some cases seawater-like fluids (Janecky & Seyfried, 1986; Allen & Seyfried et al., 2003; Seyfried et al., 2007; Malvoisin et al., 2012; Godard et al., 2013, Klein et al., 2015; McCollom et al.,

2016). Only a few studies addressed the potential effects of fluid composition on reaction progress and products ((Poty et al., 1972; Janecky & Seyfried, 1986).

In spite of the significant research activity related to serpentinization in natural systems and laboratory experiments in recent years, many details of the kinetics of the hydration reactions of ultramafic minerals are still not well constrained. Only a few studies have specifically examined reaction rates for serpentinization of olivine (Martin & Fyfe, 1970; Wegner and Ernst, 1983; Lafay et al., 2012, Malvoisin et al., 2012; Andreani et al., 2013). For similar conditions, the reported reaction rates differ by several orders of magnitude and with no clear evidence of the controlling factors that affect reaction rates (Malvoisin et al., 2012; McCollom et al., 2016).

It has been suggested that salinity can have a significant effect on mineral dissolution (Cadore, 1995; Schott et al., 2009; Casey & Westrich, 1992; Morrow et al., 2014; Yardley and Bodnar, 2014; Olsen et al., 2015) and nucleation and growth processes. The salinity of a fluid can affect the dissolution process by increasing the ionic strength of the solution, which affects the activities of the activated complexes or by decreasing the activity of water in the solution, which reduces its participation in the dissolution mechanism (Olsen et al., 2015), and by influencing pH (Yardley and Bodnar, 2014). Because water activity (a_{H_2O}) is a function of the osmotic coefficient of the solute, water activities in solutions of the same ionic strength but containing different solutes may be very different (Robinson and Stokes, 2002).

In this study, we developed a new experimental approach using synthetic fluid inclusions (SFI) as micro-batch reactors that allows us to monitor reaction progress during the serpentinization of olivine. Using this method, we monitored the extent of

reactions in real time and *in situ*, and as a function of initial salt concentration and composition. The results provide new insights concerning the reaction products being produced in real time, their order of appearance, abundances, compositions and the rate of reaction during serpentinization.

2. Methodology and analytical procedures

2.1 Experimental methods

In this study 12 experiments were conducted to understand the effects of fluid concentration (salinity) and composition in the hydration of olivine. The experiments involved the formation of the synthetic fluid inclusions in olivine at high temperatures where olivine + water are stable, followed by the serpentinization of olivine at a lower temperature where olivine will react to form serpentine.

2.1.1 Formation of Synthetic Fluid Inclusions

Synthetic fluid inclusions (SFI) in olivine were used previously to trap fluids at magmatic PT conditions (Johnson & Jenkins, 1991), to understand fluid behavior at mantle conditions (Bali et al., 2013), and as a means to analyze fluids produced by dehydration reactions at subduction environment PT conditions (Spandler et al., 2014). For this study, the SFI were synthesized according to procedures described by Sterner and Bodnar (1984) and Bodnar and Sterner (1987).

Individual olivine crystals (3 to 5 mm in diameter) were examined in immersion oil using a petrographic microscope, and crystals free of fluid and solid inclusions and containing no visible fractures were selected. After cleaning the crystals in soapy water followed by boiling in distilled water to remove the immersion oil, the selected crystals were heated to 700°C in an oven, and then quenched by dropping the crystals into a

beaker containing distilled water. The thermal shock produced numerous micro fractures extending into the crystal from the edge, similar to the types of fractures that are generated in quartz for SFI studies (Sterner and Bodnar, 1984). Following this initial fracturing, the crystals were placed into a vacuum oven at ~110°C overnight to remove any water that may have entered the fractures during the quench. For each experiment, a single cleaned and dried crystal was loaded into a platinum capsule along with an aqueous solution of known composition.

We conducted 8 experiments with an H_2O-NaCl-$MgCl_2$ fluid with seawater Na:Mg mass ratio (8:1; corresponding to a NaCl/$MgCl_2$ mass ratio of ~5.2), with concentrations of 1, 3.5, 6 and 10 wt.% total salt. To assess the role of fluid composition in the serpentinization process, additional experiments were conducted using binary solutions of H_2O-NaCl and H_2O-$MgCl_2$ with the concentrations of 3.5 and 10 wt.% total salinity.

A fractured olivine crystal along with approximately 100 µl of solution was loaded into a 5 mm OD and ~2.5 cm long platinum capsule. The loaded capsules were sealed with an arc welder and weighed to determine the total weight of the loaded capsule before the experiment, and then placed into cold-seal pressure vessels. Pressure and temperature were increased to 5.5 kbar and 600 ºC (Fig. 3), and the capsules were held at these conditions for 30 days. At the end of the experiment, the bombs were removed from the furnace and, after air-cooling; the capsules were removed from the pressure vessels and weighed to confirm that the capsules had not leaked during the experiment. Any capsule whose weight after the run differed from that before the experiment (within analytical uncertainty) was discarded. The crystals were removed from the capsules and mounted in thermal cement for cutting and polishing. The polished chips (~1 mm thick)

were examined petrographically to confirm the presence of fluid inclusions along the healed fractures, and several thousand SFI were found in each chip. Then, one chip from each sample was analyzed in the heating/cooling stage to confirm that the trapped inclusions had the correct density (homogenization temperature) corresponding to the P-T formation conditions. The homogenization temperatures are a function of not only the formation conditions but, also, the salinity, which affects the slopes of the isochores. For the formation conditions and salinities of the fluids in this study, homogenization temperatures ranged from ~225°C to 240°C. Finally, if all of these tests confirmed that the crystals had trapped fluid inclusions at the experimental conditions and that the composition and density of the SFI were consistent with run conditions and the composition loaded into the capsule, one or more chips were selected for further monitoring of reaction progress during serpentinization. The sizes of the SFI varied between 1 μm to 100 μm, with an average of ~10 μm.

During synthesis we observed a systematic difference in the size and abundance of the SFI as a function of initial fluid composition loaded into the capsule. The SFI in the experiments with H_2O-$MgCl_2$ were more abundant, larger (up to several 100s μm) and more equant and three-dimensional. Olivine overgrowths on the original crystal were observed for some of the crystals in which SFI containing high $MgCl_2$ concentrations were trapped, and primary SFI were trapped in these overgrowths.

The experiments in $MgCl_2$-free fluids produced SFI that were significantly smaller (~ 5 to 10 μm) and more irregularly shaped. One experiment was conducted using pure H_2O, however the SFI produced were very small (<1μm), scarce and the fractures were poorly healed. These SFI were not used during the serpentinization experiments. One

possible explanation for the relationship between fluid composition and SFI size and abundance is that the presence of Mg might help to promote the healing of fractures in olivine and lead to the trapping of larger and more abundant fluid inclusions.

2.1.2 Serpentinization experiments

For each fluid composition and concentration, several SFI in each chip were selected to monitor the serpentinization reaction progress. Each inclusion was photographed and mapped with an optical microscope to record the original shape, phase assemblage (liquid + vapor for all of the SFI after synthesis when observed at room temperature; see Fig. 1A, 0 days) and location of the selected SFI within the sample chip. Then, individual disks containing SFI were placed in a furnace at ~280 ºC and ambient P (~1 bar). Note that, even though the confining pressure on the sample was ~1 bar during this part of the experiment, the pressure in the SFI was considerably higher and was controlled by the density of the fluid in the inclusion. The P-T conditions of trapping were chosen such that the internal pressure in the SFI would be ~500 bar at 280 ºC depending on the concentrations. The polished olivine disks containing synthetic fluid inclusions were removed from the furnace every 5 or 20 days, photographed (see Fig. 1A; 15, 30, 45 and 120 days) and examined petrographically and by Raman spectroscopy and then returned to the furnace. Initially all samples were removed from the furnace and examined every 5 days, but after several 5-day sequences showed no evidence of reaction for the higher salinity SFI. Subsequently, these samples were removed every 20 days and examined. The maximum amount of time that the samples were out of the furnace for these measurements and analyses was ~1 day before being returned to the furnace at 280°C for the serpentinization reaction to continue.

It is not clear whether the thermal cycling (episodically quenching the SFI from 280°C to room temperature for analysis and then heating again to 280°C) used in this study affects the dissolution/precipitation process, compared to maintaining the sample at a constant temperature. In order to confirm that repeatedly cycling the samples from 280°C to room temperature and back to 280°C photograph and analyze the SFI did not affect the results, we conducted an additional experiment using a Chaixmeca microscope heating stage (Poty et al., 1976) to follow the reaction progress without the need to cool the experiment to room temperature for observation or analysis. Two samples of olivine with SFI of two different fluid compositions (1 wt.% and 3.5 wt.% H_2O-NaCl-$MgCl_2$) were used to monitor the reaction progress in this constant temperature experiment. The samples were heated to ~280°C and monitored petrographically and analyzed by Raman spectroscopy every 2 days to monitor reaction progress for 120 days.

2.2 Mineral and chemical analyses

2.2.1 Raman

After each heating period, the SFI were removed from the furnace, examined petrographically, photographed, and analyzed by Raman spectroscopy. Raman is an ideal method to characterize the phases in the SFI because it is non-destructive and can analyze a spot with ~1 micron diameter. Importantly, the confocal nature of the Raman system has excellent depth control and thus allows us to eliminate signal from material above and below the target to obtain high-quality spectra of phases that are below the sample surface. Raman analyses were performed in the Department of Geosciences at Virginia Tech using a JY Horiba LabRam HR (800 mm) spectrometer, with a 600 grooves/mm grating. The slit width was set to 150 μm, and the confocal aperture at 100 μm.

Excitation was provided by a 514.529 nm (green) Laser Physics 100S-514 Ar+ laser. The laser output was 50 mW at the source and ~10 mW at the sample. The laser was focused through a 40× objective (N.A. = 0.55). The detector used is an electronically cooled open electrode 1024 pixel CCD. The mean value of three collections of 45 seconds each was taken to determine the Raman peak positions at each pressure. Data were collected over the spectral range 100 to 4200 cm^{-1} using 3 accumulations of 30 seconds each.

Raman X-Y mapping was conducted at Woods Hole Oceanographic Institute using a JY Horiba LabRam HR confocal Raman spectrometer with a 473 nm laser source and a 600 groove/mm grating. A 100× objective with a 100 μm confocal aperture was used for mapping. Maps were constructed with a 1 x 1 μm spatial resolution and the spectra were collected using 3 accumulations of 20 seconds each.

2.2.2 Electron Microprobe Analysis (EMPA)

The chemistry of the olivine host crystal used in experimental run 3, and later used for the TOF SIMS analyses, was determined on a Cameca SX-50 electron microprobe in the Department of Geosciences at Virginia Tech. Accelerating potential was 15 kV, 20 nA current and 1 μm beam size, using natural and synthetic mineral standards for calibration. Relative analytical error is better than 1 % (1σ) except for element concentrations <1 wt.%, where the analytical error is better than 4 % (1σ).

2.2.3 TOF-SIMS

Chemical analyses of the contents of the SFI (both solids and fluids) after the serpentinization experiments were conducted using time of flight secondary ion mass spectrometry (TOF-SIMS) (Chou et al., 2015; Zu et al., 2015; Colleary et al., 2015) at the Texas Materials Institute at the University of Texas at Austin. At each step during the

analysis, the ion beam consisting of Bi^{1+} ion pulses (30 keV ion energy) was first set in the high current bunched mode (HC, 20 ns pulse duration, ~3.7 pA measured sample current, ~1 um lateral resolution) to determine the masses of interest with high mass resolution. The beam was typically rastered over areas of 100 x 100 um or 200 x 200 um depending on the region of interest. Then, the beam was set in the burst alignment mode (BA, 100 ns pulse duration, ~0.03 pA measured sample current, ~200 nm lateral resolution) to produce high spatial resolution maps of the selected regions for all masses of interest. To expose the SFI in the olivine hosts at various depths we used an O^{2+} sputtering ion beam (1 keV ion energy, ~300 nA measured sample current) that was rastered over an area of 500 x 500 um and centered over the region of interest. The resulting sputtering rate was calculated at 0.3 nm/s. The sample was maintained at a base temperature of -100ºC at all times during the analysis by inductive liquid nitrogen cooling to prevent the water from desorbing from the exposed SFI. All detected ions have positive polarity when the analysis was performed at a 10^{-9} mbar base pressure. A constant current (21 eV electron energy) electron beam was focused on the sample during data acquisition to reduce sample charging. The mass resolution is >3000 and >100 (m/dm) for the HC and BA modes, respectively. To avoid signal saturation, ^{25}Mg (rather than the more abundant ^{24}Mg) was used to estimate the Mg concentration.

The TOF-SIMS provides ratios of the number of counts for one mass (isotope) to the number of counts for some other isotope, and these counts had to be converted into a concentration ratio. To do this, the count ratio for Mg and Fe was converted into a concentration ratio using the known Mg to Fe concentration ratio of the olivine host obtained from EMPA (Table 1) and the count ratio obtained by TOF SIMS analyses for

this same area of the crystal. For this comparison, two $^{25}Mg/(^{25}Mg + ^{56}Fe)$ count ratios obtained from TOF-SIMS analyses were calculated from carefully selected regions of interest analyzed from the BA mode maps. One of these ratios represents the average stoichiometry of the olivine matrix from a region of interest outside of the SFI, and the other represents the reaction products inside the exposed SFI. The Mg# of the reaction products was then calculated using the correction factor based on the Mg# of the olivine host obtained by EMPA and that obtained from TOF-SIMS analysis.

2.2.3 FIB-SEM

In order to expose the SFI to obtain images of the reaction products we used a Helios 600 NanoLab FIB-SEM in the Nanoscale Characterization and Fabrication Laboratory (NCFL) at Virginia Tech. The instrument is equipped with an Omniprobe 200.2 with a 3-nozzle gas injection system to deposit platinum for insulator-enhanced etching.

2.2.4 TEM

TEM images were obtained with a JEOL 2100 TEM thermionic emission analytical electron microscope in the Nanoscale Characterization and Fabrication Laboratory (NCFL) at Virginia Tech. Samples were prepared for TEM analysis by first polishing the chip manually to bring the target SFI close to the sample surface, with final milling to open the SFI using a Fischione Ion Mill.

2.3 Monitoring reaction progress

Each SFI represents a closed system reaction vessel in which material can only be exchanged between the aqueous solution and the surrounding host phase (olivine) as the reaction proceeds. During the hydration of olivine in the serpentinization reaction H_2O is

removed from the solution and incorporated into hydrous phases, while Na^+ and Cl^- are assumed to be conservative and remain in the solution. Note that small concentrations of Cl^- can be incorporated into the serpentine molecular structure substituting OH^- (Miura et al., 1981; Sharp & Barnes, 2004). However, the concentrations of Cl^- found both in natural serpentines as well as in lab experiments are small, ranging from 0.1 to 0.4 wt.% of Cl^- (Boschi et al., 2013; Frost et al., 2009; Klein et al., 2015), with rare reported concentrations of ~1 wt.% Cl^- (Schwarzenbach et al., 2016). The changes in the overall salinity produced by incorporating a 1 wt.% of the Cl^- are negligible. For example, in a fluid with a 3.5 wt.% salinity, the change in salinity produced by incorporating 1 wt.% of the Cl^- into the serpentine crystals are ~0.02 wt.%. As explained further in this section, a change in salinity of this magnitude is below the sensitivity of the FPD.

For the experiments in which the starting solution contained $MgCl_2$, some of Mg^{2+} will be removed from or added to the solution by dissolution and precipitation. However, some of the Mg^{2+} will be conservative in order to maintain charge balance to the Cl^-. To monitor the amount of H_2O removed from the solution we measured the freezing point depression (see Bodnar, 2003) and interpreted the data assuming a pure H_2O-NaCl solution. Although the dissolution of olivine would have added Mg, Si and Fe to the solutions during the reaction, their concentrations are expected to be low (10s to 100s of ppm) and would have an insignificant effect on the freezing point depression.

The salt concentration monitored by measuring the freezing point depression of the aqueous phase (temperature of melting of the last ice crystal, Tm) in the SFI using a Linkam THMSG 600°C heating and freezing stage. Each measurement was corrected for analytical error by measuring the Tm of a pure H_2O SFI. Note that the chip containing the

pure H_2O SFI and that containing the SFI from the serpentinization experiments were adjacent to each other in the heating/cooling stage, making it possible to easily move back and forth between the two samples to measure the SFI. The correction factor ranged from 0.8 to 1.0ºC, and the precision of the FPD measurements is considered to be ~ ±0.1˚C. The salinity (wt.% eq. NaCl) as a function of the FPD was calculated by using the equation of Bodnar (1993).

At each step (i.e., after some time increment of heating at ~280°C), the SFI being monitored were photographed and the appearance of the SFI was compared with photographs of the SFI after synthesis and before the reaction experiments, and with photographs taken after previous heating steps (see Fig. 1A). Note that the salinity does not vary linearly with the FPD. Hence, the uncertainty in salinity associated with the error of the FPD measurement (~ ±0.1˚C) decreases as salinity increases. For example, the salinity uncertainty associated with an FPD of -0.1ºC ±0.1˚C is 0.35 wt.%, whereas the salinity uncertainty associated with an FPD of -1ºC ±0.1˚C is 0.34 wt.%, and the salinity uncertainty associated with an FPD of -10ºC ±0.1˚C is 0.21 wt.%.

The reaction progress is expressed in terms of the extent of a reaction (ξ), which is defined as the number of moles (n) of reactant consumed or product generated since the start of the reaction along with the stoichiometric coefficient (ν) for the phase being consumed or produced

$$\left(n_i\right)_t = \left(n_i\right)_{t=0} + \nu_i \xi \tag{3}$$

Based on this definition, the rate of reaction is defined as the time (t) derivative of the extent of reaction.

$$\frac{d\xi}{dt} = \frac{1}{\nu_i}\frac{dn_i}{dt} \tag{4}$$

As such, the rate of reaction (4) can be defined in terms of the rate of change in the amount of any of the phases that participate in the reaction.

$$\frac{d\xi}{dt} = -2\frac{dn_{fo}}{dt} = -3\frac{dn_{\mathrm{w}}}{dt} = \frac{1}{1}\frac{dn_{chr}}{dt} = \frac{1}{1}\frac{dn_{bru}}{dt} \tag{5}$$

where the subscripts *fo*, *w*, *chr* and *bru* stand for forsterite, water (H_2O), chrysotile and brucite, respectively. In this study H_2O was used as the reaction progress variable and the reaction rate was calculated from the time rate of change of H_2O content in the aqueous phase in the SFI. The amount of H_2O in the inclusion was determined from the salinity established by measuring the freezing point depression of the liquid remaining after various stages of reaction progress. For example, a spherical fluid inclusion with a diameter of 10 μm has a volume of 5.24×10^{-10} cm^3. If the fluid inclusion trapped a 3.5 wt. % H_2O-NaCl solution at 600°C and 5.5 kbar the fluid density would be 0.870 g/cm^3. Accordingly, the inclusion would contain 4.56×10^{-10} g of aqueous solution, or 1.60×10^{-11} g of NaCl and 4.40×10^{-10} g of H_2O. This inclusion would have a freezing point depression (FPD) of -2.1°C. If, after some amount of reaction, the measured FPD is -2.4°C, the salinity of the aqueous solution would be 4 wt.% NaCl. As NaCl is conservative and only H_2O has been removed from the solution during the reaction, the amount of H_2O in the fluid inclusion corresponding to a salinity of 4 wt. % NaCl and a total NaCl content of 1.60×10^{-11} g is 3.84×10^{-10} g. Thus, during the reaction as the salinity of the aqueous phase in the SFI increased from 3.5 wt.% to 4 wt.% NaCl, 5.6×10^{-11} g of H_2O was removed from the aqueous solution and incorporated into hydrous

phases. Stated differently, ~13 mass percent of the H_2O originally in the aqueous solution has been incorporated into hydrous phases during reaction, as the salinity of the aqueous phase increased from 3.5 to 4 wt.% NaCl.

2.3.1 Initial Rate Method

Reaction progress was followed in several hundred SFI inclusions by measuring the changes in salinity with time. The salinities were recalculated to moles of H_2O consumed by calculating the number of moles of H_2O that must be removed from the solution to increase the salinity to the value corresponding to the new FPD, as described above. The mass balance calculations are attached as Appendix A. The number of moles of H_2O consumed by the serpentinization reaction with time was incorporated into the initial rate method:

$$r = \frac{dn_w}{dt} \tag{6}$$

where r is the rate of reaction in moles per sec, n_w is the moles of H_2O, and t is the change in time (t) in seconds. The number of moles of H_2O removed from solution and incorporated into hydrous phases as a function of time (t) for every SFI was fit by a linear regression model and the rate of reaction was taken as the slope of the regression line (Laidler, 1987; Rimstidt and Newcomb, 1993). Previous studies have shown that the initial rate method yields comparable results to other dissolution rate methods (Rimstidt and Newcomb, 1993).

Because the reaction is taking place at an interface that separates two phases (solid and liquid), the rate expresses how fast a component is transferred to or from that interface, and the area of the interface must be taken into account as follows:

$$J = \frac{r}{A} \tag{7}$$

where J is the flux of H_2O, defined as the rate of H_2O consumption per unit surface area (mol/m^2sec), r is the rate of H_2O consumption in mol/sec, and A is the surface area of a 10 μm spherical fluid inclusion (1.26×10^{-09} m^2).

In our experimental method, we quantify the rates of serpentinization based on the amount of water removed from the aqueous solution and incorporated into hydrous phases. We use the freezing point depression (FPD) as a proxy for the amount of water removed from solution, and the sensitivity (precision) of our FPD measurement is ±0.1°C. However, some amount of H_2O must be removed from the solution and incorporated into hydrous phases before the salinity is increased by an amount sufficient to produce a 0.1 degree Celsius lowering of the FPD. The actual amount of H_2O that must be removed from solution to produce a 0.1 degree Celsius lowering of the FPD is also a function of the starting salinity (see Appendix A). Thus, if the initial salinity is 1 wt.% NaCl (FPD=-0.6°C), ~17 percent of the H_2O in the initial fluid must be consumed by hydration reactions to drive the FPD lower by 0.1 degree Celsius to -0.7°C (corresponding to a salinity of ~1.2 wt.% NaCl). However, the same 0.1 degree Celsius lowering of the FPD for a starting salinity of 10 wt.% NaCl requires consumption of only 1.1% of the initial H_2O, as the FPD is lowered from -6.6°C (10 wt.% NaCl) to -6.7°C (10.1 wt.% NaCl). Thus, until a sufficient amount of reaction has occurred to consume enough H_2O to lower the FPD by ≥0.1 degree Celsius, we would not know *a priori* that the reaction has started and, depending on the starting salinity, the amount of H_2O consumed (and, therefore, the amount of reaction) could vary from ~1 to 20 percent of the initial H_2O. We have direct evidence that reactions have started before they are recorded by a measureable lowering of the FPD because we often observed reaction

products in the SFI with no detectable change in FPD. As such, our linear regressions include data for that part of the experiment in which the FPD was decreased by ≥0.1 degree Celsius from the initial value, recognizing that the actual reaction likely began at some time between the beginning of the heating experiment and the time at which a change in FPD was first recorded. All the data were fit using multiple linear regressions with the JMP statistical software package.

2.3.2 Rate equation

To produce geochemical rate models, rates obtained as described above were converted into rate equations that summarize the effects of solution compositions (Rimstidt, 2014). These experimental rates were fit to an equation that relates the rate the concentration (*m*, molal) of each reacting species, *i,* raised to a power (*n*).

$$r = k\Pi m_i^{n_i} \tag{8}$$

This equation was transformed to a linear form:

$$\log r = \log k + \Sigma n_i \log m_i \tag{9}$$

The data were fit to an equation of this form using linear regression analysis to find the rate constant (k) and the apparent reaction order (n).

2.4 Thermodynamic modeling

The *in situ* speciation of the reacting fluids, activity of water ($a_{\mathrm{H_2O}}$) and reaction product compositions were estimated using the software code EQ3/6 (Wolery, 1992) and a thermodynamic database for 50 MPa as described in Klein et al (2013). We used a solution with the composition of starting solutions of our experiments and equilibrated the solution with olivine (Fo85) at 280ºC, in a closed system with a water to rock ratio of

1 to 1 (1 kg of water and 1 kg of olivine) and let it react with the olivine until all the olivine was consumed by the reaction.

To determine the equilibrium constants (log *k*) at different temperatures for the reaction described by Eq. (1) we used SUPCRT92 (Johnson et al., 1992). The equilibrium constants were used to calculate the chemical potential of the reaction as a function of T and a_{H2O} (see discussion).

3. Results

3.1 Mineral characterization of the reacting products

Twelve different SFI experiments were conducted at serpentinization conditions of ~280ºC (Table 1). After a few days at the run conditions, small crystals were recognizable in some of the SFI, and as time progressed more crystals appeared (Fig.1). Often these small reaction products were observed without a measureable change in FPD. Usually one or several clusters of crystals started growing on the walls of the inclusion and continued growing inward away from the walls as time progressed. The newly formed crystals in the SFI are submicron in size, precluding optical identification. However, two common textural and optically distinct characteristics were observed in all 12 experiments. The phase identified as brucite showed a clear euhedral platy shape, whereas the serpentine phases growed in small concentric clusters that with time become opaque. The abundance of the reaction products steadily increased with time, and the SFI became progressively less transparent until the inclusion eventually becomes opaque (Fig. 1). The opacity that develops in the SFI as the reaction proceeds is analogous to the behavior of transparent aqueous inclusions when they are cooled rapidly and, after considerable undercooling, the liquid crystallizes to produce a very fine-grained mixture

of ice and various salt hydrates. Owing to the abundance of many tiny facetted crystals in the inclusion, light passing through the inclusion is both reflected and refracted such that little light is transmitted through the inclusion to the eye of the observer.

Raman analyses were performed after each increment of heating to identify the reaction products (Table 2). In all experiments the crystal clusters were composed of serpentine minerals (lizardite and/or chrysotile), and the clear, euhedral crystals were brucite (Fig. 3). Magnetite was also found in the experiments of at least 120 days duration (Fig. 1).

The FIB-SEM technique was used to mill through the olivine host to expose the SFI and obtain high-resolution images of the reaction products (Fig. 4A-B). The mineral clusters observed with the optical microscope are comprised of small conical and fibrous serpentine crystals. TEM images clearly show the chrysotile fibers (Fig. 4C-D).

3.2 Chemical characterization of the reaction products

TOF-SIMS analyses were performed to characterize the chemical composition of the reaction products (Table 3). The "areas" corresponding to the chemical analyses listed in Table 3 refer to the areas containing reaction products in SFI as shown in Figure 5. The SFI selected for this analysis was a large, irregularly-shaped inclusion (~100 μm) with well characterized visible crystals of brucite and clusters of serpentine (Fig. 3). Seven areas of the SFI (labeled I-VII, Fig. 5) in which Raman analyses identified serpentine and brucite where analyzed by TOF-SIMS to determine the compositions of these phases. The brucite compositions have Mg# = 87- 88 and serpentines have an Mg# ranging from 90-94. The average of the EMPA analyses on the olivine host for the SFI are tabulated in Table 4 and indicate an Mg# of 85.

3.3 Rates of reaction

The results of all the SFI micro-batch reactor experiments, including rates of reaction (r), fluxes (J), and calculated activities of water (a_{H_2O}) are tabulated in Tables 5 and 6, along with the solution chemistry.

3.3.1 Effects of salinity and fluid composition on reaction progress

Our data shows distinct differences in the amount of time at 280°C before evidence of reaction is observed, either by observable crystals in the SFI or a measureable change in the freezing point depression, as a function of the initial salinity and composition.

We emphasize that the reaction of aqueous fluid with olivine to produce serpentine and brucite likely begins slightly before we see optical or microthermometric evidence of reaction progress. As noted above, it is not possible to recognize that the reaction has begun until the salinity has changed by an amount sufficient to lower the freezing point depression of the solution by >0.1°C, due to the analytical sensitivity of the FPD measurement. Alternatively, evidence that the reaction has begun is provided if serpentine and/or brucite crystals can be observed in the SFI. Thus, some amount of reaction must occur before evidence in the form of a decrease in FPD of >0.1°C or presence of reaction products are detected.

In the experiments with an aqueous solution in the system H_2O-NaCl-$MgCl_2$ (Na/Mg mass ratio of 8 to 1), ~50% of the SFI in experiments with 1 wt.% total salinity showed reaction products within the first 5 days, whereas during the same period of time only ~20% of the SFI with the 3.5 wt.% solution showed evidence of reaction. For the experiments with 6 wt.% salt, ~5 % of the SFI showed evidence of reaction after 5 days, and in the 10 wt.% experiments none of the inclusions show any indication of reaction

after 5 days. Experiments with H_2O-NaCl (3.5 and 10 wt.%) showed similar results, with fewer SFI showing evidence of reaction in the higher salinity sample compared to the lower salinity sample. For the H_2O-$MgCl_2$ sample (3.5 and 10 wt.%), no evidence of reaction was observed in either sample after ~4 months, but when the sample was examined again after ~ 7 months incipient reaction was observed - serpentine and brucite were confirmed by Raman but no measureable change in FPD was observed. Note that in order to detect a measureable change in the FPD for these two starting compositions (≥0.1 degree Celsius change), the salinity of the 3.5 wt.% $MgCl_2$ starting fluid would have to increase to ~3.7 wt.% $MgCl_2$ (corresponding to consumption of ~6 mass percent of the H_2O in the original solution), and salinity of the 10 wt.% $MgCl_2$ starting fluid would have to increase to ~10.1 wt.% $MgCl_2$ (corresponding to consumption of ~1 mass percent of the H_2O in the original solution). Thus, some amount of reaction could have occurred without changing the FPD by a detectable amount.

Once the reaction starts, the amount of H_2O consumed increases with time (Fig. 6A). As noted above, we are unable to detect that the reaction is occurring until a change in salinity is observed based on a measureable difference in the FPD compared to that of the starting solution (±0.1ºC). A linear regression to the salinity versus time data of all SFI that showed evidence of reaction during the time of our observations, and the slope of the line defined the rate of reaction as shown in Figure 6B. The FPD measurements, calculated salinities, moles of H_2O consumed and time at the experimental conditions for all the SFI are tabulated in Electronic Appendix B. The experiments with H_2O-NaCl and H_2O-NaCl-$MgCl_2$ concentrations of 3.5 wt.% were monitored until the reaction proceeded to the extent that further microthermometric measurements were not possible

because the liquid phase could not be resolved optically, i.e., the SFI was completely filled with solid reaction products (Fig. 1).

Experiments 1 wt.% H_2O-NaCl-$MgCl_2$ solution

Experiments conducted with a starting composition of 1 wt.% H_2O-NaCl-$MgCl_2$ show evidence of reaction within the first two days in some inclusions based on the presence of small crystals in the SFI (but without a measureable change in FPD), and most of the inclusions formed reaction products within 30 days. The average reaction rates calculated for this starting composition are 8.48×10^{-18} mol/sec and fluxes of 6.73×10^{-9} mol/m^2sec. SFI with this same composition were heated in the Chaixmeca stage and held at 280°C continuously (without quenching to room temperature for analysis) so that reaction progress could be monitored optically and by Raman spectroscopy daily. Salinity changes were not monitored (because we could not cool the SFI to measure FPD) but the appearance and overall progression of the reaction to eventually produce SFI that were opaque owing to precipitation of reaction products occurred in the same time frame as with the other experiments in which SFI were regularly removed from the furnace for Raman analysis at room temperature and to measure the FPD. The mineral assemblages observed in the experiment include magnetite, in both the experiments in the furnace with episodic quenching and the continuous heating experiments in the Chaixmeca stage. Magnetite is evidenced by the appearance of small opaque crystals that are identified as magnetite by Raman analysis. Note that magnetite only appears in the experiments that lasted longer than 120 days.

Experiments with 3.5 wt.% H_2O-NaCl-$MgCl_2$ solution

In these experiments, reaction was first observed in several of the inclusions being monitored within the first 5 days at serpentinization conditions, evidenced by the presence of small crystals forming on the SFI walls. The average rate of reaction for this fluid composition is 3.66 $x10^{-18}$ mol/sec with a flux of H_2O of 2.91 $x10^{-9}$ mol/m^2sec. An experiment with this composition was conducted using the Chaixmeca stage to monitor reaction progress optically and by Raman spectroscopy daily. Salinity changes were not monitored but the overall progression of the reaction to produce SFI that were opaque owing to mineral precipitation occurred in the same time frame as the other experiments in which the SFI were episodically removed from the furnace for analysis. The mineral assemblage observed in this experiment includes magnetite, in both the experiments in the furnace with episodic quenching and the continuous heating experiments in the Chaixmeca stage. Magnetite is evidenced by the appearance of small opaque crystals that are identified as magnetite by Raman analysis. Magnetite appeared only in experiments that lasted longer than 120 days.

Experiments with 6 wt.% H_2O-NaCl-$MgCl_2$ solution

After 5 days, brucite and serpentine were observed in a smaller proportions in the SFI compared to the experiments with this same composition but salinities of 1 and 3.5 wt.%. The average rate of 1.06 x 10^{-18} mol/sec and the H_2O flux of 28.39 x 10^{-10} mol/m^2sec measured from this concentration are slightly slower than values obtained in experiments with this same composition but with salinities of 1 and 3.5 wt.%. No magnetite was observed throughout the duration of this experiment.

Experiments with 10 wt.% H_2O-NaCl-$MgCl_2$ solution

No reaction products were observed after 60 days in SFI in which the starting composition was 10 wt.% H_2O-NaCl-$MgCl_2$, after 60 days measuring SFI every 5 days. After 270 days, evidence of reaction was observed in ~10% of the SFI based on the presence of crystals and a measured FPD that was >0.1 degree Celsius different from the original FPD. The average rate determined for this composition is 8.97 x 10^{-20} mol/sec and the flux of H_2O is 7.12 x 10^{-11} mol/m^2sec, both of which are significantly slower than those obtained for this same composition but with salinities of 1, 3.5 and 6 wt.%. The mineral assemblage observed in the SFI in this experiment includes magnetite, as evidenced by the appearance of small opaque crystals that are identified as magnetite by Raman analysis.

3.3.2 Effects of fluid composition on the reaction progress

To compare the results described above for a seawater-like starting composition containing both NaCl and $MgCl_2$, experiments were also conducted using Mg-free starting compositions and Na-free starting compositions.

H_2O-NaCl fluids

Two experiments were conducted in the system H_2O-NaCl with salt concentrations of 3.5 and 10 wt.% (Table 6). For the 3.5 wt.% concentration no significant differences were observed in the order of appearance of the reaction products, the abundances of mineral products, or the reaction rates, compared to the results for this same salinity in the ternary H_2O-NaCl-$MgCl_2$ system. For this salinity (3.5 wt.%), the rates of reaction obtained from experiments using H_2O-NaCl (3.76 x 10^{-18} moles/sec) are within the experimental uncertainties to that obtained in experiments using H_2O-NaCl-$MgCl_2$ of the same salinity (3.66 x 10^{-18} moles/sec). In the experiment conducted with a starting composition of 10

wt.% H_2O-NaCl, no reaction was observed in any of the SFI during the first 60 to 90 days at 280˚C, similar to results for the ternary fluid composition of the same total salinity. After 270 days, several SFI in both the experiments with 10 wt.% H_2O-NaCl and 10 wt.% H_2O-NaCl-$MgCl_2$ showed evidence of reaction based on the presence of serpentine + brucite ± magnetite in the SFI (identified both optically and by Raman analysis). Approximately 40 to 50% of SFI with a starting composition of 10 wt.% H_2O-NaCl show evidence of reaction, compared to ~10-20% of the SFI in the 10 wt.% H_2O-NaCl-$MgCl_2$ experiment. Additionally, rates of reaction in the 10 wt.% H_2O-NaCl experiments are slightly faster at 1.23×10^{-19} moles/sec, compared to the 8.97×10^{-20} moles/sec for the H_2O-NaCl-$MgCl_2$ solution of the same salinity.

$MgCl_2$-H_2O fluids

Two experiments in the system H_2O-$MgCl_2$ and concentrations of 3.5 and 10 wt.% were conducted to determine if the presence of Mg in the starting fluid affects rates of serpentinization. No evidence of reaction was observed in the selected SFI during the first 60 days of observation. The samples were kept continuously at 280ºC for an additional 210 days (270 days total). After this time, small crystals of brucite + serpentine ± magnetite were identified optically in a few of the SFI. Although reaction of the solution with the olivine host to produce serpentine phases occurred based on optically examination, no changes in the FPD were observed for this composition.

3.4 Rate equation

A rate equation was generated by fitting the rates of reaction obtained as described above using a linear regression to and plotting the log of the flux (J) versus log activity of H_2O (a_{H2O}) (Fig. 7A and 8A).

The rate equation for the H_2O-NaCl-$MgCl_2$ experiments is given by:

$$log\ J = -7.76(0.04) + 120.28(4.17)\ log\ a_{H_2O} \quad (10)$$

where -7.76 is the log rate constant, and 120.28 is the apparent reaction order. The rate equation for the H_2O-NaCl experiments is given by:

$$\log J = -7.64(0.11) + 127.06(7.52) \log a_{H_2O} \quad (11)$$

where -7.64 is the rate constant, and 127.06 is the apparent reaction order. The two rates are the same, within the uncertainty of the experiments, with the reaction rate determined for the H_2O-NaCl composition being slightly faster than that for the H_2O-NaCl-$MgCl_2$ compositions.

Residual plots showing the difference between calculated fluxes ($log\ J$) predicted by Eq. (10 and 11) and the fluxes (rates) determined from individual SFI are shown in Figures 7B and 8B. The total dispersion (1σ) of the data for the H_2O-NaCl-$MgCl_2$ experiments is 1σ=0.08 log units, and for the H_2O-NaCl experiments the dispersion is 1σ=0.1 log units.

4. Discussion

4.1 Mineralogy and chemistry of the reaction products

The reaction products in all experiments are serpentine (chrysotile and/or lizardite) + brucite ± magnetite. The identification of the serpentine phase as either chrysotile or lizardite was not always possible using Raman. The reasons for this are that chrysotile and lizardite both show major peaks in approximately the same spectral range (±~10 cm^-

[1]), and the actual positions of these peaks for a given phase vary by several wavenumbers from the nominal position owing to slight variations in composition, crystal structure, orientation, etc. (Lewis et al., 1996, Bard et al., 1997; Kloprogge et al., 1999; Rinaudo et al., 2003; Groppo et al., 2006; Kodalányi & Pettke, 2011; Moctar et al., 2013). For example, the lizardite peak with a nominal position of 228 cm^{-1} and the chrysotile peak with a nominal position of 230 cm^{-1} both appear between 224 and 232 cm^{-1} in our samples. Similarly, chrysotile peak with a nominal position of 388 cm^{-1} and the lizardite peak with a nominal position of 389 cm^{-1} both occur in the range from 385 to 394 cm^{-1}. Both chrysotile and lizardite have peaks at a nominal position of 690 cm^{-1} and in our analyses this peak appears at 685 to 695 cm^{-1}. The lizardite has a Raman peak at 1090 cm^{-1} and chrysotile has a peak at 1100 cm^{-1}, and our analyses of show peaks ranging from 1090 to 1100 cm^{-1}. Other minor peaks of the serpentine phases were not observed or overlapped with peaks from the olivine host. Similarly, peaks at higher wavenumbers corresponding to O-H stretching modes in the hydrous phases showed some variability in the peak position. Most of the serpentine crystals show an intense peak from 3698 to 3707 cm^{-1}, with less intense peaks between 3670 to 3690 cm^{-1} that would agree with chrysotile and lizardite. The FIB-SEM and TEM analyses show that the most likely serpentine phase present is chrysotile. Brucite shows similar variability in peak position, especially for peaks representing the O-H stretching modes that span from 3635 to 3650 cm^{-1} with minor peaks (shoulders) from 3624 to 3660 cm^{-1}. The serpentine and brucite crystals of our experiments grow in clusters of hundreds of nanometer crystals with different crystal orientations (Fig. 4A-D). Since the probe size of the Raman using a 100X objective is ~1 micron, the vibrational frequencies of several crystals of slightly

different compositions and at different orientations are being combined, resulting in a broadening of the Raman bands.

4.1.1 Chemical composition

The composition of the reaction products of our experiments was determined from TOF-SIMS analysis. These data indicate that chrysotile has a Mg# that ranges from 90 to 94, and brucite has a Mg# that ranges from 87 to 88. These values are in agreement with the compositions obtained from the thermodynamic simulations conducted in this study (Table 6) and with other studies (McCollom and Bach, 2009; McCollom et al., 2016; Klein et al., 2009b, 2013). The compositions calculated from TOF SIMS data are ~1 to 2 Mg# lower than the compositions predicted by EQ3/6 when the reaction progress $\xi = 0.5$. The model predicts that serpentine with a Mg# of 96 and brucite with a Mg# of 89 are produced by reacting olivine with a Mg# of 85 with our aqueous solution. The measured compositions are also in agreement with the average compositions of reaction products from other experimental studies (e.g., McCollom et al., 2016 and references within). The differences in compositions of the reaction products of our experiments (1 to 2 Mg# lower for our experiments) compared to other experiments can be explained because the olivine crystal host used for our experiments have a slightly higher iron content and a lower Mg# = 85 (Klein et al., 2013).

4.1.2 Magnetite formation

Magnetite was observed as a reaction product in approximately 50% of the experiments. However, magnetite was only observed in experiments of long duration. According to Eq. (2), loss of H_2 from the system forces the reaction to the right, i.e.,

favors the formation of magnetite. Hydrogen diffusion through olivine has been studied at magmatic conditions experimentally (Mackwell & Kohlstedt, 1990; Mei & Kohlstedt; Demouchy & Mackwell, 2006) and in natural samples (Wang et al., 2006). To our knowledge no data are available for hydrogen diffusivity in olivine at temperatures relevant to serpentinization, i.e., ~250-350°C. As such, we extrapolated the diffusivity data of Demouchy & Mackwell (2006) to the temperatures relevant to our study. The results suggest diffusivities that are at least 12 orders of magnitude slower, at the experimental conditions of our study, than the experimental conditions at which the hydrogen diffuses out olivine in Demouchy & Mackwell (2006) (800-1300ºC) (Fig. 9).

4.2 Effect of salinity on reaction rates

The serpentinization process, even in its simplest expression (Eq. 1), represents a set of competing mechanisms operating simultaneously during the reaction. These include olivine dissolution, precipitation of serpentine and brucite, and the back reactions. The dissolution and precipitation process is not a simple bond breaking process but rather involves bond rearrangements, and several elementary reaction steps in between (Rimstidt et al. 2012). Furthermore, the serpentinization reaction rates are known to be fastest at 250- 300ºC (Martin & Fyfe, 1970; Malvoison et al., 2012; McCollom et al., 2016), whereas the equilibrium phase boundary between olivine+H_2O and serpentine + brucite occurs at higher temperature (325 to 350ºC depending on pressure). At the phase boundary, the forward and reverse reactions (dissolution of olivine to form serpentine and brucite and the reaction of serpentine + brucite to produce olivine), which doubles the number of possible elementary steps. Therefore, the rates of serpentinization are a

combination of the rate at which the olivine is dissolved into the fluid and the rate at which the aqueous species combine to form serpentine and brucite.

In this study H_2O was used as the reaction progress variable and the reaction rate was calculated from the time rate of change of H_2O content in the aqueous phase. The amount of H_2O in the aqueous phase was determined from the salinity established using the freezing point depression of the liquid remaining after the reaction had proceeded to different extents. Although this is an indirect method, the scatter in the measured rates, $1\sigma = \pm 0.08$ log units for the H_2O-NaCl-$MgCl_2$ experiments, and $1\sigma = \pm 0.1$ for the H_2O-NaCl experiments, is similar to rates determined using other methods (see for example Rimstidt et al., 2012).

During the initial stages of the reaction olivine dissolution is occurring according to:

$$Mg_2SiO_4\ (fo) + 4\ H^+ = 2\ Mg^{2+} + SiO_{2(aq)} + 2H_2O \qquad (12)$$

This reaction does not consume water so the salinity does not change. Eventually the concentration of dissolved species becomes large enough to allow chrysotile and brucite to nucleate and grow according to:

$$3\ Mg^{2+} + 2\ SiO_{2(aq)} + 5\ H_2O = Mg_3Si_2O_5(OH)_4(chr) + 6\ H^+ \qquad (13)$$

and,

$$Mg^{2+} + 2\ H_2O = Mg(OH)_2(bru) + 2\ H^+ \qquad (14)$$

These two precipitation reactions consume water and generate hydrogen ions that react with more forsterite by reaction (12) to produce more solution species. Soon after the precipitation reactions commence, the rate of production of solution species by reaction (12) is balanced by their rate of consumption by reactions (13) and (14) so the overall

process reaches a near steady state and equation (4) becomes valid. Even though reactions (13 and (14) are ongoing and H_2O is being consumed, a change in the salinity will not be obvious until it has changed by an amount required to decrease the FPD by at least 0.1 degree Celsius.

The most notable result of this study is the dramatic effect of water activity (a_{H2O}) on the reaction rate. The reaction rate is controlled by two major factors: (1) the rate of decomposition of the activated complex for the rate determining step as defined by a rate constant (k) and, (2) the driving force for the reaction as expressed by the activity of key reactants (a_i), in this case water, raised to a reaction order (n).

$$\frac{d\xi}{dt} = k a_w^n \tag{15}$$

The value of n found in this study is on the order of 120±5, which is extraordinarily large. Although the reaction order is often interpreted to indicate the number of molecules of reactant that participate in the activated complex for the rate-determining step, that interpretation is clearly incorrect for this case so a more nuanced explanation is needed. Olsen et al. (2015) showed that at low temperatures the reaction order for water involved in forsterite dissolution is 3.26 and it would not be surprising to find similar values for the water reaction order for chrysotile and brucite precipitation. However, these reaction order values are much smaller than the one found in this study so there must be other effects. One important difference between this study and Olsen et al. (2015) is that at the temperature of that study (25°C) forsterite is not thermodynamically stable so there is no possibility of forsterite precipitation. That means that their observed reaction rate (r) equals the far from equilibrium forward rate (r_+). However, these experiments were

carried out at 280°C, closer to the equilibrium phase boundary (for $a_w = 1$) that Eq. (15) requires a second term to account for the rate of re-precipitation of magnesium and silica onto the forsterite. At equilibrium the rate of this back reaction must equal the rate of the forward reaction and if the reaction processes remain the same as at equilibrium the rate equation can be rewritten in terms of the chemical potential driving the reaction (see for example supplemental information in Liu et al., 2016).

$$\frac{r}{r_+} = \frac{r}{k_+ a_w} = 1 - e^{\frac{\Delta \mu_r}{RT}} \quad (16)$$

Figure 10 shows the chemical potential for reaction (1) (calculated using SUPCRT92, Johnson et al., 1992) contoured in water activity. Figure 11 shows how this change in chemical potential affects the reaction rate. These experiments were conducted for conditions where the relatively flat far from equilibrium curve transitions into the relatively steep near equilibrium part of the curve. Thus, the dramatic effect of H_2O reactivity on the observed rates appears to be the result of a convolution of the reaction order of the far from equilibrium forsterite dissolution rate, Eq. (15), and the effect of water activity on the decreasing thermodynamic driving force, equation (16).

Another strong effect in reaction rates observed in our experiments is related to the initial composition of the fluids. The reaction rates appear to slow down as more $MgCl_2$ is increased in the initial fluid. One of the probable reasons behind this could be that the more Mg^{2+} in the fluid can drive Eq. (12) in the opposite direction increasing the back reaction, hence slowing the serpentinization reaction.

4.3 Implications

The olivine micro-reactors experiments revealed that the serpentinization rates are sensitive to the salinity of the reacting fluid and decrease rapidly with increasing salinity. However, in natural systems where ultramafic rocks are exposed to aqueous fluids, like abyssal peridotites, ophiolites and orogenic peridotites, the rocks exhibit high degrees of serpentinization (~40 to 100%) (Alt et al., 2013 and reference within; Andreani et al., 2007, 2013; Bach et al., 2004, 2006; Beard et al., 2009; Cannat et al., 1992, 2010; Klein et al., 2009). Only few examples have been found so far in which the peridotites are not heavily serpentinized (Craddock et al., 2013).

The effect of salinity on reaction rates suggests that serpentinization during seawater infiltration into the oceanic lithosphere needs a constant influx of "fresh" seawater in order to keep the fluid with low salinity to avoid the reaction to stall. If there are no other efficient mechanisms that would enhance fluid circulation, the H_2O in the seawater will be consumed by the serpentinization reaction until the salinity of the fluid is high enough for the kinetic effect to slow the reaction to near zero.

These slow rates in the serpentinization reaction will be expected on Earth in places where high salinity brines can interact with mantle rocks like in continental collisions, deep subduction zones, or in continental rifting. Moreover this effect can be significant in Mars and other planetary bodies where high salinity brines are thought to interact with ultramafic minerals (Martinez and Renno, 2013; McEwen et al, 2011; Knauth and Burt, 2002; Zolensky et al., 1999; Smith et al., 2009). The synthetic fluid inclusion micro-batch reactor technique for measuring mineral hydration rates described in this paper will provide the kinetics data that are needed to model these coupled processes.

5. Conclusions

In this study we developed a new experimental approach that allows an *in situ* monitoring of reaction progress of the hydration of olivine using synthetic fluid inclusions as micro-reactors. As soon as reaction was observed by the precipitation of serpentine and brucite, the salinity inside the SFI increased. The initial rate method was applied to determine rates at which H_2O was consumed by the reaction: olivine + water = serpentine + brucite. Different initial concentrations (1, 3.5, 6 and 10 wt.%) and compositions (NaCl-$MgCl_2$-H_2O, NaCl-H_2O and $MgCl_2$-H_2O) and rates were determined from each experiment. Reaction products can be analyzed with several microanalytical techniques (Raman, FIB SEM, TOF SIMS, TEM). The olivine micro-reactors experiments revealed that the serpentinization rates are strongly sensitive to the salinity and composition of the reacting fluid and decrease rapidly with increasing salinity. Increasing salinity decreases the activity of water enough for the chemical potential driving the reaction to decrease, almost stalling the reaction with salinities as high as 10wt.%. Mg^{2+} in the initial fluid.

Acknowledgements

The authors thank Charles Farley and Hanna Brooks for assistance with the Raman analyses; Sarah Ulrich, Chris Winkler, Rui Serra Meia, Jay Tuggle, for their support with TEM and FIB SEM. Special thanks to the PhD committee members Bob Tracy, Mark Caddick, Frieder Klein, Bob Lowell and Jim Beard for insights concerning the world of petrology, geochemistry and serpentinization. HML acknowledge support from the National Science Foundation under grant OCE-1459433. Consejo Nacional de Ciencia y Tecnología (CONACyT) and the Virginia Tech Geosciences Department and Virginia Tech Graduate School provided partial funding to HML during this study.

Appendix A

As the serpentinization reaction progresses in the closed system represented by the synthetic fluid inclusion (SFI) in olivine, H_2O contained in the aqueous solution is consumed to form the hydrous minerals, whereas the mass of solutes in the aqueous solution ($NaCl \pm MgCl_2$) is assumed to remain constant. The concentration of NaCl likely does remain constant, as Na is not incorporated easily into any of the solid phases that form during the reaction. Other cations, especially Mg, Fe and Si, will be added to or removed from the aqueous solution as the reaction progresses maintaining a charge balance with Cl^-. We assume that the Mg concentration changes little from that in the original starting fluid for the H_2O-$MgCl_2$ and the H_2O-NaCl-$MgCl_2$ starting compositions, and that concentrations of Si and Fe in solution never exceed a few hundreds of ppm. The triple point of pure H_2O occurs at 0.01°C and 0.006 bars, where liquid H_2O, vapor H_2O, and solid H_2O (in this case, the Ice I polymorph) occur in equilibrium. As salt is added to H_2O, the triple point migrates to lower temperature, and this effect is referred to as the freezing point depression (FPD) of the solution. FPD is a colligative property that depends only on the ratio of the number of moles of the solute (NaCl-$MgCl_2$ in our experiments) to that of the solvent H_2O. Thus, as H_2O is transferred from the aqueous solution into the forming hydrous phases, the ratio of moles of solute to moles of H_2O increases, and the temperature of the triple point decreases. The relationship between the salinity (moles of solute in the solution) and FPD has been determined for the ternary system H_2O-NaCl-$MgCl_2$ (Bodnar, 1993; Dubois and Marignac, 1997).

In our experimental method, we quantify the rates of serpentinization based on the amount of water removed from the aqueous solution and incorporated into hydrous phases. We use the freezing point depression (FPD) as a proxy for the amount of water removed from solution, and the sensitivity (precision) of our FPD measurement is ±0.1°C. However, some amount of H_2O must be removed from the solution and incorporated into hydrous phases before the salinity is increased by an amount sufficient to produce a 0.1 degree Celsius lowering of the FPD. The actual amount of H_2O that must be removed from solution to produce a 0.1 degree Celsius lowering of the FPD is also a function of the starting salinity (Figure Appendix A). Thus, if the initial salinity is 1 wt.% NaCl (FPD=-0.6°C), ~17 percent of the H_2O in the initial fluid must be consumed by hydration reactions to drive the FPD lower by 0.1 degree Celsius to -0.7°C (corresponding to a salinity of ~1.2 wt.% NaCl). However, the same 0.1 degree Celsius lowering of the FPD for a starting salinity of 10 wt.% NaCl requires consumption of only 1.1% of the initial H_2O, as the FPD is lowered from -6.6°C (10 wt.% NaCl) to -6.7°C (10.1 wt.% NaCl). Thus, until a sufficient amount of reaction has occurred to consume enough H_2O to lower the FPD by ≥0.1 degree Celsius, we would not know *a priori* that the reaction has started and, depending on the starting salinity, the amount of H_2O consumed (and, therefore, the amount of reaction) could vary from ~1 to 20 percent of the initial H_2O.

To calculate the mass of H_2O consumed by the serpentinization reaction as a function of the FPD, we constructed a simple mass balance model that relates the mass of H_2O in moles removed from the aqueous fluid during the reaction to the FPD. In all of our calculations we assumed a hypothetical spherical fluid inclusion 10 μm in diameter

(average size of the SFI in our experiments). The density of the aqueous solution in the SFI was calculated using the HOKIEFLINCS H2O_NaCl program (Steele-MacInnis et al., 2012) and assuming that the system H_2O-NaCl provides a reasonable approximation for the fluids in the SFI. Accordingly, the densities at 600°C and 5.5 kbar for salinities of 1, 3.5, 6, and 10 wt.% NaCl are ~0.840, ~0.870, ~0.880 and ~0.9 g/cm^3, respectively. Using these densities, the mass of the solution (H_2O and NaCl) contained in a 10 µm diameter spherical inclusion with a volume of 5.24×10^{-10} cm^3 was calculated, and the amounts salt and H_2O were obtained from the total mass of solution and the known concentration of salt obtained from the FPD measurement.

The mass of H_2O (g) contained in the reference 10 µm diameter SFI was calculated for 0.1 degrees Celsius increments of FPD as follows. The total mass of solution in the SFI is given by:

$$M_{SFI} = V_{SFI} \times \rho_{SFI} \quad (1)$$

where V_{SFI} is the volume of the SFI (= 5.24×10^{-10} cm^3) and ρ_{SFI} is the density of the solution in the SFI (in g/cm^3 as described above). The masses of NaCl and H_2O in the SFI are given by:

$$M_{NaCl} = X_{NaCl} \times M_{SFI} \quad (2)$$

$$M_{H_2O} = (1 - X_{NaCl}) \times M_{SFI} \quad (3)$$

where M_{NaCl} and M_{H_2O} are the masses of NaCl and H_2O, respectively, in the SFI in grams, and X_{NaCl} is the mass fraction of NaCl (= wt.% NaCl/100) in the solution.

$$M_{H_2O} = \frac{M_{NaCl} - (X_{NaCl} * M_{NaCl})}{X_{NaCl}} \quad (4)$$

. where M_w is the mass of H_2O (g), M_{NaCl} is the mass of NaCl (g) and X_{NaCl} is salinity of the fluid given as a fraction of NaCl.

The amount of H_2O consumed by the reaction could then be estimated from the measured FPD as follows. First, the mass of H_2O in the SFI corresponding to the initial salinity and measured FPD is calculated according to equation (4). Then, the amount of H_2O in the SFI after some amount of reaction has occurred to lower the FPD by some measureable amount is calculated. The loss at every change of salinity ($M_{w\ loss}$) was then calculated:

$$M_{w\ loss} = M_{w,0} - M_w \tag{5}$$

where, $M_{w,0}$ is the mass of H_2O in grams at t = 0, and M_w is the mass of H_2O obtained by Eq. (1). From this the number of moles of H_2O consumed $n_w$was calculated:

$$n_w = M_{w\ loss}\ (g) \times \frac{1\ mol}{18\ g} \tag{6}$$

For every initial salinity (1, 3.5, 6 and 10 wt.%) the number of moles of H_2O consumed n_w was fit as polynomial expressions of salinity to determine the number of moles of H_2O consumed as a function of the salinity of the SFI.

Appendix A Figure

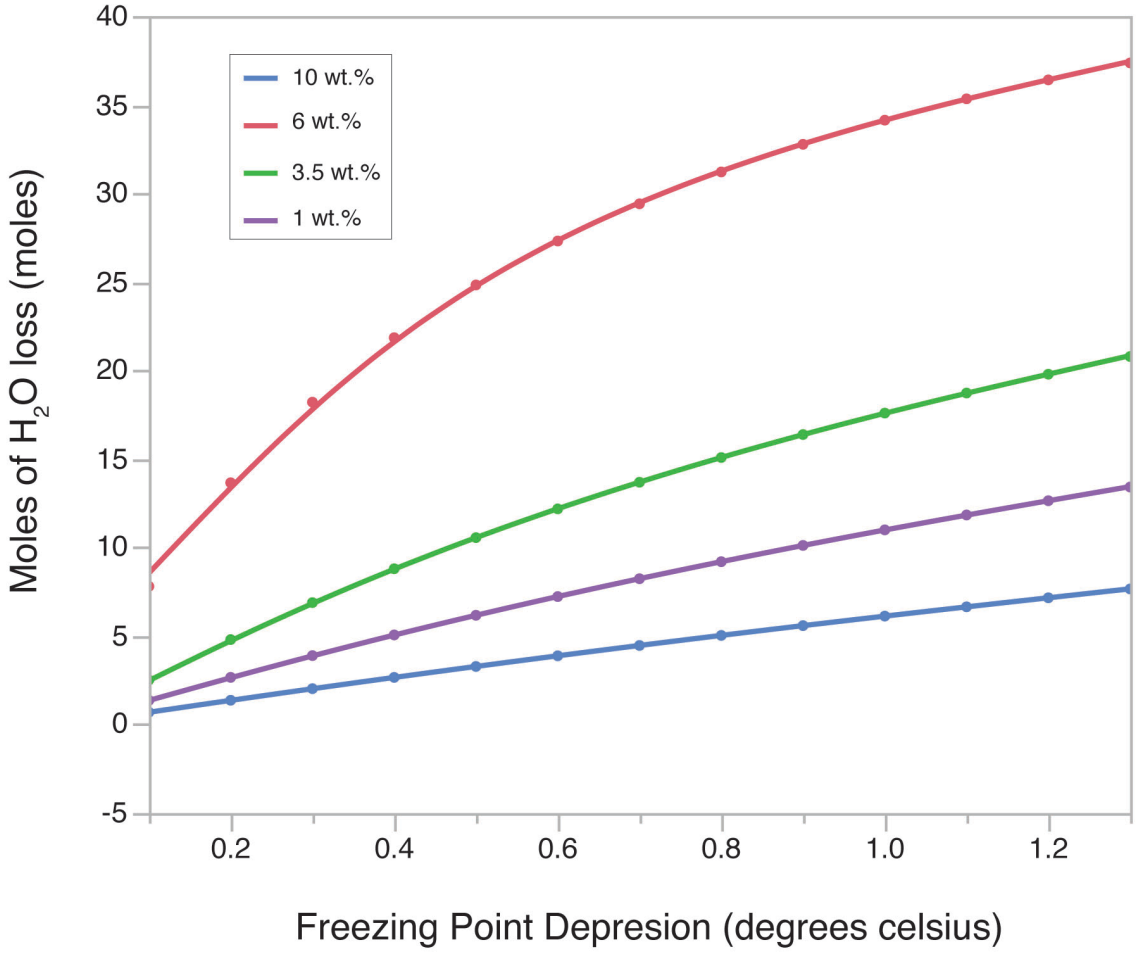

Appendix A Figure. Amount of moles of H_2O needed to decrease the freezing point depression (FDP) of a solution as a function of the initial salinity of the solution. In a solution with a total mass of 1 kg with1 wt.% of NaCl, 7.8 moles of H2O need to be consumed to decrease in 0.1 degrees Celsius the FPD, if the initial salinity is 3.5 wt.%, 2.5 moles of H_2O need to be consumed to decrease in 0.1 degrees Celsius the FPD.

References

Abrajano, T. A., Sturchio, N. C., Bohlke, J. K., Lyon, G. L., Poreda, R. J., & Stevens, C. M. (1988) Methane-hydrogen gas seeps, Zambales Ophiolite, Philippines: Deep or shallow origin?. *Chemical Geology*, ***71*** (1), 211-222.

Allen, D. E., & Seyfried, W. E. (2003) Compositional controls on vent fluids from ultramafic-hosted hydrothermal systems at mid-ocean ridges: An experimental study at 400 C, 500 bars. *Geochimica et Cosmochimica Acta, **67*** (8), 1531-1542.

Allen, D. E., & Seyfried, W. E. (2004) Serpentinization and heat generation: constraints from Lost City and Rainbow hydrothermal systems. *Geochimica et Cosmochimica Acta, **68*** (6), 1347-1354.

Alt, J. C., Schwarzenbach, E. M., Früh-Green, G. L., Shanks III, W. C., Bernasconi, S. M., Garrido, C. J., Crispini, L., Gaggero, L., Padrón-Navarta, J. A., Marchesi, C. (2013) The role of serpentinites in cycling of carbon and sulfur: Seafloor serpentinization and subduction metamorphism. *Lithos **178***, 40-54.

Andreani, M., Daniel, I., & Pollet-Villard, M. (2013) Aluminum speeds up the hydrothermal alteration of olivine. *American Mineralogist, **98*** (10), 1738-1744.

Andreani, M., Mével, C., Boullier, A. M., & Escartin, J. (2007) Dynamic control on serpentine crystallization in veins: constraints on hydration processes in oceanic peridotites. *Geochemistry, Geophysics, Geosystems*,***8*** (2).

Arredondo, E. H., & Rossman, G. R. (2002) Feasibility of determining the quantitative OH content of garnets with Raman spectroscopy. *American Mineralogist, **87*** (2-3), 307-311.

Auzende, A. L., Daniel, I., Reynard, B., Lemaire, C., & Guyot, F. (2004) High-pressure behaviour of serpentine minerals: a Raman spectroscopic study. *Physics and Chemistry of Minerals, **31*** (5), 269-277.

Bach, W., Banerjee, N. R., Dick, H. J. B., Baker, E. T. (2002) Discovery of ancient and active hydrothermal systems along the ultra-slow spreading Southwest Indian Ridge 10° -16° E. *Geochemistry, Geophysics, Geosystems, **3*** (7), 1-14..

Bach, W., Garrido, C. J., Paulick, H., Harvey, J., Rosner, M. (2004) Seawater-peridotite interactions: First insights form ODP Leg 209, MAR 15°N. G*eochemistry, Geophysics, Geosystems, **5** (9).*

Bach, W., Paulick, H., Garrido, C.J., Ildefonse, B., Meurer, W.P., Humphris, S.E. (2006) Unraveling the sequence of serpentinization reactions: petrography, mineral chemistry, and petrophysics of serpentinites from MAR 15°N (ODP Leg 209, Site 1274). *Geophysical research letters, **33*** (13).

Bach, W., Klein, F. (2009) The petrology of seafloor rodingites: Insights from geochemical reaction path modeling. *Lithos, **112***, 103-117.

Bali, E., Audétat, A., & Keppler, H. (2013) Water and hydrogen are immiscible in Earth/'s mantle. *Nature, **495*** (7440), 220-222.

Bard, D., Yarwood, J., & Tylee, B. (1997) Asbestos fibre identification by Raman microspectroscopy. *Journal of Raman spectroscopy*, ***28*** (10), 803-809.

Barnes, I., O'Neil, J.R., (1978) Present day serpentinization in New Caledonia, Oman and Yugoslavia. *Geochimica et Cosmochimica Acta, **42** (1), 144-145.*

Barnes, I., LaMarceh, V.C., Himmelberg, G., (1967) Geochemical evidence of present-day serpentinization. *Science, **156***, 830-832.

Beard, James S., B. Ronald Frost, Patricia Fryer, Andrew McCaig, Roger Searle, Benoit Ildefonse, Pavel Zinin, and Shiv K. Sharma. (2009) Onset and progression of serpentinization and magnetite formation in olivine-rich troctolite from IODP Hole U1309D. *Journal of Petrology*, egp004.

Becker, S. P., Eichhubl, P., Laubach, S. E., Reed, R. M., Lander, R. H., & Bodnar, R. J. (2010) A 48 my history of fracture opening, temperature, and fluid pressure: Cretaceous Travis Peak Formation, East Texas basin. *Geological Society of America Bulletin, **122*** (7-8), 1081-1093.

Berkesi, M., Guzmics, T., Szabó, C., Dubessy, J., Bodnar, R. J., Hidas, K., & Ratter, K. (2012) The role of CO_2 -rich fluids in trace element transport and metasomatism in the lithospheric mantle beneath the Central Pannonian Basin, Hungary, based on fluid inclusions in mantle xenoliths. *Earth and Planetary Science Letters, **331***, 8-20.

Bischoff, J. L., & Pitzer, K. S. (1985) Phase relations and adiabats in boiling seafloor geothermal systems. *Earth and Planetary Science Letters, **75*** (4), 327-338.

Blackman, D. K., Canales, J. P., & Harding, A. (2009) Geophysical signatures of oceanic core complexes. *Geophysical Journal International*, ***178*** (2), 593-613.

Bodnar, R. J., Burnham, C. W., & Sterner, S. M. (1985) Synthetic fluid inclusions in natural quartz. III. Determination of phase equilibrium properties in the system H_2O-NaCl to 1000° C and 1500 bars. *Geochimica et Cosmochimica Acta, **49*** (9), 1861-1873.

Bodnar, R. J., Azbej, T., Becker, S. P., Cannatelli, C., Fall, A., & Severs, M. J. (2013) Whole Earth geohydrologic cycle, from the clouds to the core: The distribution of water in the dynamic Earth system. *Geological Society of America Special Papers*, **500**, 431-461.

Boschi, C., Früh-Green, G. L., Delacour, A., Karson, J. A., & Kelley, D. S. (2006) Mass transfer and fluid flow during detachment faulting and development of an oceanic core complex, Atlantis Massif (MAR 30 N). *Geochemistry, Geophysics, Geosystems*, ***7*** (1).

Boschi, C., Dini, A., Früh-Green, G. L., Kelley, D. S. (2008) Isotopic and element exchange during serpentinization and metasomatism at the Atlantis Massif (MAR 30°N): Insights from B and Sr isotope data. *Geochimica et Cosmochimica Acta, **72** (7), 1801-1823*.

Boschi, C., Bonatti, E., Ligi, M., Brunelli, D., Cipriani, A., Dallai, L., D'Orazio, M., Früh-Green, G. L., Tonarini, S., Barnes, J. D., Bedini, R. M. (2013) Serpentinization of mantle peridotites along an uplifted lithospheric section, Mid Atlantic Ridge at 11° N. *Lithos, **178***, 3-23.

Bowen, N. L., & Tuttle, O. F. (1949) The system MgO—SiO2—H2O.*Geological Society of America Bulletin*, ***60*** (3), 439-460.

Brazelton, W.J., Schrenk, M.O., Kelley, D.S., Baross, J.A., (2006) Methane- and sulfur-metabolizing microbial communities dominate the Lost City hydrothermal field ecosystem. A*pplied and Environmental Microbiology, **72** (9), 6257-6270.*

Cadore, E. (1995) Mécanismes de dissolution du quartz dans les solutions naturelles. Etude expérimentale et modélisation (Doctoral dissertation).

Calas, G. (2013) Versatile serpentine. *Elements,* ***9*** (2), 83-83.
Casey, W. H., & Westrich, H. R. (1992) Control of dissolution rates of orthosilicate minerals by divalent metal–oxygen bonds. *Nature,* ***355*** (6356), 157-159.
Cannat, M. (1993) Emplacement of mantle rocks in the sea-floor at mid-ocean ridges. *Journal of Geophysical Research: Solid Earth,* ***98*** *(B3), 4163-4172.*
Cannat, M., Bideau, D., Bougault, H. (1992) Serpentinized periodtites and gabbros in the Mid-Atlantic Ridge axial valley at 15°37'N and 16°52'N. *Earth Planetary Science Letters.* ***109***, 87-106.
Cannat, M., Fontaine, F., Escartin, J. (2010) Serpentinization and associated hydrogen and methane fluxes at slow spreading ridges, in: Rona, P.A., Devey, C.W., Dyment, J., Murton, B.J. (Eds.), Diversity of hydrothermal systems on slow spreading ocean ridges. American Geophysical Union, Washington.
Carlson, R. L. (2001) The abundance of ultramafic rocks in Atlantic Ocean crust. *Geophysical Journal International,* ***144*** (1), 37-48.
Charlou, J. L., Fouquet, Y., Bougault, H., Donval, J. P., Etoubleau, J., Jean-Baptiste, P., & Rona, P. A. (1998) Intense CH_4 plumes generated by serpentinization of ultramafic rocks at the intersection of the 15° 20′ N fracture zone and the Mid-Atlantic Ridge. *Geochimica et Cosmochimica Acta*, ***62*** (13), 2323-2333.
Charlou, J. L., Donval, J. P., Fouquet, Y., Jean-Baptiste, P., & Holm, N. (2002) Geochemistry of high H_2 and CH_4 vent fluids issuing from ultramafic rocks at the Rainbow hydrothermal field (36° 14′ N, MAR). *Chemical Geology*, ***191*** (4), 345-359.
Chernak, L. J., & Hirth, G. (2010) Deformation of antigorite serpentinite at high temperature and pressure. *Earth and Planetary Science Letters*, ***296*** (1), 23-33.
Chernosky, J. V. (1973) The stability of chrysotile, $Mg_3Si_2O_5(OH)_4$, and the free energy of formation of talc, $Mg_3Si_4O_{10}(OH)_2$. In *Geological Society of America Annual Meeting,* Program and Abstracts.
Chou, H., Ismach, A., Ghosh, R., Ruoff, R. S., & Dolocan, A. (2015) Revealing the planar chemistry of two-dimensional heterostructures at the atomic level. *Nature communications*, ***6***.
Coleman, R. G. (1967) Low-temperature reaction zones and alpine ultramafic rocks of California, Oregon and Washington. *U.S. Geological Survey Bulletin* ***1247***, 1-49.
Colleary, C., Dolocan, A., Gardner, J., Singh, S., Wuttke, M., Rabenstein, R., Habersetzer, J., Schaal, S., Feseha, M., Clemens, M. and Jacobs, B.F. (2015) Chemical, experimental, and morphological evidence for diagenetically altered melanin in exceptionally preserved fossils. *Proceedings of the National Academy of Sciences,* ***112*** (41), 12592-12597.
Connolly, J. A. D. (2005) Computation of phase equilibria by linear programming: A tool for geodynamic modeling and its application to subduction zone decarbonation. *Earth and Planetary Science Letters* ***236***, 524-541.
Craddock, P. R., Warren, J. M., & Dauphas, N. (2013) Abyssal peridotites reveal the near-chondritic Fe isotopic composition of the Earth. *Earth and Planetary Science Letters,* ***365***, 63-76.
Deer, W. A., Howie, R. A., & Zussman, J. (Eds.). (2009) Layered silicates excluding micas and clay minerals. Geological Society of London.

Delaney, J. R., Mogk, D. W., & Mottl, M. (1987) Quartz-cemented breccias from the Mid-Atlantic Ridge: Samples of a high-salinity hydrothermal upflow zone. *Journal of Geophysical Research: Solid Earth,* ***92*** (B9), 9175-9192.

Deschamps, F., Guillot, S., Godard, M., Andreani, M., & Hattori, K. (2011) Serpentinites act as sponges for fluid-mobile elements in abyssal and subduction zone environments. *Terra Nova*, ***23*** (3), 171-178.

Deschamps, F., Godard, M., Guillot, S., & Hattori, K. (2013) Geochemistry of subduction zone serpentinites: A review. *Lithos*, ***178***, 96-127.

Dick, H. J. B., Lin, J., Schouten, H. (2003) An ultraslow-spreading class of ocean ridge. *Nature,* ***426***, 405- 412.

Dubois, M., & Marignac, C. (1997) The H_2O-NaCl-$MgCl_2$ ternary phase diagram with special application to fluid inclusion studies. *Economic Geology*, ***92*** (1), 114-119.

Eckstrand, O.R. (1975) The Dumont Serpentinite: A model for control of nickeliferous opaque mineral assemblages by alteration reactions in ultramafic rocks. *Economic Geology,* ***70***, 183-201.

Esposito, R., Hunter, J., Schiffbauer, J. D., & Bodnar, R. J. (2014) An assessment of the reliability of melt inclusions as recorders of the pre-eruptive volatile content of magmas. *American Mineralogist,* ***99*** (5-6), 976-998.

Evans, B. W., Johannes, W., Oterdoom, H., & Trommsdorff, V. (1976) Stability of chrysotile and antigorite in the serpentinite multisystem. Schweiz. *Mineral. Petrogr. Mitt,* ***56***, 79-93.

Evans, B. W., Kuehner, S. M., & Chopelas, A. (2009) Magnetite-free, yellow lizardite serpentinization of olivine websterite, Canyon Mountain complex, NE Oregon. *American Mineralogist,* ***94*** (11-12), 1731-1734.

Evans, B. W. (2008) Control of the products of serpentinization by the Fe2+ Mg− 1 exchange potential of olivine and orthopyroxene. *Journal of Petrology*, ***49*** (10), 1873-1887.

Evans, B. W., Hattori, K., & Baronnet, A. (2013) Serpentinite: What, Why, Where?. *Elements*, ***9*** (2), 99-106.

Evans, B.W. (1977) Metamorphism of alpine peridotite and serpentinite. *Annual Reviews Earth and Planetary Sciences,* ***5***, 397-447.

Farough, A., Moore, D. E., Lockner, D. A., & Lowell, R. P. (2016) Evolution of fracture permeability of ultramafic rocks undergoing serpentinization at hydrothermal conditions: An experimental study. *Geochemistry, Geophysics, Geosystems.*

Frost, B.R. (1975) Contact metamorphism of serpentinite, chloritic blackwall and rodingite at Paddy-go-easy Pass, Central Cascades, Washington. *Journal of Petrology,* ***16***, 272-313.

Frost, B.R. (1985) On the stability of sulfides, oxides, and native metals in serpentinite. *Journal of Petrology,* ***26***, 31-63.

Frost, B. R., & Beard, J. S. (2007) On silica activity and serpentinization. *Journal of Petrology*, ***48*** (7), 1351-1368.

Frost, B. R., Beard, J. S., McCaig, A., & Condliffe, E. (2008) The formation of micro-rodingites from IODP Hole U1309D: key to understanding the process of serpentinization. *Journal of Petrology,* ***49*** (9), 1579-1588.

Früh-Green, G. L., Connolly, J. A., Plas, A., Kelley, D. S., Grobéty, B. (2004) Serpentinization of oceanic peridotites: Implications for geochemical cycles and

biological activity. In*: the subseafloor biospere at Mid-Ocean Ridges*. American Geophysical Union, Washington D.C. 119-136

German, C. R., Lin, J., & Parson, L. M. (2004) Mid-ocean ridges: hydrothermal interactions between the lithosphere and oceans. Washington DC. *American Geophysical Union Geophysical Monograph Series, **148***.

Godard, M., Luquot, L., Andreani, M., & Gouze, P. (2013) Incipient hydration of mantle lithosphere at ridges: A reactive-percolation experiment. *Earth and Planetary Science Letters, **371**,* 92-102

Groppo, C., Rinaudo, C., Cairo, S., Gastaldi, D., & Compagnoni, R. (2006) Micro-Raman spectroscopy for a quick and reliable identification of serpentine minerals from ultramafics. *European Journal of Mineralogy, **18*** (3), 319-329.

Hattori, K. H., & Guillot, S. (2003) Volcanic fronts form as a consequence of serpentinite dehydration in the forearc mantle wedge. *Geology, **31*** (6), 525-528.

Hidas, K., Guzmics, T., Szabó, C., Kovács, I., Bodnar, R. J., Zajacz, Z., Nédli Zs, Vaccari L & Perucchi A. (2010) Coexisting silicate melt inclusions and H_2O-bearing, CO_2-rich fluid inclusions in mantle peridotite xenoliths from the Carpathian–Pannonian region (central Hungary). *Chemical Geology, **274*** (1), 1-18.

Hilairet, N., Reynard, B., Wang, Y., Daniel, I., Merkel, S., Nishiyama, N., & Petitgirard, S. (2007) High-pressure creep of serpentine, interseismic deformation, and initiation of subduction. *Science*, ***318*** (5858), 1910-1913.

Hyndman, R. D., & Peacock, S. M. (2003) Serpentinization of the forearc mantle. *Earth and Planetary Science Letters*, ***212*** (3), 417-432.

Janecky, D. R., & Seyfried, W. E. (1986) Hydrothermal serpentinization of peridotite within the oceanic crust: experimental investigations of mineralogy and major element chemistry. *Geochimica et Cosmochimica Acta, **50*** (7), 1357-1378. Chicago

Johannes, W. (1969) An experimental investigation of the system MgO-SiO_2-H_2O-CO_2. *American Journal of Science, **267*** (9), 1083-1104.

Johnson, E. L., & Jenkins, D. M. (1991) Synthetic H_2O - CO_2 fluid inclusions in spontaneously nucleated forsterite, enstatite, and diopside hosts: The method and applications. *Geochimica et Cosmochimica Acta, **55*** (4), 1031-1040.

Johnson, J. W., Oelkers, E. H., & Helgeson, H. C. (1992) SUPCRT92: A software package for calculating the standard molal thermodynamic properties of minerals, gases, aqueous species, and reactions from 1 to 5000 bar and 0 to 1000 C. *Computers & Geosciences, **18** (7*), 899-947.

Kelemen, P. B., Matter, J. (2008) In situ carbonation of peridotite for CO_2 storage. *Proceedings of the National Academy of Sciences, 105(45), 17295-17300.*

Kelemen, P. B., & Hirth, G. (2012) Reaction-driven cracking during retrograde metamorphism: Olivine hydration and carbonation. *Earth and Planetary Science Letters*, ***345***, 81-89.

Kelley, D. S., Robinson, P. T., & Malpas, J. G. (1992) Processes of brine generation and circulation in the oceanic crust: Fluid inclusion evidence from the Troodos Ophiolite, Cyprus. *Journal of Geophysical Research: Solid Earth (1978–2012), **97*** (B6), 9307-9322.

Kelley, D. S. (1996) Methane-rich fluids in the oceanic crust. *Journal of Geophysical Research: Solid Earth (1978–2012)*, ***101*** (B2), 2943-2962.

Kelley, S. D., Karson, J. A., Blackman, D. K., Früh-Green, G. L., Butterfield, D. A., Lilley, D. M., Olson, E. J., Schrenk, M. O., Roell, K. K., Lebon, G. T., Rivizzigno, P., and the AT3-60 Shipboard Party (2001) An off-axis hydrothermal vent field near the Mid-Atlantic Ridge at 30° N. *Nature, **412***, 145-149.

Kelley, D.S., Karson, J.A., Früh-Green, G.L., Yoerger, D.R., Shank, T.M., Butterfield, D.A., Hayes, J.M., Schrenk, M.O., Olson, E.J., Proskurowski, G., Jakuba, M., Bradley, A., Larson, B., Ludwig, K.A., Glickson, D., Buckman, K., Bradley, A.S., Brazelton, W.J., Roe, K., Elend, M.J., Delacour, A., Bernasconi, S.M., Lilley, D.M., Baross, J.A., Summons, R.E., Sylva, S.P. (2005) A serpentinite-hosted ecosystem: The lost city hydrothermal field. *Science, **307***, 1428-1434.

Kitahara, S., & Kennedy, G. C. (1967) The calculated equilibrium curves for some reactions in the system MgO-SiO_2-H_2O at pressures up to 30 kilobars. *American Journal of Science, **265*** (3), 211-217.

Klein, F., Grozeva, N. G., Seewald, J. S., McCollom, T. M., Humphris, S. E., Moskowitz, Berquó, TS., & Kahl, W. A. (2015) Fluids in the Crust. Experimental constraints on fluid-rock reactions during incipient serpentinization of harzburgite. *American Mineralogist, **100*** (4), 991-1002.

Klein, F., Bach, W., & McCollom, T. M. (2013) Compositional controls on hydrogen generation during serpentinization of ultramafic rocks. *Lithos*, ***178***, 55-69.

Klein, F., Bach, W. (2009a) Fe-Ni-Co-O-S Phase Relations in Peridotite-Seawater Interactions. *Journal of Petrology, **50***, 37-59.

Klein F., Bach W., Jo¨ns N., McCollom T. M., Moskovitz B. and Berquo T. (2009b) Iron partitioning and hydrogen generation during serpentinization of abyssal peridotites from 15ºN on the Mid-Atlantic Ridge. *Geochimica et Cosmochimica. Acta **73***, 6868–6893

Kloprogge, J., Frost, R. L., Rintoul, L. (1999) Single crystal Raman microscopic study of the asbestos mineral chrysotile. *Physical Chemistry Chemical Physics*, ***1*** (10), 2559-2564.

Knauth, L. P., and D. M. Burt (2002) Eutectic brines on Mars: Origin and possible relation to young seepage features, I*carus*, ***158*** (1), 267–271.

Kodolányi, J., & Pettke, T. (2011) Loss of trace elements from serpentinites during fluid-assisted transformation of chrysotile to antigorite—an example from Guatemala. *Chemical Geology*, ***284*** (3), 351-362.

Kolesov, B. A., & Geiger, C. A. (2005) The vibrational spectrum of synthetic hydrogrossular (katoite) $Ca_3Al_2(O_4H_4)_3$: A low-temperature IR and Raman spectroscopic study. *American Mineralogist, **90*** (8-9), 1335-1341.

Kontak, D. J. (2004) Analysis of evaporate mounds as a complement to fluid-inclusion thermometric data: case studies from granitic environments in Nova Scotia and Peru. *The Canadian Mineralogist, **42*** (5), 1315-1329.

Kuebler, K. E., Jolliff, B. L., Wang, A., & Haskin, L. A. (2006) Extracting olivine (Fo–Fa) compositions from Raman spectral peak positions. *Geochimica et Cosmochimica Acta, **70*** (24), 6201-6222.

Laidler, K. J. (1969). Theories of chemical reaction rates.

Lafay, R., Montes-Hernandez, G., Janots, E., Chiriac, R., Findling, N., & Toche, F. (2012) Mineral replacement rate of olivine by chrysotile and brucite under high alkaline conditions. *Journal of Crystal Growth, **347*** (1), 62-72.

Lewis, I. R., Chaffin, N. C., Gunter, M. E., & Griffiths, P. R. (1996) Vibrational spectroscopic studies of asbestos and comparison of suitability for remote analysis. *Spectrochimica Acta Part A: Molecular and Biomolecular Spectroscopy*, ***52*** (3), 315-328.

Li, Z. X. A., & Lee, C. T. A. (2006) Geochemical investigation of serpentinized oceanic lithospheric mantle in the Feather River Ophiolite, California: implications for the recycling rate of water by subduction. *Chemical Geology, **235*** (1), 161-185.

Lin, F., Bodnar, R. J., & Becker, S. P. (2007a) Experimental determination of the Raman CH_4 symmetric stretching (ν_1) band position from 1–650 bar and 0.3–22° C: Application to fluid inclusion studies. *Geochimica et Cosmochimica Acta, **71*** (15), 3746-3756.

Lin, F., Sum, A. K., & Bodnar, R. J. (2007b) Correlation of methane Raman ν_1 band position with fluid density and interactions at the molecular level. *Journal of Raman Spectroscopy, **38*** (11), 1510-1515.

Liu, Z., Rimstidt, J.D., Zhang, Y. and Zhu, C. (2016) A stable isotope doping method to test the range of applicability of detailed balance. *Geochemical Perspectives Letters **2***, 78-86.

Lowell, R. P., & Rona, P. A. (2002) Seafloor hydrothermal systems driven by the serpentinization of peridotite. *Geophysical Research Letters*, ***29*** (11).

Marcaillou, C., Munoz, M., Vidal, O., Parra, T., & Harfouche, M. (2011) Mineralogical evidence for H_2 degassing during serpentinization at 300° C/300bar. *Earth and Planetary Science Letters, **303*** (3), 281-290.

Mackwell, S. J., & Kohlstedt, D. L. (1990) Diffusion of hydrogen in olivine: implications for water in the mantle. *Journal of Geophysical Research: Solid Earth, **95*** (B4), 5079-5088.

Martin, B., & Fyfe, W. S. (1970) Some experimental and theoretical observations on the kinetics of hydration reactions with particular reference to serpentinization. *Chemical Geology, **6***, 185-202.

Martin, W., & Russell, M. J. (2007) On the origin of biochemistry at an alkaline hydrothermal vent. *Philosophical Transactions of the Royal Society B: Biological Sciences*, ***362*** (1486), 1887-1926.

Martin, W., Baross, J., Kelley, D., Russell, M. (2008) Hydrothermal vents and the origin of life. *Nature Reviews Microbiology **6***, 805 - 814.

Martinez, G. M., and N. O. Renno (2013) Water and brines on Mars: Current evidence and implications for MSL, *Space Science Reviews, **175** (1-4), 29-51.*

McEwen, A. S., L. Ojha, C. M. Dundas, S. S. Mattson, S. Byrne, J. J. Wray, S. C. Cull, S. L. Murchie, N. Thomas, and V. C. Gulick (2011) Seasonal flows on warm Martian slopes, *Science, **333*** (6043), 740–743.

Mei, S., & Kohlstedt, D. L. (2000) Influence of water on plastic deformation of olivine aggregates: 1. Diffusion creep regime. *Journal of Geophysical Research: Solid Earth, **105*** (B9), 21457-21469.

Merrill, G. P. (1899) A discussion on the use of the terms rock-weathering, serpentinization, and hydrometamorphism. *Geological Magazine **6***, 354-358.

McCollom, T.M. (1999) Methanogenesis as a potential source of chemical energy for primary biomass production by autotrophic organisms in hydrothermal systems on Europa. *Journal of Geophysical Research: Planets, **104** (E12), 30729-30742.*

McCollom, T. M., Seewald, J. S. (2001) A reassessment of the potential for reduction of dissolved CO_2 to hydrocarbons during serpentinization of olivine. *Geochim. Cosmochim. Acta **65***, 3769-3778.

McCollom, T. M., & Bach, W. (2009) Thermodynamic constraints on hydrogen generation during serpentinization of ultramafic rocks. *Geochimica et Cosmochimica Acta*, ***73*** (3), 856-875.

McCollom, T. M., & Seewald, J. S. (2013) Serpentinites, hydrogen, and life. *Elements*, ***9*** (2), 129-134.

McCollom, T.M., Klein, F., Robbins, M., Moskowitz, B., Berquó, T.S., Jöns, N., Bach, W. and Templeton, A (2016) Temperature trends for reaction rates, hydrogen generation, and partitioning of iron during experimental serpentinization of olivine. *Geochimica et Cosmochimica Acta, **181***, 175-200.

Miura, Y., Rucklidge, J., & Nord Jr, G. L. (1981) The occurrence of chlorine in serpentine minerals. *Contributions to Mineralogy and Petrology*, ***76*** (1), 17-23.

Miyoshi, A., Kogiso, T., Ishikawa, N., & Mibe, K. (2014) Role of silica for the progress of serpentinization reactions: Constraints from successive changes in mineralogical textures of serpentinites from Iwanaidake ultramafic body, Japan. *American Mineralogist, **99*** (5-6), 1035-1044.

Moody, J. B. (1976) Serpentinization: a review. *Lithos, **9***, 125-138.

Morrow, C. P., Olsen, A. A., & Kubicki, J. D. (2014) Quantum mechanical modeling of hydrolysis and H2O-exchange in Mg-, Ca-, and Nisilicate clusters: Implications for dissolution mechanisms of olivine minerals. *American Mineralogist, **99*** (11-12), 2303-2312.

Moctar, D. O., Boushaba, A., & Dubois, M. (2014) Serpentinization of mantle formations in the Mauritanides Belt: regions of Agane and Gouérarate (middle-western Mauritania). *Arabian Journal of Geosciences*, ***7*** (5), 1985-1992.

Rimstidt, J. D., & Newcomb, W. D. (1993) Measurement and analysis of rate data: The rate of reaction of ferric iron with pyrite. *Geochimica et Cosmochimica Acta, **57*** (9), 1919-1934.

Normand, C., Williams-Jones, A. E., Martin, R. F., & Vali, H. (2002) Hydrothermal alteration of olivine in a flow-through autoclave: Nucleation and growth of serpentine phases. *American Mineralogist, **87*** (11-12), 1699-1709.

Olsen, A. A., E. M. Hausrath, and J. D. Rimstidt (2015) Forsterite dissolution rates in Mg-sulfate-rich Mars-analog brines and implications of the aqueous history of Mars. *Journal of Geophysical Research: Planets, **120*** (3), 388-400.

Ogasawara, Y., Okamoto, A., Hirano, N., & Tsuchiya, N. (2013) Coupled reactions and silica diffusion during serpentinization. *Geochimica et Cosmochimica Acta, **119***, 212-230.

O'Hanley, D.S. (1992) Solution of the volume problem of serpentinization. *Geology, **20*,** 705-708.

O'Hanley, D.S. (1996) Serpentinites: Records of tectonic and petrological history. Oxford university press, New York, Oxford.

O'Hanley, D.S., Wicks, F.J. (1995) Conditions of formation of lizardite, chrysotile and antigorite, Cassiar, British-Colombia. *The Canadian Mineralogist,* ***33***, 753-773.

Okamoto, A., Ogasawara, Y., Ogawa, Y., & Tsuchiya, N. (2011) Progress of hydration reactions in olivine–H_2O and orthopyroxenite–H_2O systems at 250 C and vapor-saturated pressure. *Chemical geology,* ***289*** (3), 245-255.

Olsen, A.A., Hausrath, E. and Rimstidt, J.D. (2015) Forsterite dissolution rates in Mg-sulfate-rich Mars-analog brines and implications of the aqueous history of Mars. *Journal of Geophysical Research: Planets* ***120*** (3), 388-400.

Palandri, J.L., Reed, M.H. (2004) Geochemical models of metasomatism in ultramafic systems: Serpentinization, rodingitization, and sea floor carbonate chimney precipitation. *Geochim. Cosmochim. Acta,* ***68*****,** 1115 - 1133.

Plank, T., & Langmuir, C. H. (1993) Tracing trace elements from sediment input to volcanic output at subduction zones. *Nature,* ***362*** (6422), 739-743.

Plümper O., Royne A., Magraso A., Jamtveit B. (2012) The interface-scale mechanism of reaction-induced fracturing during serpentinization: *Geology,* ***40***, 1103–1106

Poty, B., Holland, H. D., & Borcsik, M. (1972) Solution-mineral equilibria in the system MgO-SiO_2-H_2O-$MgCl_2$ at 500 C and 1 kbar. *Geochimica et Cosmochimica Acta,* ***36*** (10), 1101-1113.

Poty, B., Leroy, J., & Jachimowicz, L. (1976) Un nouvel appareil pour la mesure des températures sous le microscope: l'installation de microthermométrie Chaixmeca. *Bull. Soc. Fr. Minéral. Cristallogr*, **99**, 182-186.

Proskurowski, G., Lilley, M., Seewald, J., Früh-Green, G. L., Olson, E. J., Lupton, J. E., Sylva, S. P., Kelley, D. S. (2008) Abiogenic hydrocarbon production at Lost City hydrothermal field. *Science,* ***319***, 604-607.

Rimstidt, J.D., Brantley, S.L. and Olsen, A.A. (2012) Systematic review of forsterite dissolution data. *Geochimica et Cosmochimica Acta,* ***99,*** 159-178.

Rimstidt, J.D. (2014) Geochemical Rate Models. Cambridge University Press.

Rinaudo, C., Gastaldi, D., & Belluso, E. (2003) Characterization of chrysotile, antigorite and lizardite by FT-Raman spectroscopy. *The Canadian Mineralogist*, ***41*** (4), 883-890.

Robinson, R. A., & Stokes, R. H. (2002) Electrolyte solutions. Courier Corporation.

Russell, M.J., Hall, A.J., Martin, W. (2010) Serpentinization as a source of energy at the origin of life. *Geobiology,* ***8***(5), 355-371.

Sanchez-Murillo, R., Gazel, E., Schwarzenbach, E.M., Crespo-Medina, M., Schrenk, M.O., Boll, J., Gill, B.C. (2014) Geochemical evidence for active tropical serpentinization in the Santa Elena Ophiolite, Costa Rica: An analogue of a humid early Earth? *Geochemistry, Geophysics, Geosystems,* ***15*** *(5), 1783-1800.*

Schott, J., Pokrovsky, O. S., & Oelkers, E. H. (2009) The link between mineral dissolution/precipitation kinetics and solution chemistry. *Reviews in mineralogy and geochemistry,* ***70*** (1), 207-258.

Schrenk, M.O., Kelley, D.S., Bolton, S.A., Barossa, J.A. (2004) Low archaeal diversity linked to subseafloor geochemical processes at the Lost City Hydrothermal Field, Mid-Atlantic Ridge. *Environmental Microbiology* ***6***, 1086-1095.

Schulte, M., Blake, D., Hoehler, T., & McCollom, T. (2006) Serpentinization and its implications for life on the early Earth and Mars. *Astrobiology*, ***6*** (2), 364-376.

Schwartz, S., Guillot, S., Tricart, P., Bernet, M., Jourdan, S., Dumont, T., & Montagnac, G. (2012) Source tracing of detrital serpentinite in the Oligocene molasse deposits from the western Alps (Barrême basin): implications for relief formation in the internal zone. *Geological Magazine*, ***149*** (05), 841-856.

Schwarzenbach, E.M. (2011) Serpentinization, fluids and life: Comparing carbon and sulfur cycles in modern and ancient environments, Earth Sciences. ETH Zurich, Thesis No. 19588, Zurich, p. 240.

Schwarzenbach, E. M., Caddick, M. J., Beard, J. S., & Bodnar, R. J. (2016) Serpentinization, element transfer, and the progressive development of zoning in veins: evidence from a partially serpentinized harzburgite. *Contributions to Mineralogy and Petrology, **171*** (1), 1-22.

Schwarzenbach, E. M., Früh-Green, G. L., Bernasconi, S. M., Alt, J. C., Plas, A. (2013a) Serpentinization and the incorporation of carbon: A study of two ancient peridotite-hosted hydrothermal systems. *Chemical Geology, **351***, 115-133.

Schwarzenbach, E. M., Früh-Green, G. L., Bernasconi, S. M., Alt, J. C., Shanks III, W. C., Gaggero, L., Crispini, L. (2012) Sulfur geochemistry of peridotite-hosted hydrothermal systems: Comparing the Ligurian ophiolites with oceanic serpentinites. *Geochimica et Cosmochimica Acta, **91***, 283-305.

Schwarzenbach, E. M., Lang, S. Q., Früh-Green, G. L., Lilley, M. D., Bernasconi, S. M., Méhay, S. (2013b) Sources and cycling of carbon in continental, serpentinite-hosted alkaline springs in the Voltri Massif, Italy. *Lithos, **177***, 226-244.

Smith, P. H., et al. (2009) H_2O at the Phoenix landing site, *Science, **325***(5936), 58–61.

Spandler, C., Pettke, T., & Hermann, J. (2014) Experimental study of trace element release during ultrahigh-pressure serpentinite dehydration. *Earth and Planetary Science Letters, **391***, 296-306.

Seyfried, W. E., & Dibble, W. E. (1980) Seawater-peridotite interaction at 300ºC and 500 bars: implications for the origin of oceanic serpentinites. *Geochimica et Cosmochimica Acta, **44** (*2), 309-321.

Seyfried, W. E., Foustoukos, D. I., & Fu, Q. (2007) Redox evolution and mass transfer during serpentinization: An experimental and theoretical study at 200° C, 500bar with implications for ultramafic-hosted hydrothermal systems at Mid-Ocean Ridges. *Geochimica et Cosmochimica Acta, **71*** (15), 3872-3886.

Seyler, M., Cannat, M., Mevel, C. (2003) Evidence for major-element heterogeneity in the mantle source of abyssal peridotites from the Southwest Indian Ridge (52° to 68° E). *Geochimica et Cosmochimica Acta. **4*** (2).

Sharp, Z.D., Barnes, J.D., (2004) Water soluble chlorides in massive seafloor serpentinites: a source of chloride in subduction zones. *Earth and Planetary Science Letters **226***, 243–254.

Sleep, N. H., Meibom, A., Fridriksson, T., Coleman, R. G., & Bird, D. K. (2004) H_2-rich fluids from serpentinization: geochemical and biotic implications. *Proceedings of the National Academy of Sciences of the United States of America*, ***101*** (35), 12818-12823.

Steele-MacInnis, M., Han, L., Lowell, R. P., Rimstidt, J. D., & Bodnar, R. J. (2012a) The role of fluid phase immiscibility in quartz dissolution and precipitation in sub-seafloor hydrothermal systems. *Earth and Planetary Science Letters, **321***, 139-151.

Steele-MacInnis, M., Han, L., Lowell, R. P., Rimstidt, J. D., & Bodnar, R. J. (2012b) Quartz precipitation and fluid inclusion characteristics in sub-seafloor hydrothermal systems associated with volcanogenic massive sulfide deposits. *Central European Journal of Geosciences, **4*** (2), 275-286.

Sterner S.M. & Bodnar R.J. (1984) Synthetic fluid inclusions in natural quartz. I. Compositional types synthesized and applications to experimental geochemistry. *Geochimica et Cosmochimica Acta, **48***, 2659-2668.

Toft, P. B., Arkani-Hamed, J., & Haggerty, S. E. (1990) The effects of serpentinization on density and magnetic susceptibility: a petrophysical model. *Physics of the Earth and Planetary Interiors*, ***65*** (1), 137-157.

Tutolo B.M., Mildner D.F.R., Gagnon C.V.L., Saar M.O., Seyfried W.E. (2016) Nanoscale constraints on porosity generation and fluid flow during serpentinization: *Geology, **44***, 103–106

Ulmer, P., & Trommsdorff, V. (1995) Serpentine stability to mantle depths and subduction-related magmatism. *Science, **268*** (5212), 858-861.

Vanko, D. A., Bodnar, R. J., & Sterner, S. M. (1988) Synthetic fluid inclusions: VIII. Vapor-saturated halite solubility in part of the system NaCl-$CaCl_2$-H_2O, with application to fluid inclusions from oceanic hydrothermal systems. *Geochimica et Cosmochimica Acta, **52*** (10), 2451- 2456.

Vityk M.O., Bodnar R.J. & Doukhan, J.C. (2000) Synthetic fluid inclusions: XV. TEM investigation of plastic flow associated with re-equilibration of synthetic fluid inclusions in natural quartz. *Contributions to Mineralogy and Petrology, **139*** (3), 285 - 297.

Von Damm, K. L. (2004) Evolution of the hydrothermal system at East Pacific Rise 9 50 N: geochemical evidence for changes in the upper oceanic crust. *Mid-Ocean Ridges*, 285-304.

Wang, D., Mookherjee, M., Xu, Y., & Karato, S. I. (2006) The effect of water on the electrical conductivity of olivine. *Nature*, ***443*** (7114), 977-980.

Welhan, J. T., & Craig, H. (1979) Methane and hydrogen in East Pacific Rise hydrothermal fluids. *Geophysical Research Letters**, 6*** (11), 829-831.

Wegner, W. W., & Ernst, W. G. (1983) Experimentally determined hydration and dehydration reaction rates in the system MgO-SiO_2-H_2O. *American Journal of Sciences, **283***, 151-180.

Wenner, D.B., Taylor, H.P. (1971) Temperatures of serpentinization of ultramafic rocks based on $^{18}O/^{16}O$ fractionation between coexisting serpentine and magnetite. *Contributions to Mineralogy and Petrology*. ***32***, 165 - 185.

Wicks, F.J., O'Hanley, D.S. (1988) Serpentine minerals - structures and petrology, in: Bailey, S.W. (Ed.), Hydrous phyllosilicates. *Mineralogical Society of America*, 91-167.

Wicks, F.J., Whittaker, E.J.W. (1977) Serpentine textures and serpentinization. *The Canadian Mineralogist **15***, 459-488.

Wilcock, W. S., DeLong, E. F., Kelley, D. S., Baross, J. A., & Craig Cary, S. (2004). The subseafloor biosphere at mid-ocean ridges. Washington DC *American Geophysical Union Geophysical Monograph Series*, ***144***.

Whittaker, E. J. W., & Zussman, J. (1956) The characterization of serpentine minerals by X-ray diffraction. *Mineralogy Magazine, **31*** (233), 1025-1047.

Wolery, T. J. (1992) EQ3/6: A software package for geochemical modeling of aqueous systems: package overview and installation guide (version 7.0). Livermore, CA: Lawrence Livermore National Laboratory.

Yardley, B. W., & Bodnar, R. J. (2014) Fluids in the continental crust. *Geochemical Perspectives*, ***3*** (1), 1-2.

Zolensky, M. E., Bodnar, R. J., Gibson, E. K., Nyquist, L. E., Reese, Y., Shih, C. Y., & Wiesmann, H. (1999) Asteroidal water within fluid inclusion-bearing halite in an H5 chondrite, Monahans (1998) *Science*, ***285*** (5432), 1377-1379.

Zu, C., Dolocan, A., Xiao, P., Stauffer, S., Henkelman, G., & Manthiram, A. (2015) Breaking Down the Crystallinity: The Path for Advanced Lithium Batteries. *Advanced Energy Materials*.

Tables

Table 1. EMPA data used to determine the stoichiometry and Mg # of the olivine host for the chemical analyses.

	Content (%)
SiO_2	40.67
MgO	50.03
CaO	0.05
MnO	0.126
FeO	8.66
NiO	0.37
Total	99.92
Mg #	85*

*$Mg\# = \left(\frac{MgO}{MgO+FeO}\right) \times 100$

Table 2. Experimental conditions and results.

Run	Fluid Composition	S	Experiment type	T (ºC)	t (days)	Mineral assemblege
1	H_2O-NaCl-$MgCl_2$	1	Furnace	280(±5)	120	L/C+B
2	H_2O-NaCl-$MgCl_2$	1	Chaixmeca	280(±8)	120	L/C+B+M
3	H_2O-NaCl-$MgCl_2$	3.5	Furnace	280(±5)	30	L/C+B
4	H_2O-NaCl-$MgCl_2$	3.5	Furnace	280(±5)	60	L/C+B
5	H_2O-NaCl-$MgCl_2$	3.5	Furnace	280(±5)	90	L/C+B
6	H_2O-NaCl-$MgCl_2$	3.5	Chaixmeca	280(±8)	120	L/C+B+M
7	H_2O-NaCl-$MgCl_2$	6	Furnace	280(±5)	120	L/C+B
8	H_2O-NaCl-$MgCl_2$	10	Furnace	280(±5)	270	L/C+B+M
9	H_2O-NaCl	3.5	Furnace	280(±5)	45	L/C+B
10	H_2O-NaCl	10	Furnace	280(±5)	270	L/C+B+M
11	H_2O-$MgCl_2$	3.5	Furnace	280(±5)	270	L/C+B+M
12	H_2O-$MgCl_2$	10	Furnace	280(±5)	270	L/C+B+M

S = salinity in wt.%,
Furnace = experiments doing thermal cycling from RT » 280 » RT » 280,
Chaixmeca = experiments at constant 280ºC,
Mineral assemblages, L/C = lizardite or chrysotile, B = brucite, M = magnetite

Table 3. Raman peak positions of the reaction products and the olivine host. Main peaks that were identified in this study are in bold.

Mineral	Peak positions (cm^{-1})
Serpentine*	224 - 232
	385 - 394
	685 - 695
	1090 - 1100
	3690-3703
	3620-3750
Brucite	272-270
	438-441
	3624-3665
Magnetite	305
	530
	660
Olivine	232
	584
	605
	823
	855
	880
	920
	960

*The dispersion in Raman peak positions has led to difficult identification of the reaction products as lizardite and/or chrysotile.

Table 4. TOF SIMS data and composition of the minerals from Figure 5. The areas refer to the areas highlighted in fluid inclusion shown in Figure 5.

Elements[a]	Area I		Area II		Area III		Area IV		Area V		Area VI		Area VII	
	Olivine	Brucite	Olivine	Serpentine	Olivine	Serpentine	Olivine	Serpentine	Olivine	Serpentine	Olivine	Brucite	Olivine	Serpentine
Na+	615	53677	1554	37148	1155	38146	1209	36086	985	82079	453	3165	2330	18358
^{25}Mg+	146296	103126	305704	80630	369753	14684	162388	112338	111957	116932	141797	9493	542468	74543
Si+	52707	65267	152903	56945	231141	8658	60456	57906	29471	34329	81683	6756	280256	54682
Fe+	47829	30132	107244	20184	144535	3831	52901	30230	43481	29408	52226	3039	192260	20500
Mg/Mg+Fe	0.75	0.77	0.74	0.80	0.72	0.79	0.75	0.79	0.72	0.80	0.73	0.76	0.74	0.78
Mg #	85[b]	87	85[b]	92	85[b]	94	85[b]	90	85[b]	94	85[b]	88	85[b]	90

[a]TOF SIMS data units are counts per ROI (region of interest), [b]Mg # of the olivine was calculated from the EMPA data of Table 1.

Table 5. Rates of reaction, rates of reaction, fluxes, activities and residual data for every individual SFI from the experimental with composition H_2O-NaCl-$MgCl_2$ (Na/Mg 8:1).

Salinity (wt.%)	SFI	r (mol/sec)	J (mol/m^{2}sec)	log r	log J	a_{H_2O}	log a_{H_2O}	log J Residuals*
1	FIA 1A	9.56E-18	7.58E-09	-17.02	-8.12	0.995	-0.0021	-0.103
1	FIA 1B	8.10E-18	6.43E-09	-17.09	-8.19	0.995	-0.0021	-0.175
1	FIA 1C	7.49E-18	5.95E-09	-17.13	-8.23	0.995	-0.0021	-0.209
1	FIA 1D	8.90E-18	7.06E-09	-17.05	-8.15	0.995	-0.0021	-0.134
1	FIA 1E	8.90E-18	7.06E-09	-17.05	-8.15	0.995	-0.0021	-0.134
1	FIA 1F	9.56E-18	7.58E-09	-17.02	-8.12	0.995	-0.0021	-0.103
1	FIA 1G	6.03E-18	4.79E-09	-17.22	-8.32	0.995	-0.0021	-0.303
1	FIA 1H	8.90E-18	7.06E-09	-17.05	-8.15	0.995	-0.0021	-0.134
1	FIA 1I	8.90E-18	7.06E-09	-17.05	-8.15	0.995	-0.0021	-0.134
3.5	FIA 1A	4.23E-18	3.36E-09	-17.37	-8.47	0.984	-0.0069	0.120
3.5	FIA 1B	3.70E-18	2.94E-09	-17.43	-8.53	0.984	-0.0069	0.062
3.5	FIA 1D	1.76E-18	1.40E-09	-17.75	-8.86	0.984	-0.0069	-0.261
3.5	FIA 1H	2.23E-18	1.77E-09	-17.65	-8.75	0.984	-0.0069	-0.159
3.5	FIA 1I	2.46E-18	1.95E-09	-17.61	-8.71	0.984	-0.0069	-0.115
3.5	FIA 2C	4.00E-18	3.17E-09	-17.40	-8.50	0.984	-0.0069	0.096
3.5	FIA 2D	6.03E-18	4.79E-09	-17.22	-8.32	0.984	-0.0069	0.274
3.5	FIA 2E	5.45E-18	4.33E-09	-17.26	-8.36	0.984	-0.0069	0.230
3.5	FIA 3A	3.31E-18	2.63E-09	-17.48	-8.58	0.984	-0.0069	0.013
3.5	FIA 3B	3.81E-18	3.03E-09	-17.42	-8.52	0.984	-0.0069	0.075
3.5	FIA 3C	3.03E-18	2.41E-09	-17.52	-8.62	0.984	-0.0069	-0.024
3.5	FIA 3D	3.84E-18	3.04E-09	-17.42	-8.52	0.984	-0.0069	0.078
3.5	FIA 3E	4.14E-18	3.28E-09	-17.38	-8.48	0.984	-0.0069	0.110
3.5	FIA 3G	3.22E-18	2.56E-09	-17.49	-8.59	0.984	-0.0069	0.002
3.5	FIA 3H	3.14E-18	2.49E-09	-17.50	-8.60	0.984	-0.0069	-0.009
3.5	FIA 3I	3.44E-18	2.73E-09	-17.46	-8.56	0.984	-0.0069	0.030
3.5	FIA 3J	3.79E-18	3.00E-09	-17.42	-8.52	0.984	-0.0069	0.072
3.5	FIA 3K	3.72E-18	2.95E-09	-17.43	-8.53	0.984	-0.0069	0.065
3.5	FIA 3L	5.03E-18	3.99E-09	-17.30	-8.40	0.984	-0.0069	0.195
3.5	FIA 3M	5.04E-18	4.00E-09	-17.30	-8.40	0.984	-0.0069	0.196
3.5	FIA 3N	4.84E-18	3.84E-09	-17.31	-8.42	0.984	-0.0069	0.179
3.5	FIA 3O	2.27E-18	1.80E-09	-17.64	-8.74	0.984	-0.0069	-0.150
3.5	FIA 3P	2.66E-18	2.11E-09	-17.57	-8.68	0.984	-0.0069	-0.081
3.5	FIA 3Q	2.18E-18	1.73E-09	-17.66	-8.76	0.984	-0.0069	-0.168
3.5	FIA 3R	3.90E-18	3.10E-09	-17.41	-8.51	0.984	-0.0069	0.085
3.5	FIA 3S	4.45E-18	3.53E-09	-17.35	-8.45	0.984	-0.0069	0.142
3.5	FIA 3T	3.42E-18	2.71E-09	-17.47	-8.57	0.984	-0.0069	0.028
3.5	FIA 3U	3.71E-18	2.94E-09	-17.43	-8.53	0.984	-0.0069	0.063
3.5	FIA 3Y	4.97E-18	3.95E-09	-17.30	-8.40	0.984	-0.0069	0.190
3.5	FIA 3Z	3.03E-18	2.41E-09	-17.52	-8.62	0.984	-0.0069	-0.024

Table 5. Continuation

Salinity (wt.%)	SFI	r (mol/sec)	J (mol/m^{2}sec)	log r	log J	a_{H_2O}	log a_{H_2O}	log J Residuals*
3.5	FIA 3AB	4.33E-18	3.44E-09	-17.36	-8.46	0.984	-0.0069	0.130
3.5	FIA 3AC	4.86E-18	3.86E-09	-17.31	-8.41	0.984	-0.0069	0.180
3.5	FIA 3AE	2.66E-18	2.11E-09	-17.57	-8.67	0.984	-0.0069	-0.081
3.5	FIA 4A	4.56E-18	3.62E-09	-17.34	-8.44	0.984	-0.0069	0.153
3.5	FIA 4D	3.84E-18	3.05E-09	-17.42	-8.52	0.984	-0.0069	0.079
3.5	FIA 4E	3.70E-18	2.94E-09	-17.43	-8.53	0.984	-0.0069	0.062
3.5	FIA 4F	2.56E-18	2.03E-09	-17.59	-8.69	0.984	-0.0069	-0.097
3.5	FIA 4G	1.92E-18	1.52E-09	-17.72	-8.82	0.984	-0.0069	-0.223
6	FIA 1A	1.04E-18	8.28E-10	-17.98	-9.08	0.974	-0.0116	0.077
6	FIA 1B	1.18E-18	9.35E-10	-17.93	-9.03	0.974	-0.0116	0.130
6	FIA 1E	9.81E-19	7.78E-10	-18.01	-9.11	0.974	-0.0116	0.051
6	FIA 1F	1.08E-18	8.59E-10	-17.97	-9.07	0.974	-0.0116	0.093
6	FIA 1G	9.36E-19	7.43E-10	-18.03	-9.13	0.974	-0.0116	0.030
6	FIA 1H	9.35E-19	7.42E-10	-18.03	-9.13	0.974	-0.0116	0.030
6	FIA 1I	1.10E-18	8.74E-10	-17.96	-9.06	0.974	-0.0116	0.101
6	FIA 2A	1.23E-18	9.76E-10	-17.91	-9.01	0.974	-0.0116	0.149
6	FIA2C	9.82E-19	7.79E-10	-18.01	-9.11	0.974	-0.0116	0.051
6	FIA 2H	1.11E-18	8.79E-10	-17.96	-9.06	0.974	-0.0116	0.103
10	FI A	6.80E-20	5.40E-11	-19.17	-10.27	0.958	-0.0187	-0.254
10	FI B	6.80E-20	5.40E-11	-19.17	-10.27	0.958	-0.0187	-0.254
10	FI C	1.33E-19	1.05E-10	-18.88	-9.98	0.958	-0.0187	0.035
10	FI D	8.38E-20	6.65E-11	-19.08	-10.18	0.958	-0.0187	-0.163
10	FI K	1.18E-19	9.33E-11	-18.93	-10.03	0.958	-0.0187	-0.017
10	FI L	6.80E-20	5.40E-11	-19.17	-10.27	0.958	-0.0187	-0.254

*These data represent the difference from the measured log J to the predicted by Eq. (10).

Table 6. Rates of reaction, rates of reaction, fluxes, activities and residual data for every individual SFI from the experimental with composition H_2O-NaCl.

Salinity (wt.%)	SFI	r (mol/sec)	J (mol/m^{2}sec)	log r	log J	a_{H_2O}	log a_{H_2O}	log J Residuals*
3.5	FIA 1C	4.65E-18	3.69E-09	-17.33	-8.43	0.98	-0.0071	0.112
3.5	FIA 1D	3.20E-18	2.54E-09	-17.49	-8.59	0.98	-0.0071	-0.050
3.5	FIA 2B	4.89E-18	3.88E-09	-17.31	-8.41	0.98	-0.0071	0.134
3.5	FIA 2E	4.89E-18	3.88E-09	-17.31	-8.41	0.98	-0.0071	0.134
3.5	FIA 2F	3.22E-18	2.56E-09	-17.49	-8.59	0.98	-0.0071	-0.048
3.5	FIA 2K	1.75E-18	1.39E-09	-17.76	-8.86	0.98	-0.0071	-0.312
3.5	FIA 2L	4.89E-18	3.88E-09	-17.31	-8.41	0.98	-0.0071	0.134
3.5	FIA 2P	2.68E-18	2.13E-09	-17.57	-8.67	0.98	-0.0071	-0.127
3.5	FIA 2R	3.80E-18	3.02E-09	-17.42	-8.52	0.98	-0.0071	0.024
10	FI B	8.63E-20	6.85E-11	-19.06	-10.16	0.96	-0.019	-0.108
10	FI C	2.08E-19	1.65E-10	-18.68	-9.78	0.96	-0.019	0.275
10	FI D	1.88E-19	1.50E-10	-18.72	-9.83	0.96	-0.019	0.231
10	FI H	7.01E-20	5.56E-11	-19.15	-10.25	0.96	-0.019	-0.198
10	FI I	5.33E-20	4.23E-11	-19.27	-10.37	0.96	-0.019	-0.317
10	FI K	9.92E-20	7.87E-11	-19.00	-10.10	0.96	-0.019	-0.047
10	FI L	1.75E-19	1.39E-10	-18.76	-9.86	0.96	-0.019	0.199
10	FI M	1.02E-19	8.10E-11	-18.99	-10.09	0.96	-0.019	-0.035

*These data represent the difference from the measured log J to the predicted by Eq. (11).

Table 7. Chemical compositions of the reaction products calculated from the thermodynamic simulations using EQ3/6. All the compositions are given in Mg to Fe ratios # (MgO/MgO+FeO).

Extent of reaction	Serpentine	Brucite
0	–	99.9
0.05	97.8	94.9
0.1	97.5	93.6
0.15	97.2	92.8
0.20	97.0	92.1
0.25	96.8	91.5
0.30	96.6	91.0
0.35	96.5	90.5
0.40	96.3	90.1
0.45	96.2	89.8
0.50	96.1	89.4
0.55	95.9	89.1
0.60	95.8	88.8
0.65	95.7	88.5
0.70	95.6	88.2
0.75	95.5	88.0
0.80	95.4	87.7
0.85	95.3	87.5
0.90	95.2	87.2
0.95	95.1	87.0
1	95.0	86.8

Figures

Figure 1

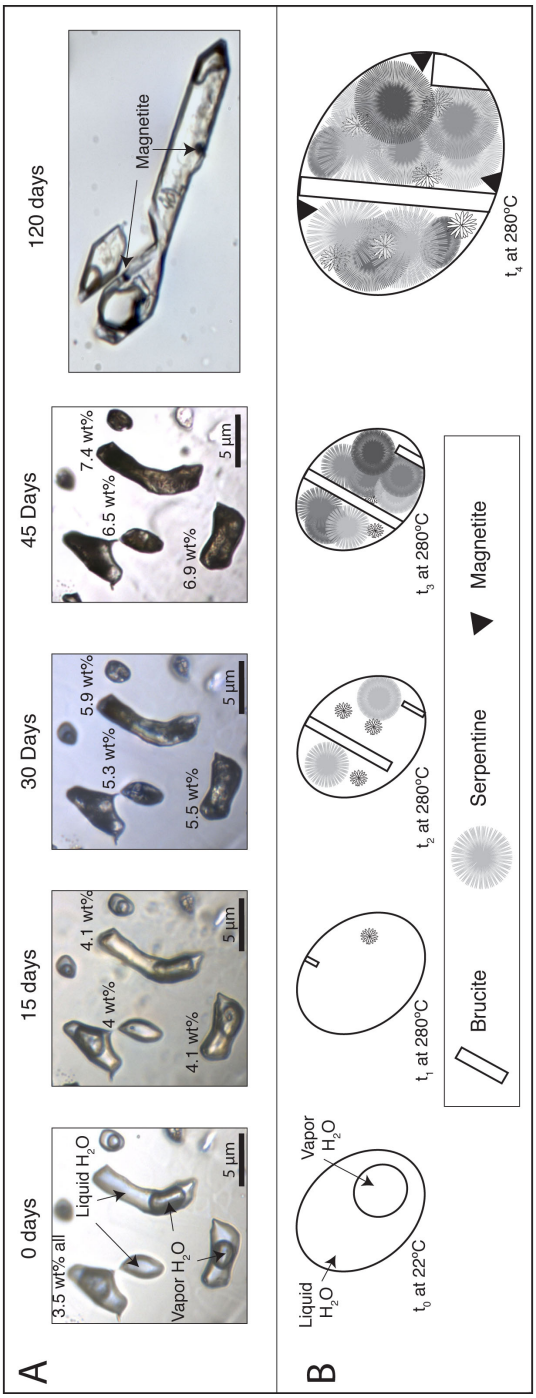

Figure 1. Photomicrographs (top) and schematic illustrations (bottom) showing changes in the phase relations in synthetic fluid inclusions (SFI) as a function of the amount of time held at the serpentinization temperature of 280°C. All photomicrographs and illustrations represent the phase behavior at room temperature. . A) Photomicrographs of several SFI from Run 4 (3.5 wt.% and H_2O-NaCl-$MgCl_2$) taken after 0, 15, 30, 45 and 270 days at the serpentinization temperature of 280ºC. Magnetite appears after 120 experimental in Run 1. (1 wt.% and H_2O-NaCl-$MgCl_2$) B) Schematic diagram of the reaction progress inside the micro-reactors. At t_0, the inclusion is at room temperature after synthetizing the fluid inclusions have a fluid composed with a aqueous phase and a vapor phase. At t_1, after a few days at 280ºC reaction begins and small crystals of brucite and serpentine appear. At t_2, reaction continues and more crystals are formed. At t_3, the fluid inclusion is almost full with crystals. At t_4, after several months at 280ºC magnetite crystals appear inside the micro-reactors.

Figure 2

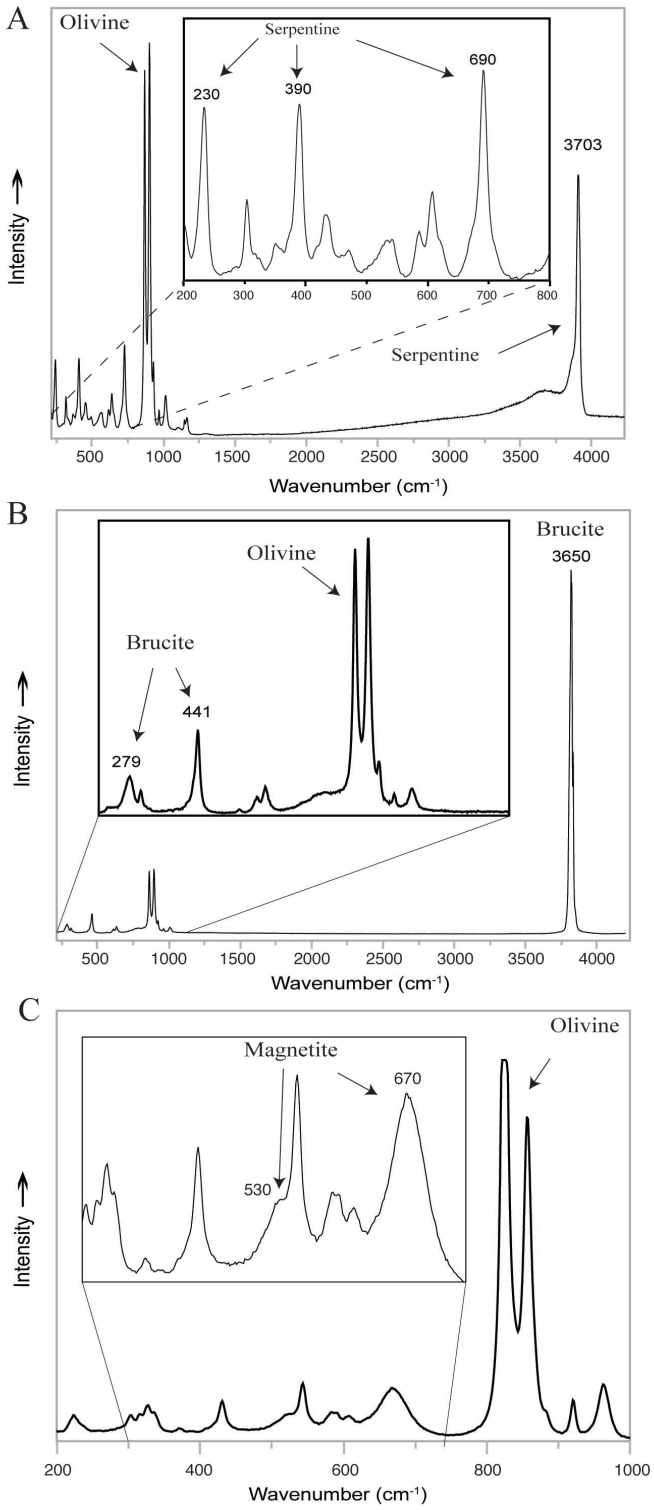

Figure 2. Representative Raman spectra of the olivine host and serpentine (A), brucite and olivine host (B), and magnetite and the olivine host (C).

Figure 3

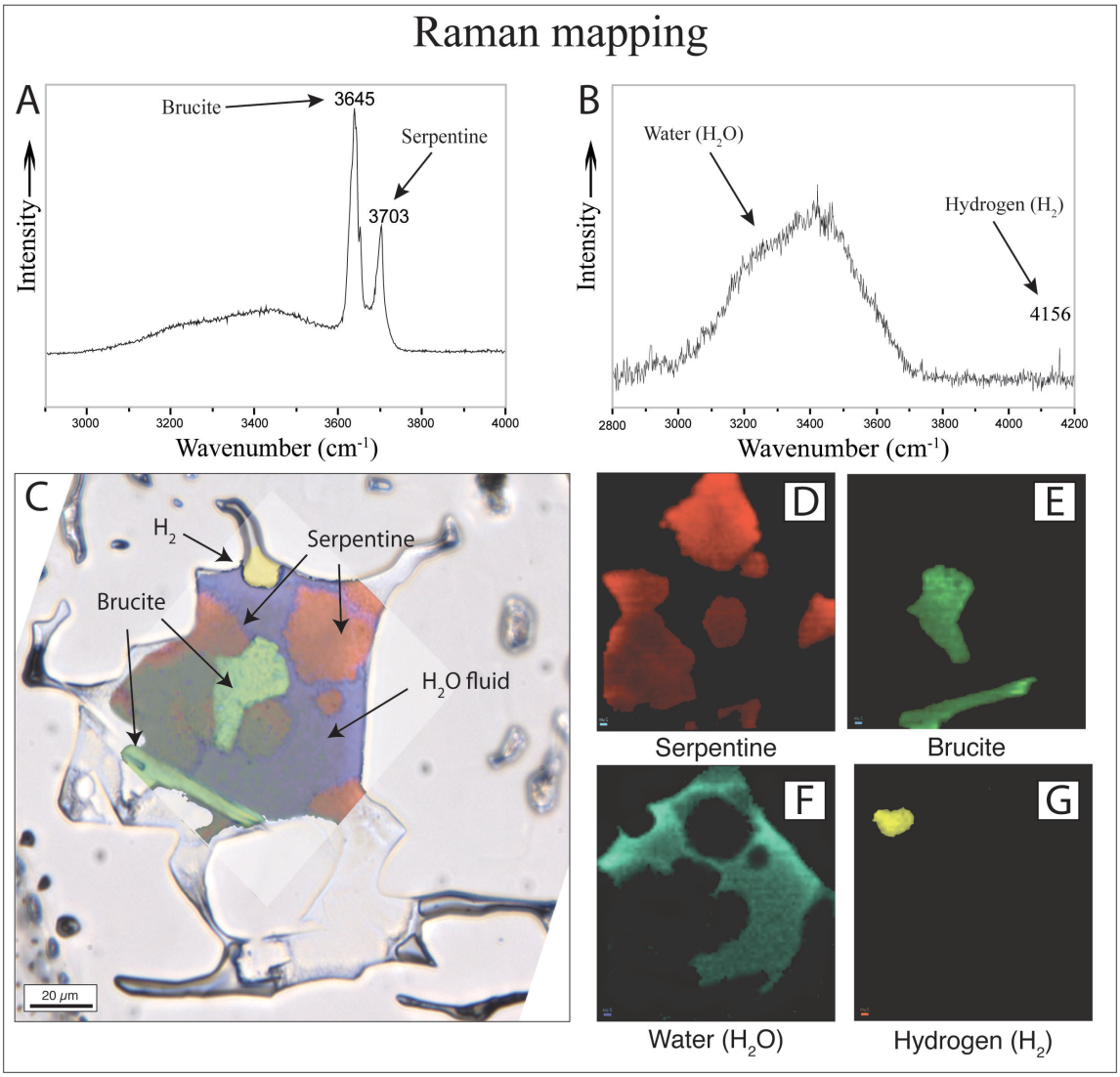

Figure 3. Raman map of a large, irregularly-shaped SFI from Run 3 (3.5 wt.% and H_2O-NaCl-$MgCl_2$). A) The minerals detected are brucite and serpentine (chrysotile or lizardite). B) The map also shows the H_2O in the aqueous phase and H_2 in the vapor bubble. C) Raman map of all the volatile and mineral species inside the SFI: D) serpentine in red, E) brucite in green, F) water in blue, G) H_2 in yellow.

Figure 4

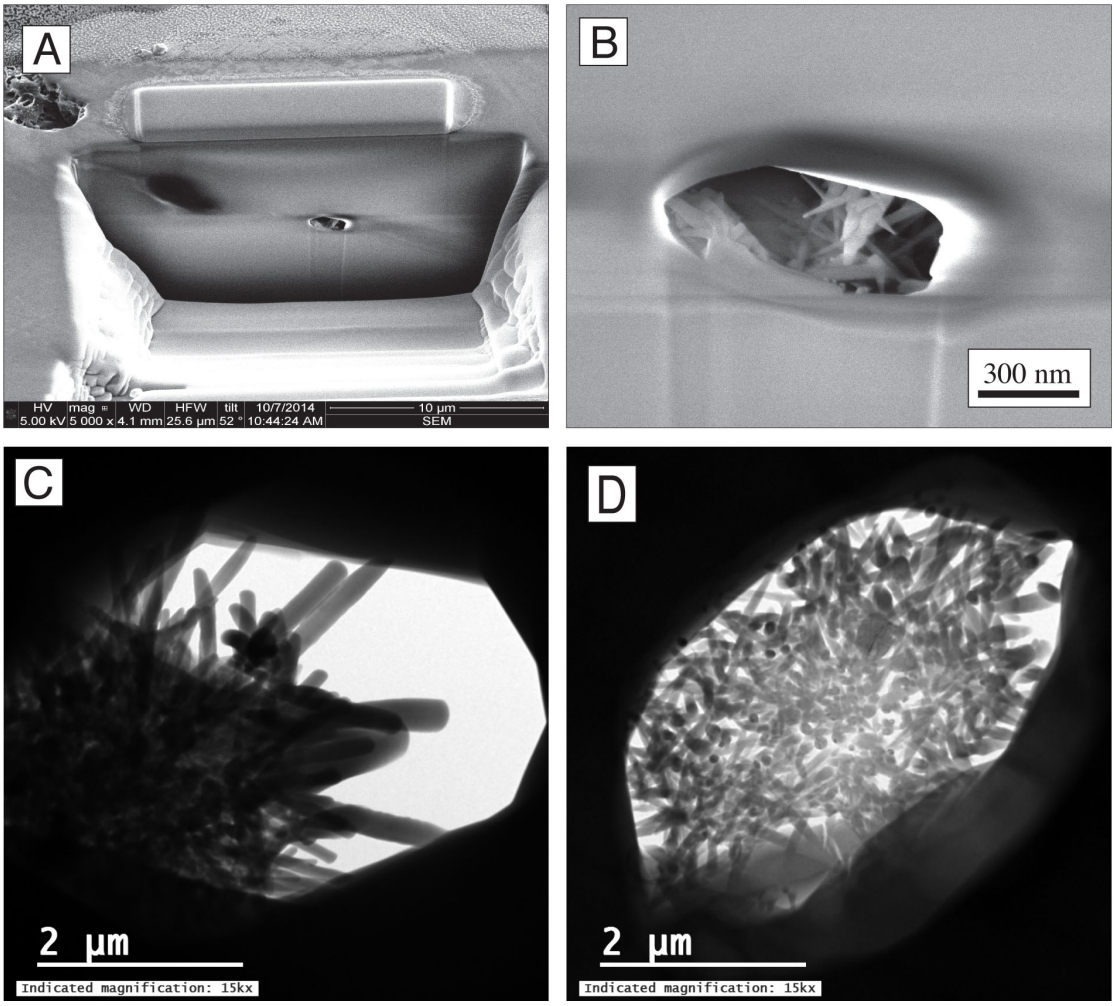

Figure 4. FIB-SEM and TEM images of SFI. (A) A SFI filled with reaction products is exposed in the wall of a pit excavated by FIB. (B) Enlargement of the area in (A) containing the SFI, showing typical fibrous and conical chrysotile crystals. (C-D) TEM images of a SFI. The fibrous and conical chrysotile crystals are easily identified.

Figure 5

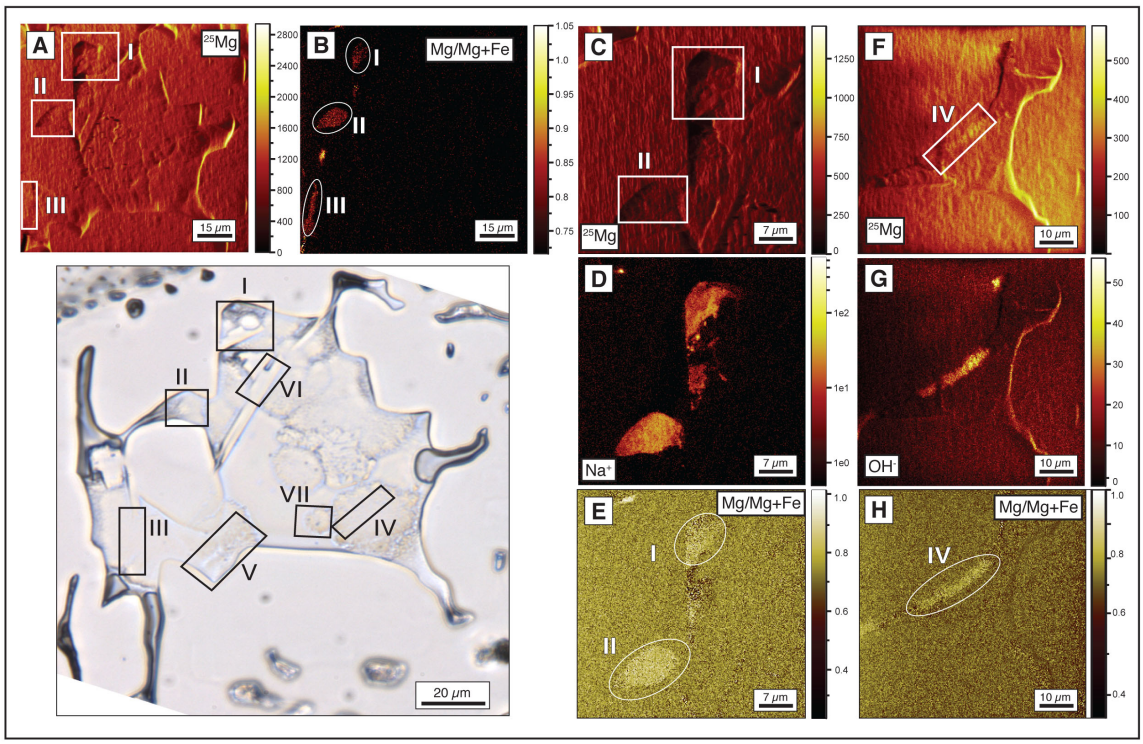

Figure 5. TOF SIMS elemental maps a SFI from Run 3 (3.5 wt.% and H_2O-NaCl-$MgCl_2$). A-H) Elemental maps of different parts of a SFI. I to VII show areas of interest where the TOF SIMS analyses were performed and are also shown on Table 4 Mg# obtained from TOF-SIMS analyses are listed in Table 4. (A, E, F) ^{25}Mg maps. (B, E, H) $^{25}Mg/(^{25}Mg+Fe)$ maps showing compositional differences between the Mg# of the host and that of the reaction products. (D) Na map. The Na is contained in the frozen aqueous phase in the SFI. (G) OH maps showing the presence of serpentine and H_2O ice.

Figure 6

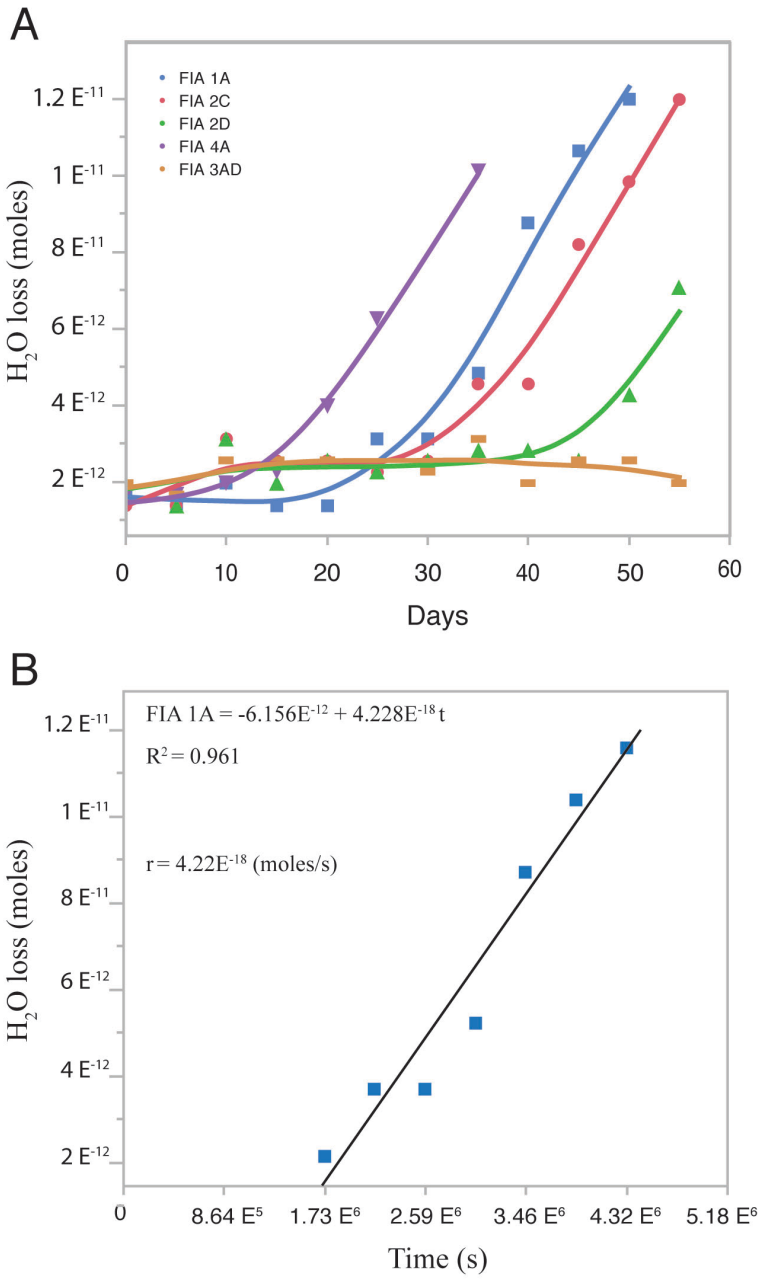

Figure 6. Moles of H_2O consumed as a function of the amount of time sample was held at 280°C. (A) Example of the moles of H_2O consumed as a function of time for five SFI micro reactors from Run 4 (3.5 wt.% and H_2O-NaCl-$MgCl_2$). Solid lines are drawn as references to identify data from individual SFI. (B) Fitted line moles of H_2O loss vs. time data for SFI FIA1A from run 4. The initial rate method was applied for each SFI starting from the time at which the reaction started. The slope of the fitted line represents the rate of reaction (r).

Figure 7

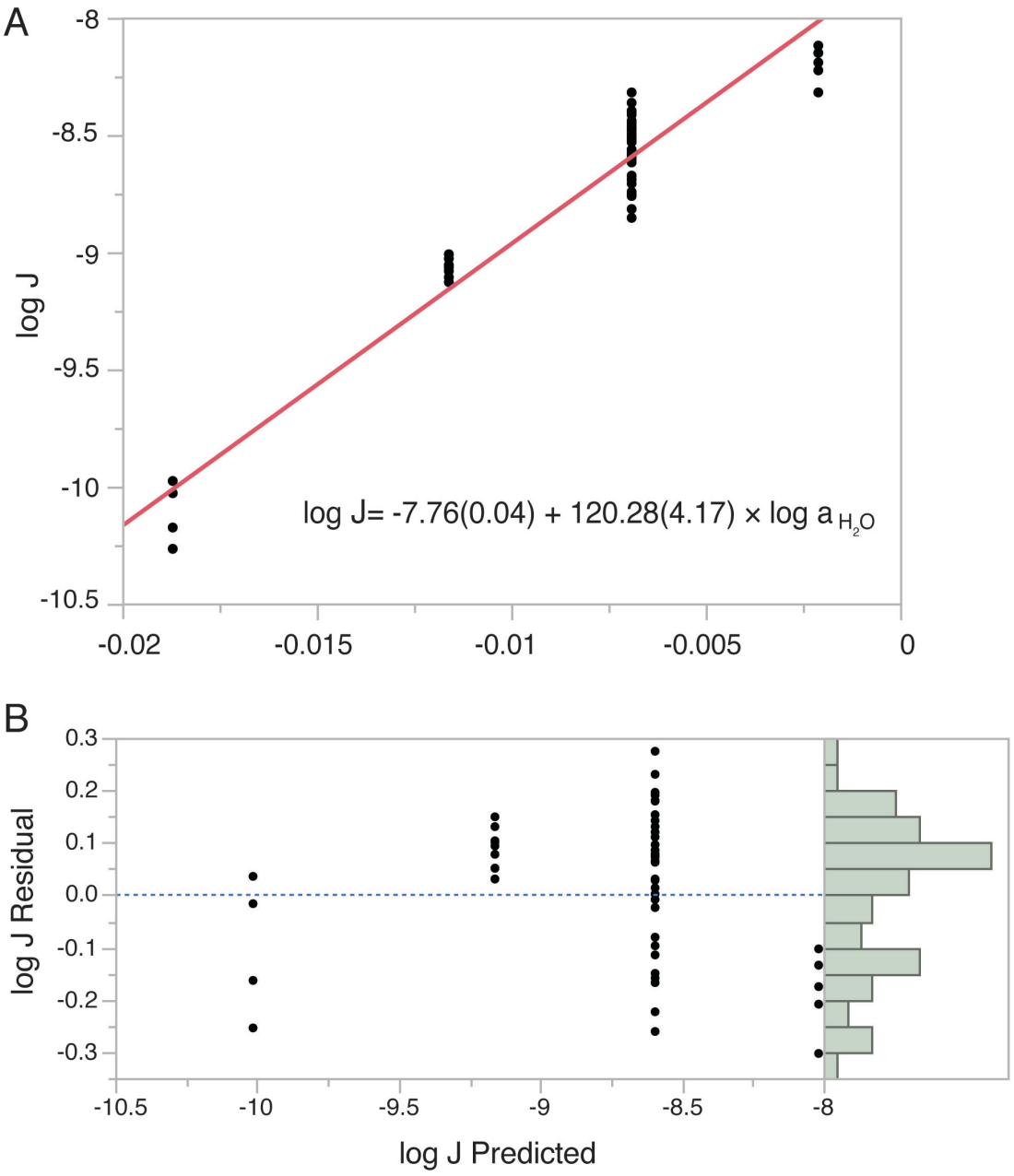

Figure 7. Rate equation calculated from the rates of reaction of olivine with an initial fluid composition of H_2O-NaCl-$MgCl_2$. (A) The rate equation represents a linear regression of all the rates of reaction from all experiments using this starting fluid composition. (B) Predicted vs. Residual plot showing the dispersion of the rates predicted by Eq. (10) from the actual rates.

Figure 8

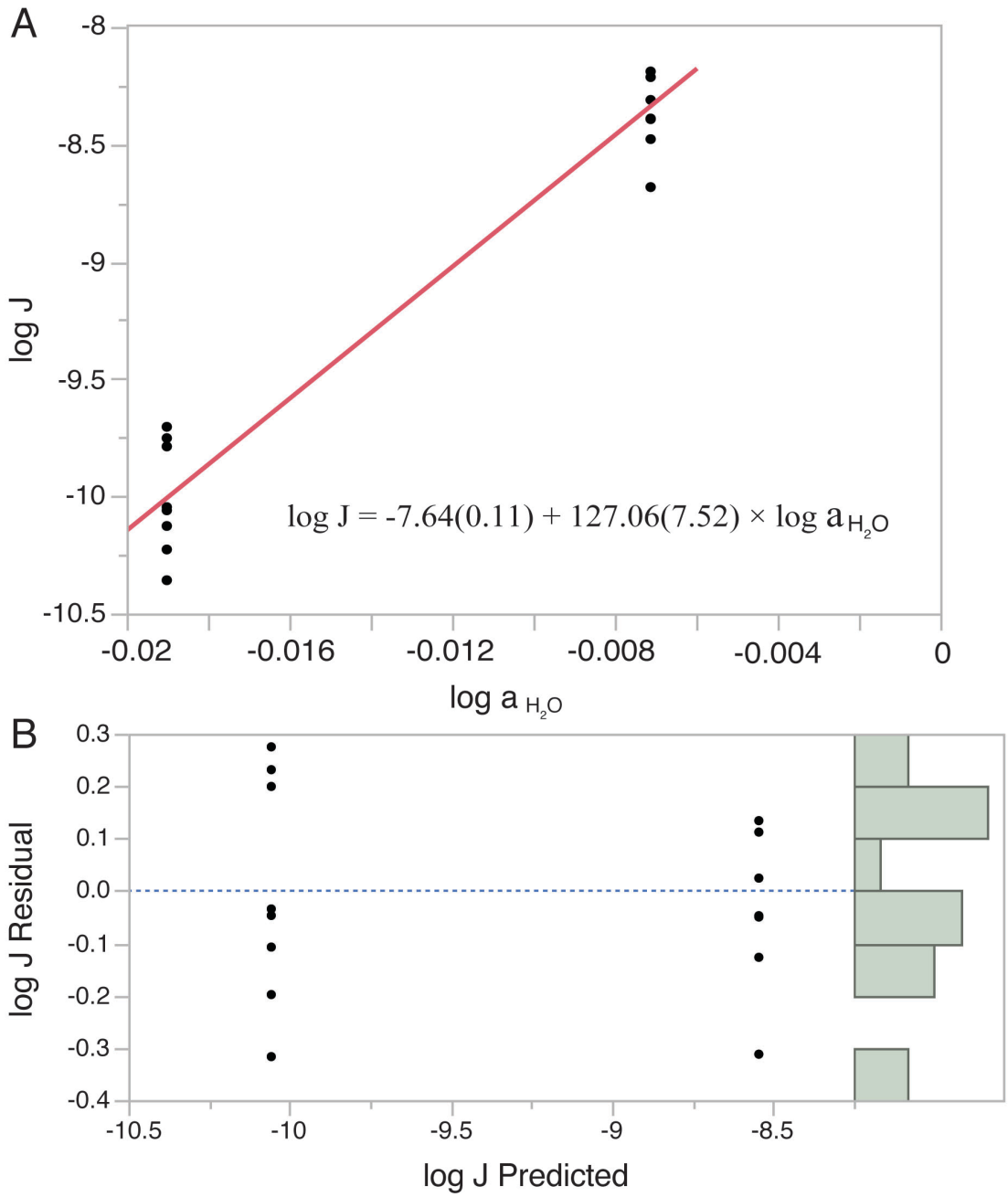

Figure 8. Rate equation calculated from the rates of reaction of olivine with an initial fluid composition of H_2O-NaCl. (A) The rate equation represents a linear regression of all the rates of reaction from all experiments using this starting fluid composition. (B) Predicted vs. Residual plot showing the dispersion of the rates predicted by Eq. (11) from the actual rates.

Figure 9

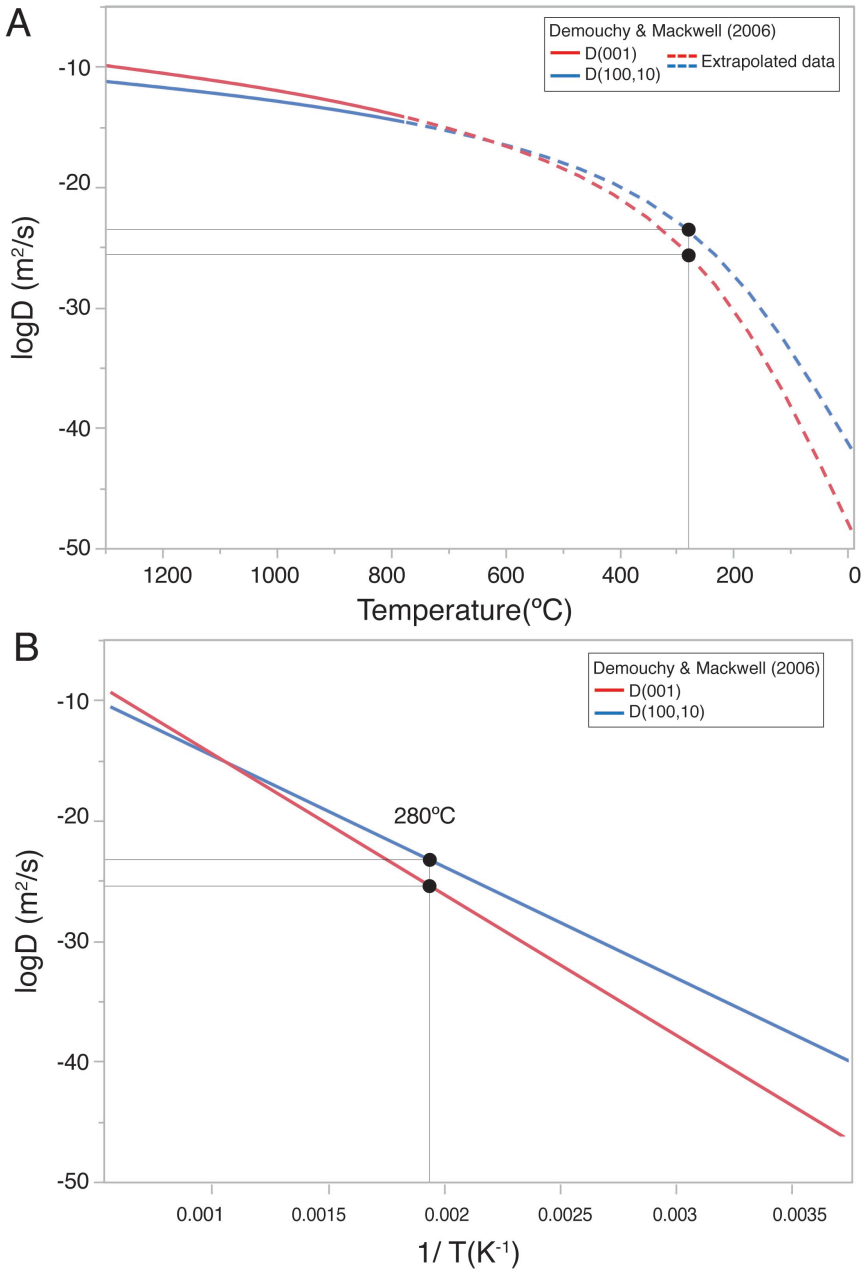

Figure 9. Model for the diffusivity of hydrogen through olivine from Demouchy & Mackwell (2006) as a function of temperature. A) The diffusivity models parallel to the crystal plane (001) in red and for plane (100,10) in blue as a function of temperature. The equation (solid line) was extrapolated (dashed line) to lower temperatures to estimate the rate at which hydrogen will defuse out of the SFI at 280°C. For the T of our experiments the diffusivity of H_2 in olivine is between 12 to 14 orders of magnitude

slower. B) Diffusivity models for (001) and (100,10) crystal plane as a function of the inverse of temperature (K-1).

Figure 10

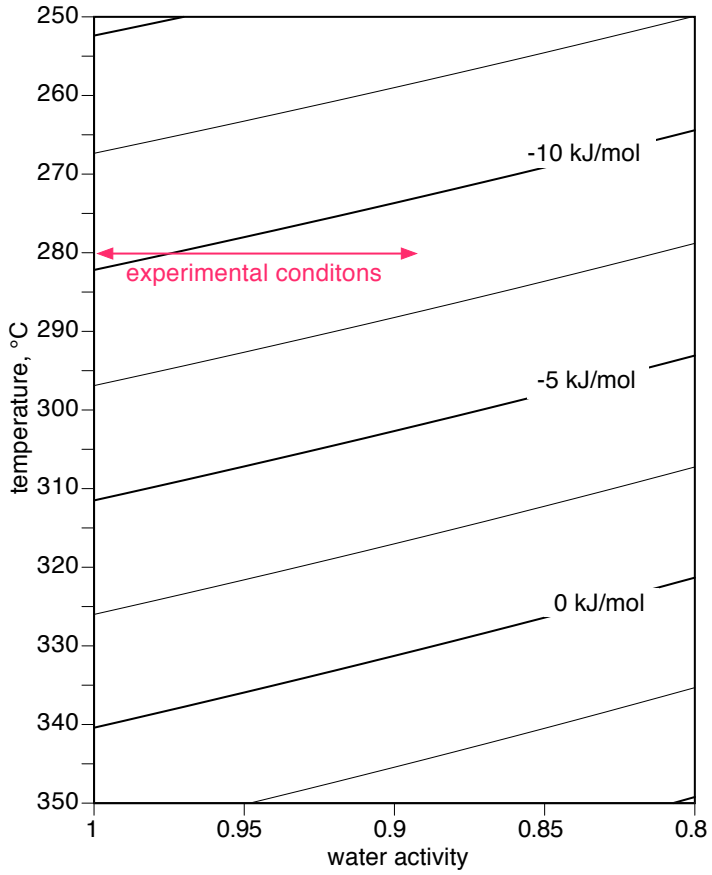

Figure 10. Chemical potential (based on $\Delta G_r°$ values from SUPCRT, Johnson et al., 1992) for the forsterite hydration reaction as a function of temperature and water activity (see text for further explanation).

Figure 11

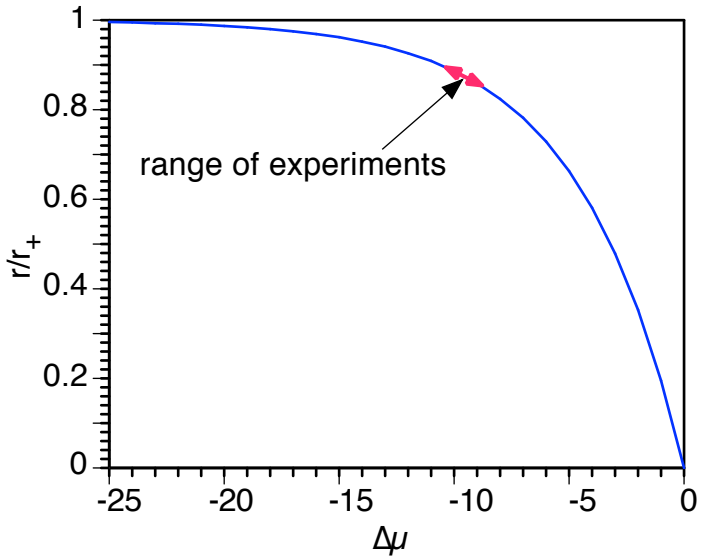

Figure 11. Relative reaction rate for reaction Eq. (1) at 280°C. The curve represents the reaction path, from a flat area far from equilibrium to a step close to equilibrium area. The experiments here described (red arrow) were conducted for conditions where the relatively flat far from equilibrium curve transitions into the relatively steep near equilibrium part of the curve.